



ARL-TR-7746 • Aug 2016



Understanding Effects of Traumatic Insults on Brain Structure and Function

by Thuvan Piehler, Nicole Zander, Lars Piehler, Richard Benjamin, Ray Sparks, Mary Boggs, Mark DeCoster, Rohan Banton, Yelena Sliozberg, Tanya Chantawansri, David Boothe, Alfred Yu, Jean Vettel, and Piotr Franaszczuk

Approved for public release; distribution is unlimited.

NOTICES

Disclaimers

The findings in this report are not to be construed as an official Department of the Army position unless so designated by other authorized documents.

Citation of manufacturer's or trade names does not constitute an official endorsement or approval of the use thereof.

Destroy this report when it is no longer needed. Do not return it to the originator.



Understanding Effects of Traumatic Insults on Brain Structure and Function

**by Thuvan Piehler, Nicole Zander, Lars Piehler, Richard Benjamin,
Rohan Banton, Yelena Sliozberg, and Tanya Chantawansri**
Weapons and Materials Research Directorate, ARL

Ray Sparks
Bowhead Science and Technology, LLC

David Boothe
Survivability/Lethality Analysis Directorate, ARL

Alfred Yu, Jean Vettel, and Piotr Franaszczuk
Human Research and Engineering Directorate, ARL

Mary Boggs
Department of Biology, University of Delaware

Mark DeCoster
Department of Biomedical Engineering, Louisiana Tech University

REPORT DOCUMENTATION PAGE				Form Approved OMB No. 0704-0188	
<p>Public reporting burden for this collection of information is estimated to average 1 hour per response, including the time for reviewing instructions, searching existing data sources, gathering and maintaining the data needed, and completing and reviewing the collection information. Send comments regarding this burden estimate or any other aspect of this collection of information, including suggestions for reducing the burden, to Department of Defense, Washington Headquarters Services, Directorate for Information Operations and Reports (0704-0188), 1215 Jefferson Davis Highway, Suite 1204, Arlington, VA 22202-4302. Respondents should be aware that notwithstanding any other provision of law, no person shall be subject to any penalty for failing to comply with a collection of information if it does not display a currently valid OMB control number.</p> <p>PLEASE DO NOT RETURN YOUR FORM TO THE ABOVE ADDRESS.</p>					
1. REPORT DATE (DD-MM-YYYY) August 2016		2. REPORT TYPE Director's Strategic Initiative (DSI)		3. DATES COVERED (From - To) 1 March 2013–30 September 2015	
4. TITLE AND SUBTITLE Understanding Effects of Traumatic Insults on Brain Structure and Function				5a. CONTRACT NUMBER	
				5b. GRANT NUMBER	
				5c. PROGRAM ELEMENT NUMBER	
6. AUTHOR(S) Thuvan Piehler, Nicole Zander, Lars Piehler, Richard Benjamin, Ray Sparks, Mary Boggs, Mark DeCoster, Rohan Banton, Yelena Sliozberg, Tanya Chantawansri, David Boothe, Alfred Yu, Jean Vettel, and Piotr Franaszczuk				5d. PROJECT NUMBER	
				5e. TASK NUMBER	
				5f. WORK UNIT NUMBER	
7. PERFORMING ORGANIZATION NAME(S) AND ADDRESS(ES) US Army Research Laboratory ATTN: RDRL-WML-C Aberdeen Proving Ground, MD 21005-5066				8. PERFORMING ORGANIZATION REPORT NUMBER ARL-TR-7746	
9. SPONSORING/MONITORING AGENCY NAME(S) AND ADDRESS(ES)				10. SPONSOR/MONITOR'S ACRONYM(S)	
				11. SPONSOR/MONITOR'S REPORT NUMBER(S)	
12. DISTRIBUTION/AVAILABILITY STATEMENT Approved for public release; distribution is unlimited.					
13. SUPPLEMENTARY NOTES					
14. ABSTRACT A multidisciplinary research project was initiated to enhance the fundamental understanding of brain structural and functional injury mechanisms associated with mild blast events on neuronal cell cultures. Two foundational infrastructure capabilities were realized, but more critically, in-house expertise was developed to execute the research and enable the future US Army capability. The first accomplishment centers on cellular experimentation. A novel experimental research platform was developed to examine the effects of explosive pressure impacts on neurons. This indoor in-vitro experimental research program uses real explosives to study the impact of blast on dissociated neurons. The experimental results found transient damage to the neuronal cell membranes that modulate neurotransmitter release that is necessary for brain signals to generate and carry information between brain regions. The second accomplishment focuses on a multiscale computational brain model implemented in a framework known as GENESIS with parallel processing, where the research team parameterized a brain model to simulate the results from the cellular experiments. Using the model to examine the effect of cellular membrane on the coordinated functional activity of thousands of neurons, the research results revealed that neuronal injury effects on the cells disrupted the coordinated, low-frequency activity of brain signals hypothesized to underlie behavioral performance.					
15. SUBJECT TERMS trauma, brain structure and function, blast, explosive, neurons					
16. SECURITY CLASSIFICATION OF:			17. LIMITATION OF ABSTRACT	18. NUMBER OF PAGES	19a. NAME OF RESPONSIBLE PERSON
a. REPORT	b. ABSTRACT	c. THIS PAGE			Thuvan Piehler
Unclassified	Unclassified	Unclassified	UU	98	19b. TELEPHONE NUMBER (Include area code) 410-278-0319

Contents

List of Figures	v
List of Tables	x
Acknowledgments	xi
Executive Summary	xiii
1. Introduction	1
2. Objective	3
3. Ongoing Hypothesized Injury Mechanisms	3
4. Overall Technical Approach	4
5. Accomplishments	6
5.1 ARL Novel In Vitro Indoor Real Explosive Blast-Induced Injury System	6
5.1.1 Introduction	6
5.1.2 ARL In Vitro Blast-Induced Injury Model to Study Primary Real Explosive Blast Effects on Neurons and Tissue Slices	7
5.1.3 Results	10
5.1.4 Discussion	16
5.2 Effects of Primary Blast Pressure Waves Generated by Detonation of Small Explosive Spherical Charges on Neurons	16
5.2.1 Introduction	16
5.2.2 Materials and Methods	17
5.2.3 Results	19
5.2.4 Discussion	26
5.3 Quantum Dot (QD) Targeting to Specific Neural Cells	28
5.3.1 Introduction	28
5.3.2 Experimental	29
5.3.3 Results	30
5.3.4 Preliminary Conclusions	31

5.4	Computational Investigation of Blast-Wave Impact on Dissociated Neurons Placed in an Aquarium	32
5.4.1	Introduction	32
5.4.2	Computational Methods and Procedures	32
5.4.3	Results	33
5.4.4	Discussion	39
5.5	Damage in Spherical Cellular Membrane Generated by the Shock Waves: Coarse-Grain Molecular Dynamics Simulation of Lipid Vesicle	39
5.5.1	Introduction	39
5.5.2	Models and Methods	41
5.5.3	Results	45
5.5.4	Discussion	55
5.6	Impact of Blast-Dependent Cellular Damage on the Local Field Potential (LFP) in a Large-Scale Simulation of Cerebral Cortex Modeling Simulation	56
5.6.1	Introduction	56
5.6.2	Materials and Methods	57
5.6.3	Results	59
5.6.4	Discussion	65
6.	Conclusions and Future Studies	66
7.	References	69
	Appendix A. Unpublished Work	75
	Appendix B. Journal Publications	77
	List of Symbols, Abbreviations, and Acronyms	79
	Distribution List	81

List of Figures

Fig. 1	DSI overview technical approach	5
Fig. 2	Schematic of the experimental setup showing the positions of cyclotrimethylenetrinitramine (RDX) explosive charge, aquarium tank, and sample.....	7
Fig. 3	Blast-induced injury of cells: A) aquarium tank, B) face-on pressure measurement setup, and C) side-on pressure measurement setup. Both B) and C) show the location of pressure sensors with samples submerged in aquarium tank before each test.....	7
Fig. 4	Standoff distance measurement from an explosive charge to the location of testing sample	8
Fig. 5	In-vitro real blast impact experimental setup showing high-speed camera, aquarium, focusing lens, and arc lamp as a light source	9
Fig. 6	View from the perspective of the Photron Fastcam SA5 high-speed camera	9
Fig. 7	Spherical RDX charge: a) matching hemispherical charges b) fully assembled 1.7-g spherical charges	10
Fig. 8	A typical side-on pressure-time history signature recorded in air at 350-mm standoff distance.....	11
Fig. 9	Pressure histories in water at 350-mm standoff distance from RDX explosive. A) Face-on pressure profile and B) side-on pressure profile.....	12
Fig. 10	The blast wave arrival images from $t = 0$ to 0.30 ms.....	14
Fig. 11	High-speed images of the blast wave arrival images from $t = 0.30$ to 0.65 ms after the initiation	15
Fig. 12	Membrane permeability changes as a function of LDH release of PC12 neurons exposed to explosive blast (ca. 25 psi). Control cells remained in the incubator during the entire experiment, sham cells were transported to blast site but were not injured. * $p < 0.05$ compared to 1 blast, sham, and control, $n = 3$	20
Fig. 13	Membrane permeability changes as a function of calcein dye uptake of PC12 neurons exposed to explosive blast (ca. 25 psi). Control cells remained in the incubator during the entire experiment, sham cells were transported to blast site but were not injured. * $p < 0.05$ compared to sham and control, $n = 3$	20
Fig. 14	Viability of PC12 neurons after exposure to explosive blast (ca. 10 psi). Control cells remained in the incubator during the entire experiment, sham cells were transported to blast site but were not injured. I) Viability of PC12 cells 24 h after blast injury as determined by a live/dead assay: A) Control, B) sham cells, and C) injured cells subjected to a single blast. Live cells appear green due to calcein AM	

	dye trapped inside. The nuclei of dead cells appear red due to ethidium homodimer-1 staining. Arrows denote selected dead cells. Scale bars represent 100 μm . Inset displays magnified image of dead cells. Inset scale bar represents 50 μm . II) Viability of PC12 cells 2 and 24 h after blast injury calculated from live/dead assay. $*p < 0.05$21
Fig. 15	Viability of PC12 neurons after exposure to single and multiple explosive blasts. Samples denoted 1 Blast were exposed to 19 psi. Samples denoted 2 Blasts and 3 Blasts were exposed to ca. 24, 14, and 9 psi (row 1, row 2, row 3). Multiple blasts were separated by 5–7 min intervals. Control cells remained in the incubator during the entire experiment, sham cells were transported to blast site but were not injured. I) Viability of PC12 cells 24 h after exposure to single and multiple explosive blasts as determined by a live/dead assay: A) injured cells exposed to single blast of ca. 9 psi, B) injured cells exposed to 2 blasts of ca. 9 psi separated by ca. 5 min, and C) injured cells exposed to 3 blasts of ca. 9 psi separated by ca. 5 min. Live cells appear green due to calcein AM dye trapped inside. The nuclei of dead cells appear red due to ethidium homodimer-1 staining. Arrows denote selected dead cells. Scale bars represent 100 μm . Inset displays magnified image of dead cells. Inset scale bar represents 50 μm . II) Viability of PC12 cells 24 h after blast injury calculated from live/dead assay. $*p < 0.05$ compared to control, sham and 1 Blast.23
Fig. 16	Morphology of PC12 cells 24 h after exposure to a single explosive blast of ca. 10 psi. A) Control cells that remained in the incubator during the experiment, B) sham cells that were transported to blast site but were not injured, and C) injured cells subjected to a single blast. Arrows denote locations of selected axonal beads. Scale bars represent 50 μm . Inset displays magnified image of beads. Inset scale bars represent 10 μm24
Fig. 17	Morphology of PC12 cells 24 h after exposure to a single and multiple explosive blasts of ca. 10 psi. A) Injured cells subjected to a single blast, B) injured cells subjected to 2 blasts separated by ca. 5 min, C) injured cells subjected to 3 blasts separated by ca. 5 min. Arrows denote locations of selected axonal beads. Scale bars represent 50 μm . Inset displays magnified image of beads. Inset scale bars represent 10 μm24
Fig. 18	Schematic showing axonal beading that can occur after blast injury ..25
Fig. 19	Structures of Concanavalin A dimer and Disuccinimidyl suberate.....28
Fig. 20	Reaction scheme for producing the QD-lectin conjugate29
Fig. 21	QD-Con A conjugate uptake in mixed neuronal cultures. Red arrows: microglia with QDs; blue arrows: neurons (no QD uptake observed).....30
Fig. 22	Microscopy of microglia QD accumulation at higher magnification (630 \times).....31

Fig. 23	a) Dissociated neurons in 24-well plate embedded in water-filled aquarium and b) 2-D numerical setup of experiment showing bird's-eye view of 24-well plate immersed in water-medium contained by aquarium walls and surrounded by air with RDX explosive at specified standoff distance.....	33
Fig. 24	Model calculations validated with blast experiments showing RDX explosive pressure histories: a) in air at 325-mm explosive standoff and b) in water-filled aquarium at 300-mm standoff	34
Fig. 25	Shock pressure histories in aquarium (PMMA) material at the front entrance exhibited peak pressure of 173 psi resulting from detonation of RDX explosive positioned at 125-mm standoff distance. The pressure wave transition from air produced increase pressure or a jump condition in the PMMA material from the nonshocked to shocked state. Peak pressure is only maintained for a very short period of time (a few milliseconds) before relaxing approximately to preshock conditions after 0.25 ms.....	35
Fig. 26	Evolution of pressure waves from detonated RDX explosive positioned 125 mm in front of aquarium. The pressure waves propagate through the aquarium walls, into the water medium and impact the neurons in the 24-well plates. Tracer particles (such as those shown 1, 2, and 3) are used to capture the strength of the pressure waves in the 24-well pack.	35
Fig. 27	Calculated pressure histories in the first row of 24-well pack for tracers 1–3 from Fig. 26 for a 325-mm standoff distance from RDX explosive. a) Pressure histories in the well ID at the tracer 1 position experienced a peak pressure of 31.5 psi loading, followed by lower-strength secondary reflected pressure waves. b) Pressure histories in the well ID at tracer 2 position produced peak loading of 26.5 psi, followed by strong secondary reflected pressure waves. c) Pressure histories in well ID at tracer 3 experienced strengthened reflected secondary pressure waves (peak 35.5 psi). Arrows indicate peak pressures entering 24-well plates.	36
Fig. 28	The effect of standoff distance on calculated peak overpressure in the 24-well pack due to RDX blast impact	37
Fig. 29	Fluorescence intensity vs peak pressure in the 24-well pack	38
Fig. 30	Impact of pressure loading on a) cultured dish containing PC-12 neurons, b) photograph of multiple PC-12 neurons (40X magnification), and c) finite element model of exhibit mechanical response of single PC-12 neuron	38
Fig. 31	Mechanical response of PC-12 neurons: a) pressure loading and b) von Mises stress	39
Fig. 32	a) A representative snapshot of the liposome surface (left) and cross-sectional area of the lipid vesicle (right): the liposome is composed of 5,551 lipids. H, T, and W particles are colored red, yellow, and blue, respectively. The liposome has a radius of 10 nm (14.5 r_c in DPD	

	units). b) A representative cross-sectional area of the simulation box after initial compression.....	42
Fig. 33	The supersonic shock wave at the various distances from its launch. The liposome is located at 117.4 nm. The Mach number is 1.49. b) The pressure profile at $t = 150$ ns after the wave initiation at the liposome location.....	46
Fig. 34	The shock wave at the location of the liposome for the various piston speeds v_p and b) movement of the center of mass of the liposome in z direction	48
Fig. 35	Change of liposome size and shape vs. time: a) radius of gyration of the liposome, R_g and b) asphericity.....	50
Fig. 36	The shock wave at the location of the liposome for the various piston speeds v_p . b) Movement of the center of mass of the liposome in z direction.	51
Fig. 37	Change of liposome size and shape vs. time: a) radius of gyration of the liposome, R_g , and b) asphericity, b	52
Fig. 38	The snapshot of a pore in the hydrophobic layer of the lipid vesicle, W and H beads removed for clarity. b) Schematic of possible damage of the hydrophobic layer.	53
Fig. 39	Schematic representation of our method. a) Two large clusters are present; they are composed from adjacent outer and inner layers and colored in red and blue, respectively. Small cluster voids are in grey. b) The liposome has a pore, and one large cluster in red is present along with some number of small clusters.....	53
Fig. 40	Number of voids in the hydrophobic layer as function of pressure profile shows the change in the number of voids in the hydrophobic layer, N_v , with time, t , during propagation of the shock wave for our systems with low overpressure peaks	54
Fig. 41	Number of voids in the hydrophobic layer as function of pressure profile.....	55
Fig. 42	Overview of cortical network model and output. a) Visual representation of the model, showing 549 cortical neurons with layer boundaries depicted as discs. b) High-pass filtered LFP for the baseline (undamaged) model shows distinct clusters of spikes. c) Low-pass filtered LFP shows slow oscillations similar to those seen in EEG. d) Parametric power spectrum shows relatively low power in higher frequencies, again similar to electrocorticography (ECoG) and EEG. 59	
Fig. 43	Comparison between baseline model output (gray) and damaged model output (color). Each row shows how the model activity changes as a function of increasing the percentage of damage to the cell membranes, ranging from 10%–50% in increments of 10%. Potential is shown in arbitrary units for the 0.5 s of model data (total simulation time 19 s). a–e) High-pass filtered model outputs designed to mimic extracellular recording techniques to measure action potential	

frequency. f–j) Low-pass filtered model output designed to mimic the LFP. Note reduction in amplitude and duration of low frequency activity.....61

- Fig. 44 Effects of cell membrane damage on spectral power of model. Across both subplots, colored lines represent change in the power spectrum with increasing levels of damage to the cell membrane (black is baseline, damage increases from blue to red in increments listed in legend). a) Effect of damage to the whole cell. b) Difference in spectral power of model between baseline (undamaged) and damage to the whole cell. Each line plots the overall reduction in power/decibels between the baseline (undamaged) model and models with increasing percentage of damage to the cell membrane. As expected, increased damage led to increased reduction in power as indicated by the negative values. Model shows larger decrease in low-frequency power due to membrane damage.63
- Fig. 45 Difference in spectral power of model due to damage to axons and soma/dendrites. Damage is modeled as changes to specific compartments of the model that comprise either simulated axons or simulated somas and dendrites. a) Effect of selective damage to only the axonal compartments of the cell. b) Reduction in power from baseline for axonal damage. Low-frequency power is reduced to a greater extent than high-frequency power. c) Effect of selective damage to the soma and dendrite compartments of the cell. d) Reduction in power from baseline for damage to somal and dendritic compartments of the model. Minor damage (10%) is associated with a small increase in low-frequency power. More damage (4%–50%) causes a drop in low-frequency power. b) and d) Comparing these plots reveals that damage to the soma and dendrites results in greater power reductions in high frequencies at smaller percentages of damage (10%–30%) while damage to the axon reduces power in the low frequencies at all damage levels (10%–50%) and also at high frequencies for larger values of percent damage (40%–50%).64

List of Tables

Table 1	Classification of TBI severity	2
Table 2	Peak side-on experimental pressures in water at selected standoff distances	13
Table 3	Quantification of axonal beading observed in PC12 neurons 24 h after exposure to explosive blast.....	25
Table 4	Calculated peak pressure distribution in 24-well plate columns (psi) .	36
Table 5	The interaction parameters a_{ijDPD} between pairs of beads where i and j belong to head (H), tail (T), or water (W) beads, respectively	43
Table 6	Neuronal firing rate.....	65

Acknowledgments

The US Army Research Laboratory funded this effort through the FY13 Director's Strategic Initiatives Program.

The authors would like to thank Dr Matthew Biss for his generous help with the experimental setup, Dr Kevin McNesby, Mr Stephen Aubert, Dr Brian Roos, Ms Stephanie Snead, Mr William H Mermagen, Mr James Rugarnus III, and Mr Vincent Boyle for providing critical technical inputs and their thoughtful technical discussion; Mr Terry Piatt and Ms Lori Pridgeon for preparing cyclotrimethylene trinitramine (RDX) spherical charges; Mr Ronnie Thompson, Mr William Sickels, Mr Eugene Summers, and Mrs Deborah Pilarski for their assistance during the small-scale blast testing; Prof Ben Bahr and Dr Marquitta Smith (University of North Carolina-Pembroke) for blast-induced tissue injury testing and analysis.

The authors would like to thank Prof Gregory Elder, MD (James J Peters, Veterans Affairs Medical Center, New York), Prof Josh Duckworth, MD, CDR (Uniformed Services University of the Health Sciences, Bethesda Maryland [USU]), and Prof Joseph McCabe (USU) for their support, mentorship, and their thoughtful clinical discussion on mild traumatic brain injury research; Dr Frederick Gregory (Army Research Office) for his encouragement and support of this project.

INTENTIONALLY LEFT BLANK.

Executive Summary

A multidisciplinary research project was initiated to enhance the fundamental understanding of brain structural and functional injury mechanisms associated with mild blast events on neuronal cell cultures. Two foundational infrastructure capabilities were realized, but more critically, in-house expertise was developed to execute the research and enable the future Army capability. The first accomplishment centers on cellular experimentation. A novel experimental research platform was developed to examine the effects of explosive pressure impacts on neurons, and this indoor in-vitro experimental research program uses real explosives (not shock tube) to study the impact of blast on dissociated neurons. The experimental results found transient damage to the neuronal cell membranes that modulate neurotransmitter release that is necessary for brain signals to generate and carry information between brain regions. The second accomplishment focuses on a multiscale, computational brain model implemented in a framework known as GENESIS with parallel processing, where the research team parameterized a brain model to simulate the results from the cellular experiments. Using the model to examine the effect of cellular membrane on the coordinated functional activity of tens of thousands of neurons, the research results revealed that neuronal injury effects on the cells disrupted the coordinated, low-frequency activity of brain signals hypothesized to underlie behavioral performance.

This multidisciplinary research project was initiated to enhance the fundamental understanding of brain structural and functional injury mechanisms associated with mild blast events on neuronal cell cultures. This basic research initiative bridges cellular brain responses with higher-order brain networks in support of a long-term goal to achieve a 2040 capability for improved Soldier protection designs that can prevent behavioral performance decrements by mitigating low-level traumatic brain insults. The brain model serves as the basis for several fiscal year 2016 projects that study brain structure-function relationships in healthy individuals in alignment with the US Army (Acquisition, Logistics and Technology) (ASA(ALT)) 6.1 funding for Cybernetics. These new modeling projects are aligned with the Future Force Operating Concept, specifically Army Warfighter challenges to enhance training and improve Soldier, team, and leader performance.

INTENTIONALLY LEFT BLANK.

1. Introduction

According to the Defense and Veterans Brain Injury Center, as of 8 December 2015, nearly 340,000 Soldiers worldwide have been medically diagnosed with traumatic brain injury (TBI) since 2000. Nearly 82.5% of injured Soldiers are suffering from mild traumatic brain injury (mTBI). TBIs in theater are frequently caused by explosive blasts that initiate a series of neuronal biochemical changes, often resulting in reduced brain/nervous system function and/or cell death. Explosive blast-induced injury represents an injury mechanism that is distinct from nonblast forms of injury. An explosive blast impact may result in 4 types of independent mechanisms of injury: primary, secondary, tertiary, and quaternary effects. Primary blast injury refers to the direct effect of the blast itself. Secondary blast effects refer to injuries that are sustained as a result of debris being projected toward the body. Tertiary blast injuries occur as a result of the body being displaced as a result of blast. Quaternary blast injury refers to burns, toxic exposure, and other potential effects of the explosion.¹

Table 1 is the criteria that clinicians use to determine the severity of TBI. According to Table 1, mTBI is defined as a traumatically induced structural or physiological disruption of brain function immediately following the traumatic event and is indicated by the onset of following clinical signs: alteration in consciousness, not prolonged, no/brief loss of consciousness, and no intracranial findings on imaging.² Diagnosis of mTBI caused by primary explosive blast is challenging, as it is not easy to clinically separate blast from nonblast mTBI on the basis of symptoms. Damage to brain tissue progresses slowly and in a manner that is generally undetectable by conventional imaging.^{1,3} The effects of blast waves on tissue are still poorly understood. The threshold pressure loading levels required to induce damage and the cumulative effects upon multiple exposures are not well characterized. Further, it is largely unknown how structural damage from the mechanical loading impacts the functional activity of the cell at variable timescales after the TBI event.⁴

Table 1 Classification of TBI severity

(If a patient meets criteria in more than one category of severity, the higher severity level is assigned)			
Criteria	Mild	Moderate	Severe
Structural imaging	Normal	Normal or abnormal	Normal or abnormal
Loss of consciousness (LOC)	0–30 min	>30 min and <24 h	>24 h
Alteration of consciousness /mental state (AOC) ^a	up to 24 hours	>24 hours; severity based on other criteria	
Posttraumatic amnesia (PTA)	0–1 day	>1 and <7 days	>7 days
Glasgow Coma Scale (GCS) (best available score in first 24 h) ^b	13–15	9–12	<9

Note: Source: VA/DoD Clinical Practice Guideline for the Management of Concussion Mild Traumatic Brain Injury, February 2016

^a Alteration of mental status must be immediately related to the trauma to the head. Typical symptoms would be looking and feeling dazed and uncertain of what is happening, confusion, and difficulty thinking clearly or responding appropriately to mental status questions, and being unable to describe events immediately before or after the trauma event.

^b In April 2015, the DoD released a memorandum recommending against the use of GCS scores to diagnose TBI. See the memorandum for additional information. [Assistant Secretary of Defense. Traumatic brain injury: updated definition and reporting. Washington (DC): Department of Defense; 2015.]

Most of the previous studies have involved the whole animal and head acceleration or some other type of movement (tertiary blast) in addition to primary blast. While most victims of TBI may experience secondary (impact) or tertiary trauma in addition to the blast wave, a thorough understanding of primary blast injury is needed.⁵ Various models have been developed to gain insight into the injury mechanisms from primary blast exposure including the use of hydrostatic pressure, a barotrauma chamber, and compression.^{6–9} It is difficult to compare these methods to one another and to in vivo models using shock tubes because the mechanisms of injury are different.¹⁰ Generally, these models have longer pulse duration and lower pressures. Arun et al.¹¹ and Effgen et al.¹² recently reported the use of shock tubes for in-vitro models of SH-SY5Y cells and organotypic hippocampal tissue slices, respectively. While shock tubes can mimic peak overpressure, impulse, and duration of the positive pressure phase, they do not reliably produce the negative pressure rarefaction events that are observed from explosions. In addition, injuries from shock tubes are often more severe and complex than those observed from live explosives.¹³

Currently there is no in-vitro experimental model with blast pressure waves generated by using real explosives in the laboratory for investigating the effects of primary blast-induced TBI. Furthermore, given the limitations of current neuroimaging methodologies, relationships between cellular changes and large-scale brain network effects have been difficult to elucidate. Large-scale simulation modeling provides a promising avenue to explore these relationships. Research on the neural underpinnings of TBI has primarily focused on large-scale morphological changes such as axonal degeneration and/or neuronal morbidity.¹⁴

Hence, it is critical to develop a novel in-vitro indoor experimental model that uses real military explosive charges to more accurately represent battlefield blast explosives and to study 1) whether blast from real explosives is any more or less injurious than from a shock tube; 2) how functional and structural alteration or damage at the cellular and tissue levels following real explosive blast impacts cognitive performance for future improvement of detection and subsequent treatment of mTBI, as well as improving personal blast protection equipment for our Soldiers.

2. Objective

The objective of this project is to enhance the fundamental understanding of the brain structural and functional injury mechanisms associated with mTBI by bridging cellular structural and functional responses with higher-order brain networks. This long-term vision to bridge across spatial scales will enable us to understand how cellular changes impact cognitive performance.

3. Ongoing Hypothesized Injury Mechanisms

We hypothesize that when neurons are exposed directly to a real explosive blast pressure wave, biochemical changes at the cellular level cause membrane damage and neurotransmitter release that eventually disrupt neural networks and compromises brain function.

- *Hypothesis 1: Subcellular level*
 - Membrane permeability changes; transient pore openings allow for increased ionic transport
- *Hypothesis 2: Cellular level*
 - Increased influx/efflux of sodium and calcium ions can cause osmotic swelling and cytoskeletal damage such as axonal beading

- Increased reactive oxygen species production due to cerebral vascular dysfunction
- Axonal degradation
- *Hypothesis 3: Network level*
 - Damaged structural connectivity
 - Altered functional activity
- *Hypothesis 4: Cellular damage after blast exposure could induce electrophysiological changes that negatively impact brain function in the absence of significant structural changes.*

4. Overall Technical Approach

The US Army Research Laboratory (ARL) research team takes advantage of a unique capability to use controlled real explosive blast and developed the unique in-vitro indoor experimental platform that uses real military explosive charges to accurately represent battlefield blast exposure and to probe the effects of primary explosive blast on dissociated neurons. The ARL Director's Strategic Initiative (DSI) team is one of only few known groups in the world studying real explosive blast impacts at the cellular level. The research is also to take advantage of the high-performance computing capabilities available at ARL to model the brain across spatial scales to understand both structural and functional effects of traumatic insults and to link results across scales and connect neural injury to changes in behavior (Fig. 1).

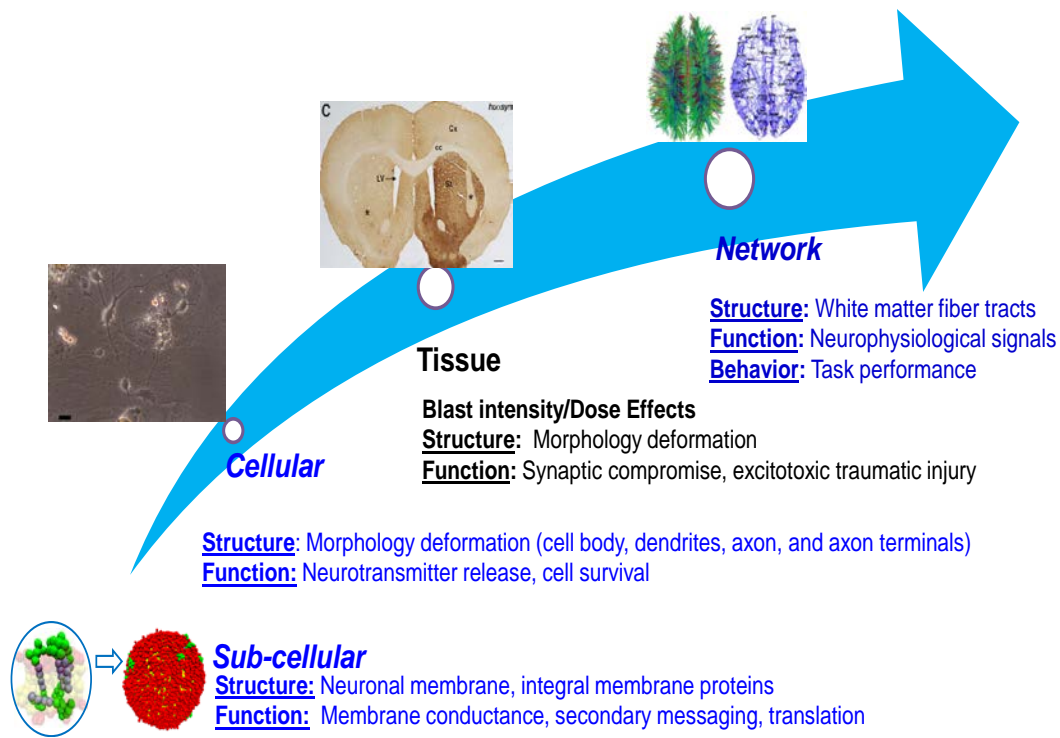


Fig. 1 DSI overview technical approach

The experimental approach is to fabricate 3-dimensional (3-D) cultures of neurons and supporting cells using a biocompatible nanofibrous scaffold, target the neural membrane with bioconjugated sensing particles to study neurotransmitters release, expose the cultures to different levels of explosive blast, and examine the cellular structural and functional changes. Pressure profiles, cellular viability, reactive oxygen species release, and membrane permeability changes are measured to build multiscale predictive models. On the cellular scale, we develop a novel model experimental system combined with 3-D cellular analysis and simulation tools for the study of neuronal injury following realistic blast and blunt trauma events. At the network scale, research focuses on structural and functional connectivity relationships that can predict differences in task performance. Across scales, research employs a multiscale model with parameters tied to multiple levels so that effects of changes/damage to these parameters can be examined on large-scale brain networks (i.e., effects on behavior). Our research explores the physiological impact of blast-induced pore formation on simulated network function in a large-scale simulation of the cerebral cortex.

5. Accomplishments

5.1 ARL Novel In-Vitro Indoor Real Explosive Blast-Induced Injury System

5.1.1 Introduction

While there is extensive literature on blast-induced brain injury, there is a lack of relevant reproducible models, including the availability of highly controlled blast-wave generators. Therefore the mechanisms for such injuries have been difficult to analyze and compare across studies, thus impeding progress in detection and treatment of these ailments.³ In addition, most clinical data of blast trauma involves secondary trauma (impact, blunt forces), making data of injury due to primary blast alone limited.¹⁵ In particular, in-vitro models that allow for the deconvolution of numerous molecular mechanisms of cell defense are scarce.⁴ Recently, there has been some in-vitro work done with shock tubes. Arun et al. examined the effect of shock waves on neuroblastoma and glioblastoma cells.¹¹ Effgen et al. developed an in-vitro shock tube model using organotypical hippocampal slices.¹² Hue et al. examined the effect of shock waves on brain endothelial cells.^{16,17} While this work is extremely useful in elucidating possible mechanisms of injury from primary blast, the pressure profile generated from such devices does not match that of most CHNO-based explosives. In particular, shock tubes typically lack the positive pressure phase duration and below-ambient pressure phase generated by chemical (and nuclear) explosives, necessitating direct tests using primary blast agents.^{9,12} Furthermore, most CHNO-based explosives or conventional military explosives release light, acoustic, thermal, and electromagnetic energies, as well as toxic fumes. Thus, there is need for in-vitro models using realistic blast to more accurately depict battlefield blast exposure. To the best of our knowledge, we are the first group to present such a model.

During the 3 years of the effort described here, the ARL research team developed the unique in-vitro indoor experimental platform that uses military explosive charges to accurately represent battlefield blast exposure and to probe the effects of primary explosive blast on dissociated neurons and tissue slices. In this report, we focus mostly on the primary blast effects on PC12 neurons.

5.1.2 ARL In-Vitro Blast-Induced Injury Model to Study Primary Real Explosive Blast Effects on Neurons and Tissue Slices

5.1.2.1 Setup

All explosive tests were performed in a 6- × 10- × 6-m blast room certified for testing up to 25 g of explosive. Figure 2 shows a schematic of the overall experimental setup. Neuronal cell cultured samples or tissue slices were contained in a water-filled aquarium (30.5 × 34.5 × 65 cm, poly (methyl methacrylate) [PMMA] construction aquarium) (Fig. 3a). The thickness of the aquarium walls was 0.2 cm. The tank was filled with water maintained at 37 °C by a heating element coupled to a small stirring device. The clear walls of the aquarium enable a visual record of the water shock passage and its interaction with the cell cultured samples.

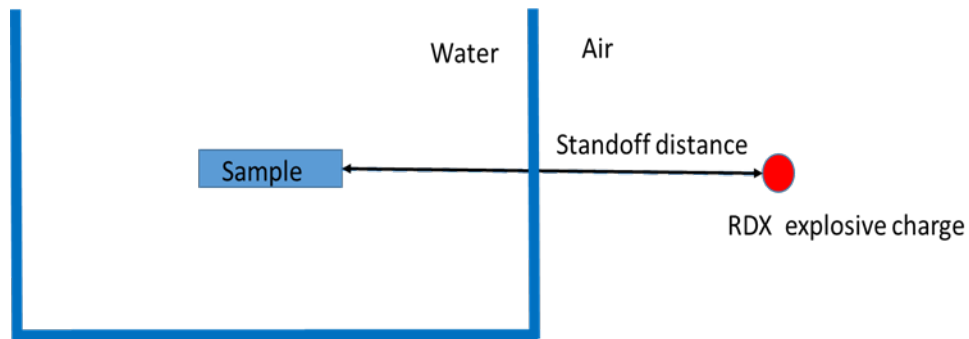


Fig. 2 Schematic of the experimental setup showing the positions of cyclotrimethylenetrinitramine (RDX) explosive charge, aquarium tank, and sample

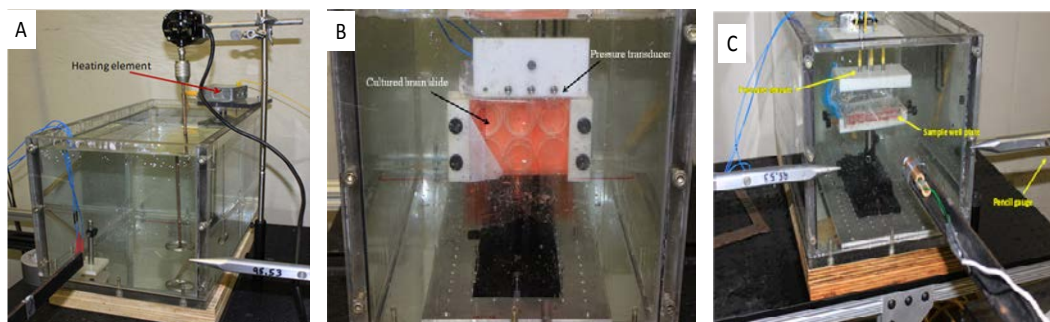


Fig. 3 Blast-induced injury of cells: A) aquarium tank, B) face-on pressure measurement setup, and C) side-on pressure measurement setup. Both B) and C) show the location of pressure sensors with samples submerged in aquarium tank before each test.

Three piezoelectric high-frequency dynamic pressure sensors (ICP model 102A, PCB Piezotronics Inc., Depew, NY) were modified for underwater use and used to measure the shock wave pressure histories at a position of 2 cm above the cultured samples using a custom-designed pressure gauge holder. For tissue slice blast impact study, all pressure gauges were mounted on top of the tissue sample bag, submerged in the aquarium approximately 4 inches under water, and positioned face-on to the blast wave direction (Fig. 3b). For cellular blast impact study, all pressure gauges were mounted on top of the cell culture plate with a custom-designed lid, submerged approximately 4 inches underwater, and positioned side-on to the blast wave direction. The caps were designed such that the pressures in different rows or columns of the well plate could be measured by moving the pressure sensors to the desired locations (Fig. 3c). Two free-field air-blast pencil probes (ICB model 137A23, PCB Piezotronics Inc., Depew, NY) were positioned in front of the aquarium to measure the free-field air-shock pressure before the shock wave entered the water medium (Fig. 3c). Pressure-time history traces and peak overpressure were recorded for each blast.

The charge standoff distance to a sample was measured as the distance between the charge and the outer wall of the aquarium (Fig. 4).

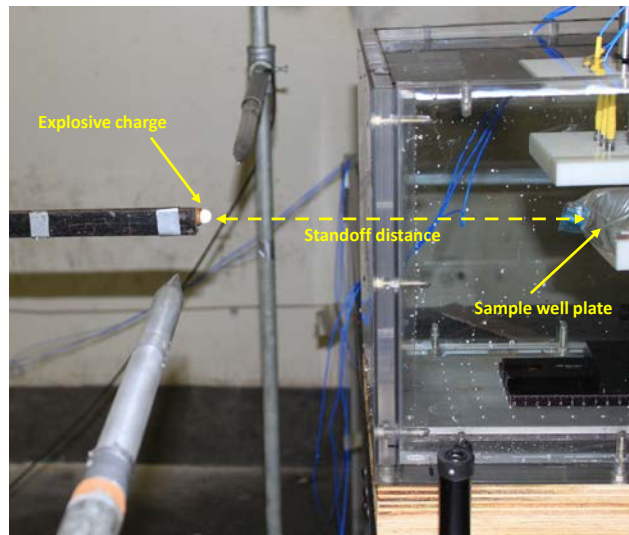


Fig. 4 Standoff distance measurement from an explosive charge to the location of testing sample

The overall experimental arrangement is depicted in Fig. 5. The shock wave produced by the detonation of a RDX spherical charge was captured by high-speed video camera images with a resolution of $1,024 \times 64$ pixels using a Photron FASTCAM SA5 Model 1300K-C3 (Photron USA, Inc., San Diego, CA). The camera frame rate was 100,000 frames per second with an exposure time of 368 nanoseconds per frame. Figure 6 shows the view from the Photron FastCam SA5

Approved for public release; distribution is unlimited.

high-speed camera location. The line-of-sight of the high-speed camera was parallel to the plane of the sample holder. The visualization of the blast wave passing over and through the sample was recorded in a direction perpendicular to the air blast direction of propagation.

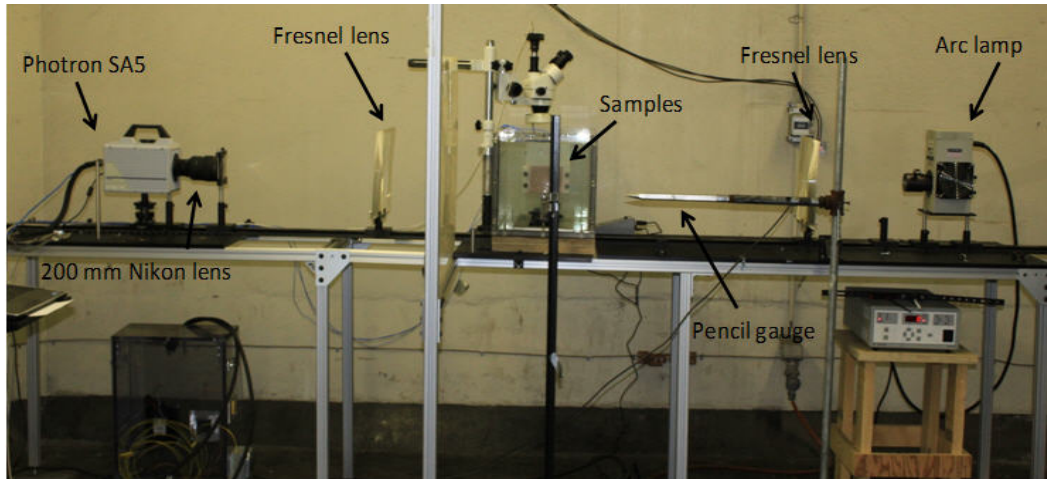


Fig. 5 In-vitro real blast impact experimental setup showing high-speed camera, aquarium, focusing lens, and arc lamp as a light source

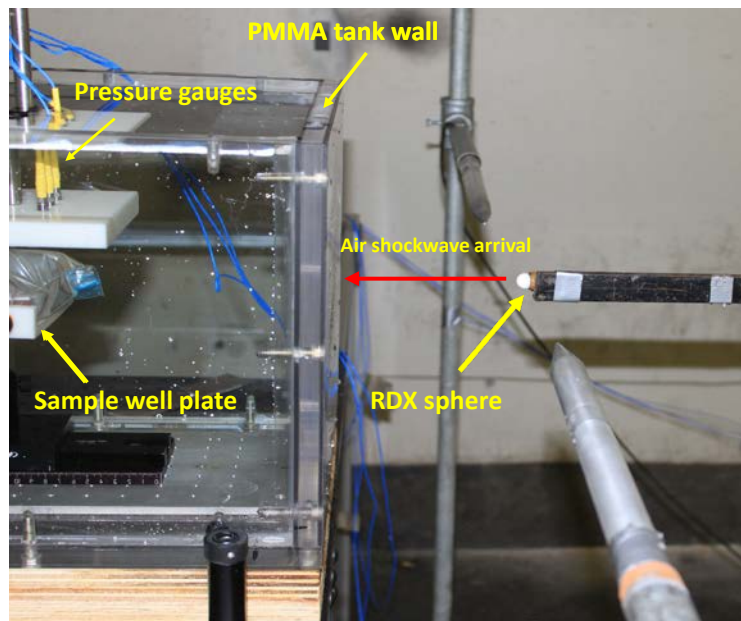


Fig. 6 View from the perspective of the Photron Fastcam SA5 high-speed camera

5.1.2.2 Explosive Charges

Spherical cyclotrimethylene trinitramine Class 5 ($C_3H_6N_6O_6$; RDX Class V, 1.7-g weight) charges are composed of matching hemispherical charge and used to generate the primary blast. RDX has an IUPAC name of 1,3,5-trinitroperhydro-1,3,5-triazinean. Each hemispherical charge has a nominal mass of 0.85 g and is pressed to a density of 1.77 g/cm^3 (98.4 % theoretical maximum density, TMD). Figure 7a shows matching hemispherical charges and Fig. 7b shows an assembled spherical charge of RDX. The spherical RDX explosive charge detonates 116 cm above the ground with RP-87 detonators.

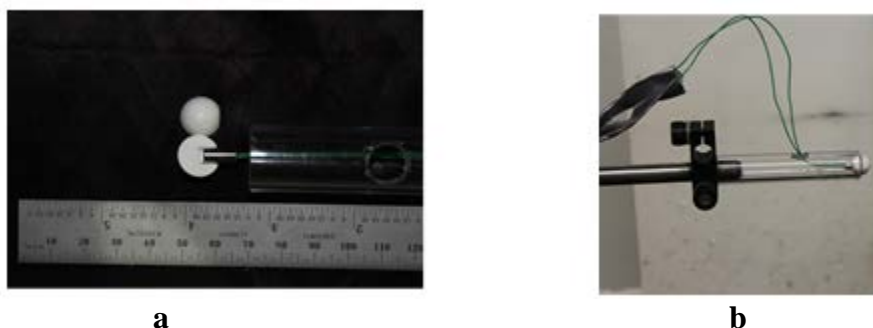


Fig. 7 Spherical RDX charge: a) matching hemispherical charges b) fully assembled 1.7-g spherical charges

5.1.3 Results

5.1.3.1 Pressure Measurements

The relative positions of RDX explosive charge, aquarium tank, and sample are shown in Fig. 6. Figure 8 illustrates a side-on pressure-time history (molecules in the leading shock are not reflected by the gauge element) observed in air at a 350-mm standoff distance from the point of initiation. As seen in Fig. 8, the pressure rises rapidly as the leading shock front passes over the gauge element to a peak value of approximately 13 psi, decays rapidly to ambient pressure, and then drops below ambient before returning to ambient conditions, with a total duration near 1 ms. The decrease in pressure to subambient is a signature of air explosions originating from a pseudo-point source.

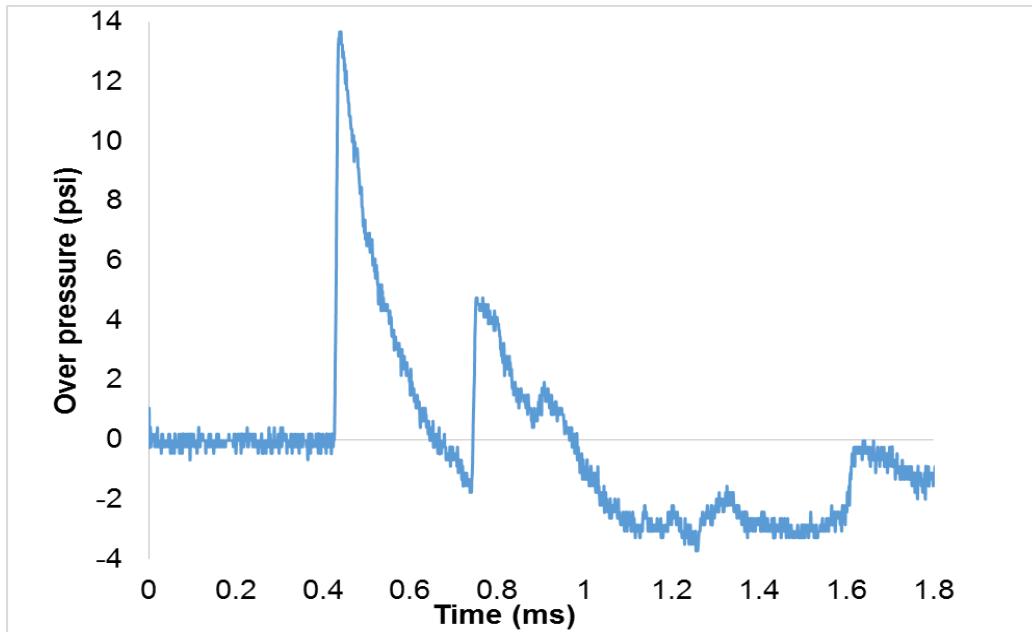


Fig. 8 A typical side-on pressure-time history signature recorded in air at 350-mm standoff distance

Figure 9a shows a face-on pressure-time history (molecules in the leading shock are reflected by the gauge element) observed in the water measured by pressure sensors placed on the extreme top of the tissue samples at a 350-mm standoff distance from the point of initiation. Air molecules pushed by expanding RDX detonation products create pressure waves, which in turn push against the PMMA aquarium surface at the air/PMMA interface, which in turn push against the water at the PMMA/water interface. The peak pressure in the water, likely propagated by an acoustic wave, was approximately 110 psi and decayed to zero (ambient condition) after approximately 100 μ s. Figure 9b shows a side-on pressure history in water measured above the sample well plate for the same standoff distance of 350 mm (see Fig. 3c for the location of the pressure gauges). The peak pressure was measured at 38.8 psi. The time duration of the pressure excursion was approximately 100 μ s. The initial pressure rise is considered the most important factor in the pathology of primary blast-induced injury.

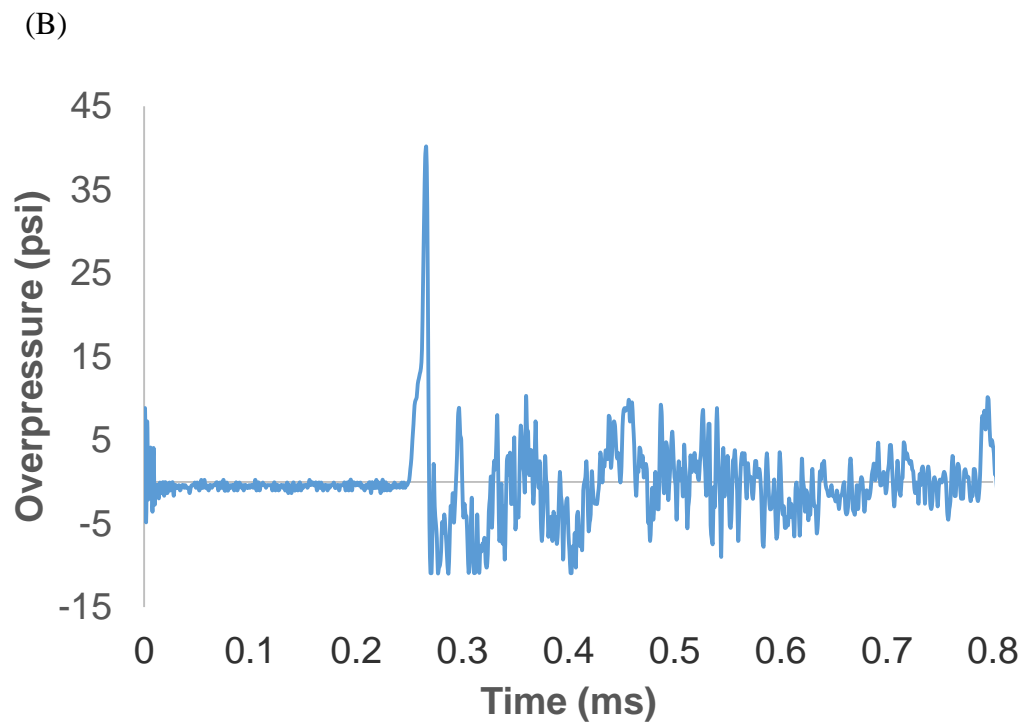
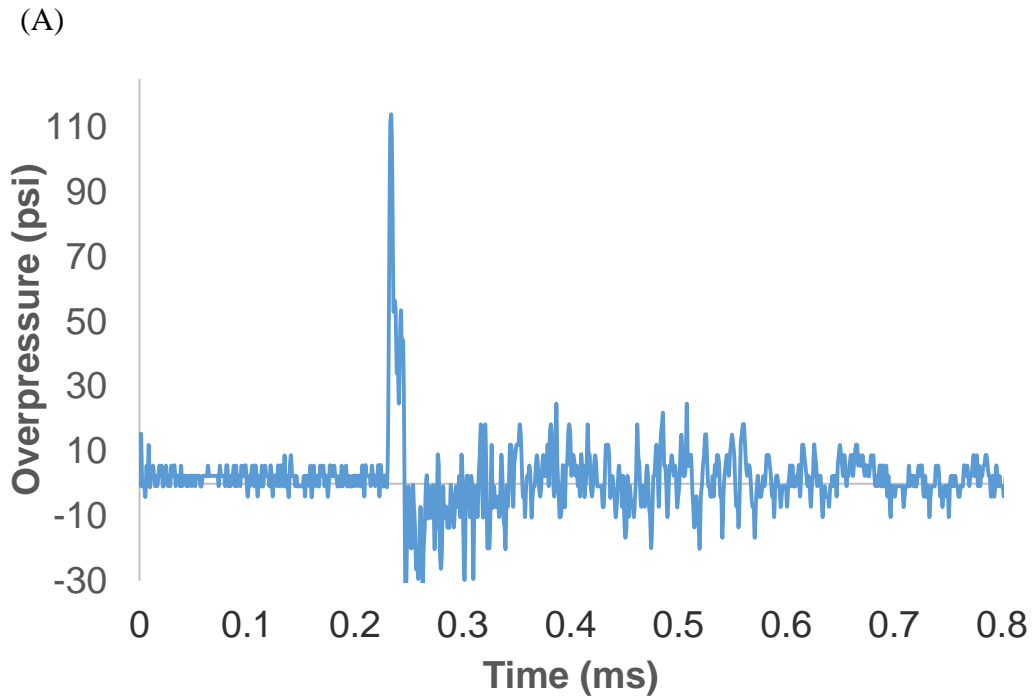


Fig. 9 Pressure histories in water at 350-mm standoff distance from RDX explosive. A) Face-on pressure profile and B) side-on pressure profile

Table 2 displays average pressure readings in water for a range of standoff distances. The pressure gauges were mounted above the sample well plate as shown in Fig. 6. The reproducibility was generally good, with standard deviations between 6% and 28% of the average pressure reading.

Table 2 Peak side-on experimental pressures in water at selected standoff distances

Standoff distance (mm)	Pressure (psi)
225	386.4 \pm 45
250	261.2 \pm 45
275	126.0 \pm 36
300	104.1 \pm 6.3
325	56.2 \pm 6.8
350	39.1 \pm 2.4

5.1.3.2 High-Speed Imaging Records of Blast Wave Impacts on Samples

Figures 10 and 11 show a series of high-speed digital images of the air-blast-induced pressure waves propagating through water. The pressure waves were generated from initiation of 1.7 g of an RDX sphere in air outside the aquarium. Figure 10 shows the blast pressure waves propagating from left to right in the aquarium and impacting the tissue samples at 0.21 ms. The impact on the tissue samples produces both transmitted and reflected pressure waves in the aquarium. This is evident at time of 0.30 ms. This combined complex pressure wave structure produces a yet unexplained bubble cloud possibly due to a cavitation phenomenon.

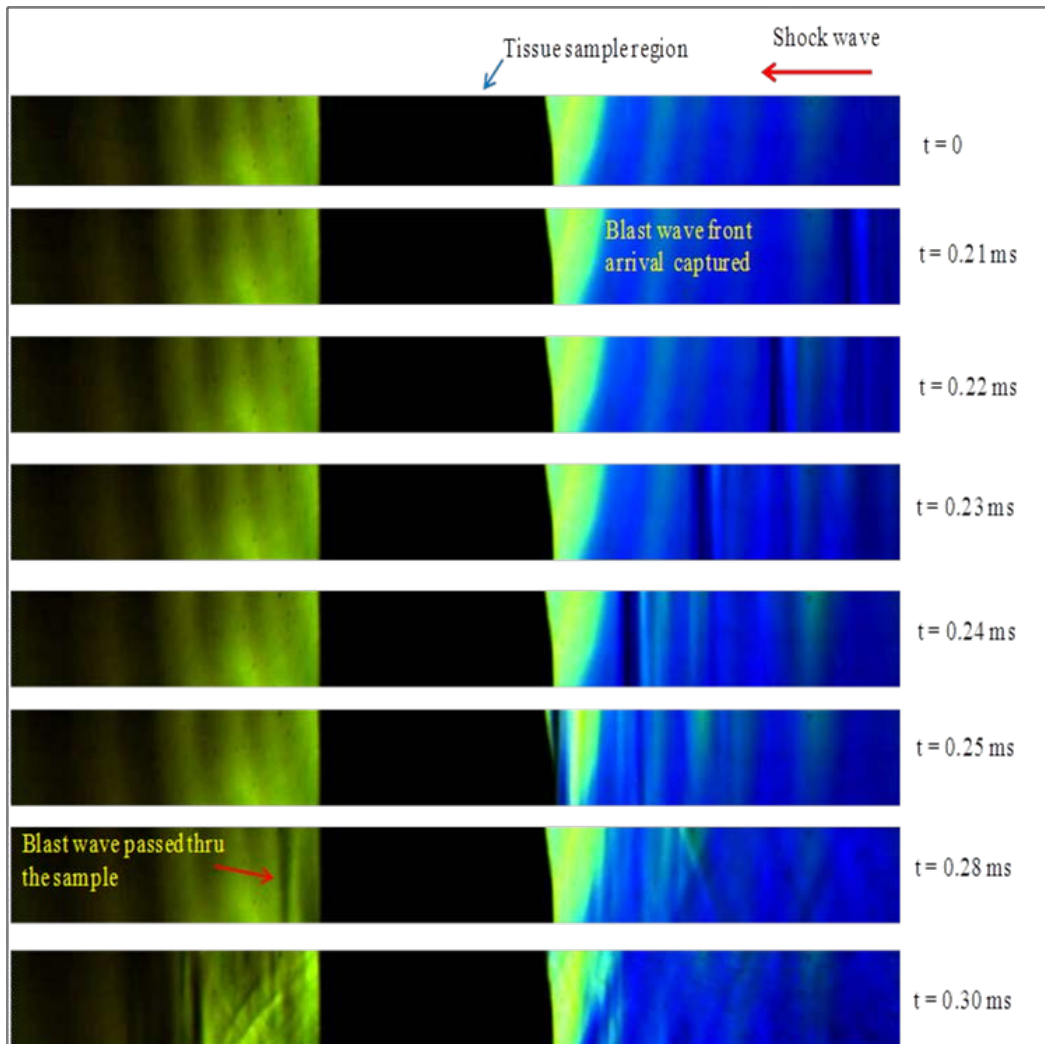


Fig. 10 The blast wave arrival images from $t = 0$ to 0.30 ms

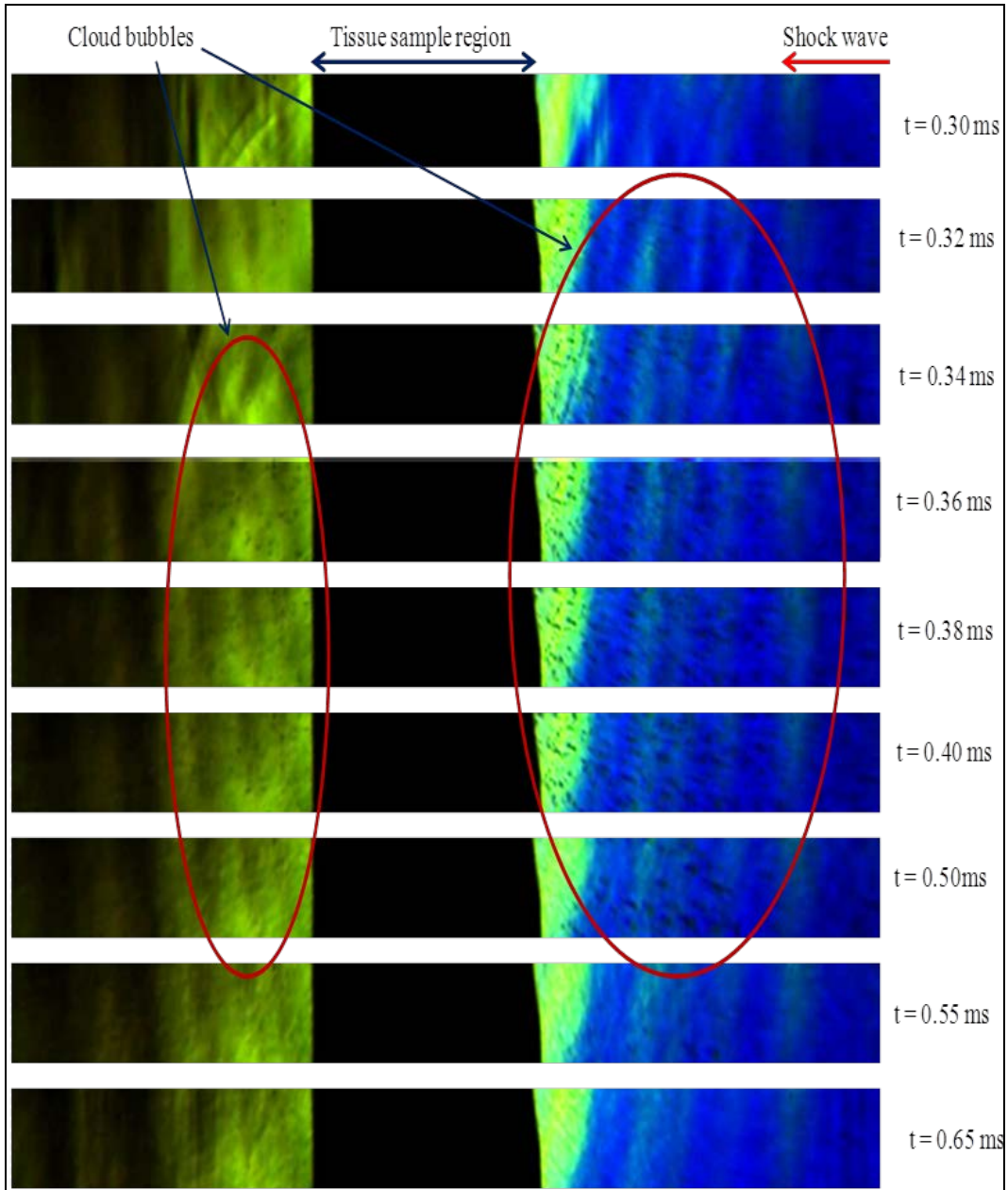


Fig. 11 High-speed images of the blast wave arrival images from $t = 0.30$ to 0.65 ms after the initiation

As shown in Fig. 11, the bubble cloud was captured at approximately 0.32 ms after the initiation. The bubble cloud dissipated completely about 0.6 ms after initiation. It can be seen from these sequences of images that the formation and disappearance of the bubble cloud are within a time span of approximately 0.3 ms. These are typical examples of the bubble cloud formation observed during these explosive blast experiments.

5.1.4 Discussion

To the best of our knowledge, we present the first indoor in-vitro experimental technique using real explosives to study the impact of real explosives on dissociated neurons. This is the most accurate experimental method existing to analyze and characterize primary explosive blast-induced neuronal/tissue injury. Known control factors from the simplified experimental setup such as charge size, distances to target, water temperature, and aquarium volume ensure reproducible data.

5.2 Effects of Primary Blast Pressure Waves Generated by Detonation of Small Explosive Spherical Charges on Neurons

5.2.1 Introduction

In this final report, we discuss the effect of single and multiple explosions of RDX on PC12 neurons. PC12 cells derived from the pheochromocytoma of the rat adrenal medulla were used in these experiments. PC12 cells are widely used in in-vitro studies and show sympathetic neuronal cell properties morphologically, physiologically, and biochemically.¹⁸ PC12 neurites have been shown to respond to external stretching forces in a similar manner to axons.¹⁹ In addition, the cells synthesize and release catecholamines and are a well-known neuronal model for in-vitro ischemia.¹⁸ PC12 cells have been used to study oxidative stress, cytoskeletal pathology such as axonal, membrane damage, and ischemia.^{20–24} PC12 cells do not express the normal complement of N-methyl-D-aspartate (NMDA) receptor subunits, which may be a limiting factor for their use as a neuronal model in TBI studies.²⁵ However, we focused on membrane compromise, which is not adversely affected by the lack of NMDA receptors, and thus PC12 cells were a suitable cell line for our experiments.

Previous research has shown a large disparity amongst the peak overpressure values required to generate mild, moderate, and severe TBI, with generated pressures of 3–50 psi for whole animal, 22 psi for the head only, and 1,450 psi for direct brain exposure.^{26–29} For our experiments, we focused on the pressure range ca. 10–25 psi to replicate mild to moderate TBI conditions since this represents the majority of military TBIs (90.6%).³⁰ Certainly, changes in cell viability following a blast event indicate injury. However, more subtle changes such as plasma membrane damage can lead to the influx of unwanted extracellular ions such as calcium and the efflux of cytosolic components, causing delayed cellular damage. In addition, the evaluation of morphological changes such as axonal beading provides another method to observe membrane and cytoskeletal damage and deferred detrimental

effects. Thus, here we have examined viability, cell membrane permeability, and cell morphology changes to gain an understanding of the structural and functional changes due to the insult.

5.2.2 Materials and Methods

5.2.2.1 Materials

Circular glass coverslips (12 mm), mouse laminin, phosphate buffered saline (PBS), Hank's Balanced Salt Solution (HBSS, 21-022-CV), Dulbecco Modified Medium (DMEM), RPMI 1640, calf serum, horse serum, nerve growth factor (NGF 7S), lactate dehydrogenase (LDH) cytotoxicity assay kit, calcein, RIPA buffer and the micro BCA protein assay kit were purchased from Fisher Scientific. Antibiotic/antimycotic (10,000 I.U. penicillin, 10,000 µg/mL streptomycin, and 25 µg/mL amphotericin [per mL]) was obtained from Cellgro. Calcein AM and ethidium homodimer-1 obtained from Life Technologies. Polylysine, protease inhibitor cocktail, and the glutamate assay kit were obtained from Sigma Aldrich.

5.2.2.2 Sample Preparation

Circular glass coverslips (12 mm) were cleaned using piranha etch (70:30 H₂SO₄: H₂O₂) for 30 min and then rinsed thoroughly with deionized (DI) water. Slides were then sonicated (3 × 10 min) in ethanol to sterilize. Sterile coverslips were placed in 24 well plates (Corning, Inc.) and submerged in 100 µg/mL polylysine solution for 30 min. The slides were rinsed 3 times in DI water and allowed to air dry. The slides were then immersed in 10 µg/mL laminin at 4 °C overnight. After protein attachment, the slides were rinsed 3 times with PBS and used immediately for cell culture.

5.2.2.3 Culture of PC12 Cells

PC12 cells derived from the pheochromocytoma of the rat adrenal medulla were used in these experiments. PC12 cells are widely used in in-vitro studies and undergo neuron-like differentiation when treated with nerve growth factor. Therefore, they are a useful cell line to probe the effect blast on neuron morphology and viability.^{31–33}

PC12 cells were cultured in RPMI 1640 medium supplemented with 10% heat-inactivated horse serum and 5% fetal bovine serum and 1% antibiotic/antimycotic “complete medium” at 37 °C and 5% CO₂. Cells were seeded at a density of 5,000 cells per well on the 12-mm coverslips in the 24 well plates in high-glucose DMEM with 1% horse serum, 0.5% calf serum and 1% antibiotic/antimycotic “differentiation medium”. After 24 h, 100 ng/mL NGF was added to the

differentiation medium. Cells were subjected to blast 5 days after adding NGF. Control samples, which remained in the incubator for the duration of the experiment, and sham samples, which experienced everything the injured samples did except the blast exposure, were also included. Sham cells were not placed into the aquarium due to time constraints. LDH and viability assays showed no significant difference between sham samples held in the oven and those put in the aquarium for a 20-min time period (typical length of a triple blast experiment).

5.2.2.4 Blast-Induced Injury of Cells

Just prior to the blast experiment in a sterile hood, the plastic well plate lid was removed, HEPES buffer (10 mM) was added, and the well plates were sealed with sterile SealPlat covers from Excel Scientific and then placed in a plastic bag to maintain sterility of the cultures. The samples were transported to the blast site and held in an oven at 37 °C until ready to be used in the experiments. The samples were submerged horizontally on a stage in a 10-gal PMMA aquarium containing water heated to 37 °C, as displayed in Fig. 3c. The neuronal cell line (PC12) culture well plates were mounted, secured, and immersed horizontally in the middle of the aquarium, with the cells in the first row facing the shock front. All blast experiments were performed without the well plate lid. The charge standoff distance to the neuron cell chamber was measured as a clear spacing between the charge and the outer wall of the aquarium (Fig. 4), and was adjusted to generate ca. 10–25 psi pressures inside the cell culture wells. Multiple blasts were separated by 5- to 7-min intervals during which the samples were not removed from the tank. The interval was chosen based on the limitations of our system and does not necessarily reflect the actual time between blasts on the battlefield. Because the blast was at a site without an incubator, we needed to keep the experiments as short as possible. The interval chosen was the minimum amount of time needed to clear the blast chamber for reentry and set up the next explosive.

5.2.2.5 Cell Morphology and Viability

Five days after seeding cells in differentiation medium supplemented with 100 ng/mL NGF, the cells were subjected to single or multiple blast insults. The viability was assessed at 2 h (single blast only) and 24 h postblast by staining the cells with calcein AM and ethidium homodimer-1, following the protocol outlined by Life Technologies. Briefly, the medium was removed and the cells were rinsed with PBS 3 times. The cells were then incubated in a PBS solution containing 2 μ M calcein AM and 4 μ M ethidium homodimer-1 for 30 min at 37 °C. Samples were imaged using confocal laser scanning microscopy (CLSM) on a Zeiss LSM5 Pascal equipped with Epiplan-Neofluar lenses. The cells were imaged in the multitrack mode with a 543-nm laser, which was used for the fluorescence imaging. A

Approved for public release; distribution is unlimited.

minimum of $n = 5$ random areas for each of a minimum of 3 replicate samples were imaged using the 10 \times and 20 \times objectives. CLSM samples were processed using image area analysis tools in Image J v 1.34, National Institutes of Health. Briefly, images were converted to binary and thresholds were set for each channel. The percent area was calculated using the Analyze Particles tool. The smaller cell size for the dead cells compared to live cells was corrected by multiplying the percentage of area of dead cells by the average live cell size divided by average dead cell size. Neurite morphology was also accessed via the calcein AM stain. The length and bead diameter were measured using the Zeiss LSM software (v 4.2.0.121).

5.2.2.6 Membrane Permeability Assays

The lactate dehydrogenase (LDH) assay was performed according to the manufacturer's instructions. Media was sampled from the extracellular bath 24 h postblast. All values were normalized to the total protein determined from a micro BCA protein assay. Briefly, the media was removed, the sample was rinsed with PBS, and the coverslips were allowed to dry for a few minutes. Then approximately 20 μ L of RIPA buffer with 1% (vol) protease inhibitor was added to each coverslip. The cells were scraped immediately and the lysate was analyzed using the micro BCA protocol or put on ice for 30 min and then stored at -80°C until analysis.

Calcein uptake was probed by rinsing the samples with HBSS and then incubating in 0.3 mM calcein in HBSS for 10 min. The samples were then rinsed thoroughly with HBSS and imaged using the 488-nm laser on the CLSM system as described previously. Imaging gains and offsets were fixed to allow semiquantitative comparison between samples. Phase-contrast images were also collected to ensure cells were in focus. Fluorescence intensities were measured by selecting individual cells using the region of interest feature and calculating the mean intensity using the histogram feature using the software.

5.2.2.7 Statistics

All data are expressed as mean \pm standard deviation unless noted. Unpaired Student's *t*-tests were conducted with a significance level of $p < 0.05$. All experiments were performed with a minimum of 3 replicate samples.

5.2.3 Results

Changes in membrane permeability, whether permanent leading to cell death or transient leading to increased ion transport, are thought to be a major contributor to cellular injury following blast exposure.³⁴ Such changes were probed using an LDH. Membrane permeability changes were accessed at 24 h postblast and

normalized to the total protein. The results for the single and triple blast peak pressure in water of ca. 25 psi are displayed in Fig. 12. The extracellular LDH concentration of the injured samples was similar to the shams and controls for the single blast but significantly higher for the triple blast. Membrane permeability was also evaluated using calcein dye. Calcein is normally a membrane-impermeable dye, but upon damage to the plasma membrane, leakage of the dye can occur into the cytosol causing an increase in the fluorescence of the cell. Figure 13 displays the average fluorescence intensities for cells subjected to single and triple blast insults of ca. 25 psi. The fluorescence intensities were significantly higher for the injured cells compared to the control and sham. However, the difference in dye uptake between the single and multiple blasted samples was not significant.

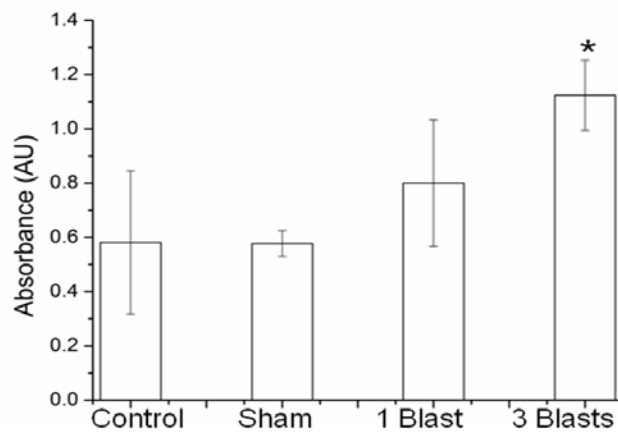


Fig. 12 Membrane permeability changes as a function of LDH release of PC12 neurons exposed to explosive blast (ca. 25 psi). Control cells remained in the incubator during the entire experiment, sham cells were transported to blast site but were not injured. * $p < 0.05$ compared to 1 blast, sham, and control, $n = 3$

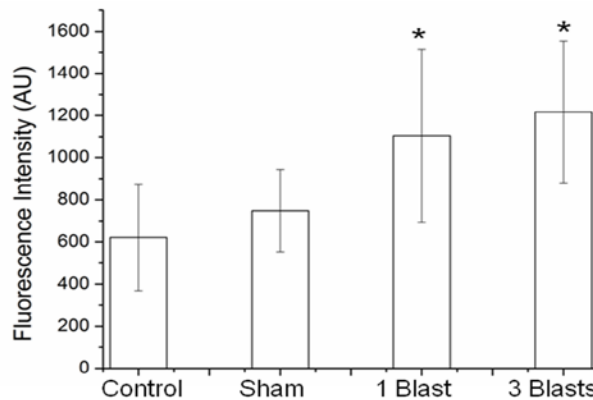


Fig. 13 Membrane permeability changes as a function of calcein dye uptake of PC12 neurons exposed to explosive blast (ca. 25 psi). Control cells remained in the incubator during the entire experiment, sham cells were transported to blast site but were not injured. * $p < 0.05$ compared to sham and control, $n = 3$

The viability of cells subjected to blast was evaluated using a live/dead assay to probe the percentage of cells that did not recover postinjury. Figure 14I displays representative images of the cells taken 24 h after the blast exposure. The cell viability remained very high after the single ca. 10-psi blast exposure. No dead cells are observed in the control sample shown, and only a few dead cells are present for the sham and injured sample. The viability was assessed numerically from live/dead images taken 2 and 24 h after injury for cells subjected to a single blast (Fig. 14II). The percentage of viable cells was nearly identical at 24 h postblast for controls, shams, and injured samples. The viability (percentage) of the injured sample after 2 h was significantly lower than the control (97.9 ± 1.4 [$n = 10$] vs. 99.3 ± 0.8 [$n = 6$]), but similar to the sham (98.5 ± 1.4 [$n = 6$])). Thus, the reduced viability may be attributed to injury from transportation to and from the blast chamber, rather than the blast itself.

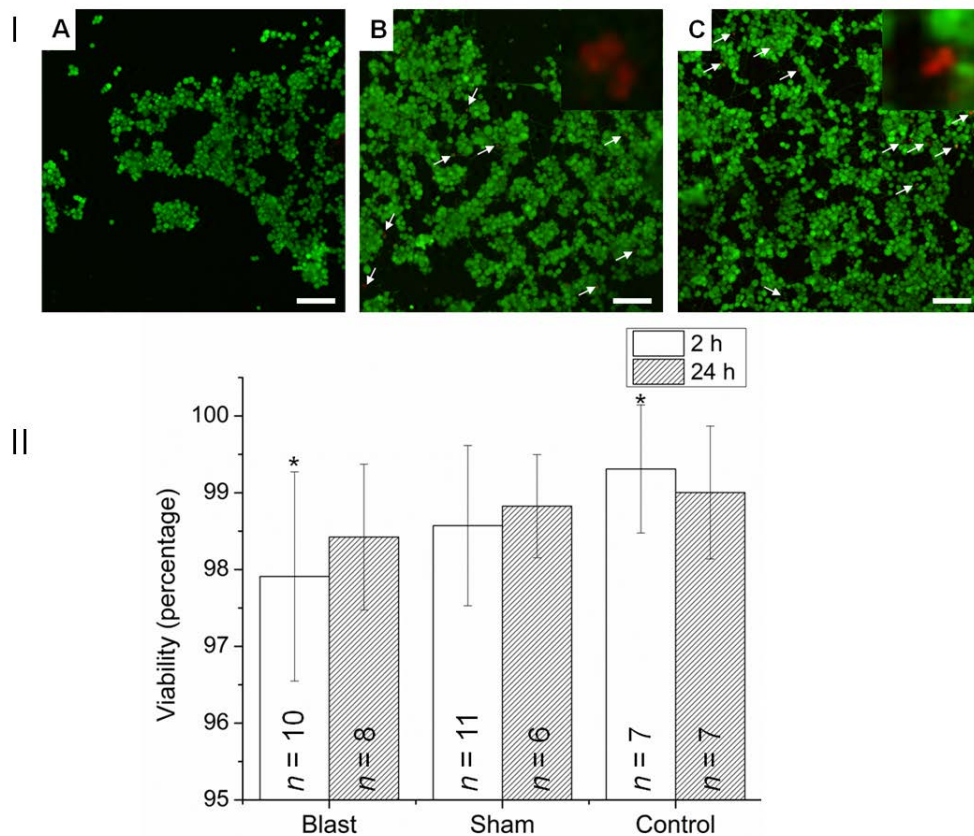


Fig. 14 Viability of PC12 neurons after exposure to explosive blast (ca. 10 psi). Control cells remained in the incubator during the entire experiment, sham cells were transported to blast site but were not injured. I) Viability of PC12 cells 24 h after blast injury as determined by a live/dead assay: A) Control, B) sham cells, and C) injured cells subjected to a single blast. Live cells appear green due to calcein AM dye trapped inside. The nuclei of dead cells appear red due to ethidium homodimer-1 staining. Arrows denote selected dead cells. Scale bars represent 100 μ m. Inset displays magnified image of dead cells. Inset scale bar represents 50 μ m. II) Viability of PC12 cells 2 and 24 h after blast injury calculated from live/dead assay. * $p < 0.05$

The viability of neurons was also evaluated for samples exposed to multiple blasts (Fig. 15). As discussed previously, the cell death after a single blast at ca. 10 psi was not significant. However, the cell death after 2 and 3 repeated blasts was elevated compared to the cells exposed to a single blast (except for 3 blasts row 2). For the multiple blast experiments, 3 different peak pressures were evaluated by placing the cells in different rows in the well plate. The first row experienced the highest pressures (ca. 24 psi), with each subsequent row receiving reduced pressures (ca. 14 psi and 9 psi, row 2 and 3 respectively). Although the pressure in row 1 was more than double that of row 3, there was no significant increase in cell death between rows. In addition, cell death did not significantly change between cells exposed to 2 blasts and those exposed to 3 blasts. Figure 15I displays images of the cells after 1, 2, and 3 blast exposures from row 1. Live cells are present in the green channel, and dead cells are in the red channel. Dead cells are smaller in size since only nucleus is stained. A greater percentage of dead cells (red stained nuclei) were observed for the samples exposed to 2 and 3 blasts.

In addition to the chemical, membrane permeability, and viability changes caused by blast exposure, neurite morphological changes were also investigated. Figures 16 and 17 show images of the neuron morphology of control, sham, and injured cells following single and multiple blast exposures of ca. 10 psi. There is evidence of a couple of axonal beads in the control and sham cells but significantly more beading is present in the injured cells. A schematic of axonal beading due to blast injury is demonstrated in Fig. 18. To quantify the beading, the number of beads per micrometer of neurite length, number of beads per neurite, and the bead diameter were calculated from analyzing a minimum of 5 CSLM images and ca. 300 neurites.

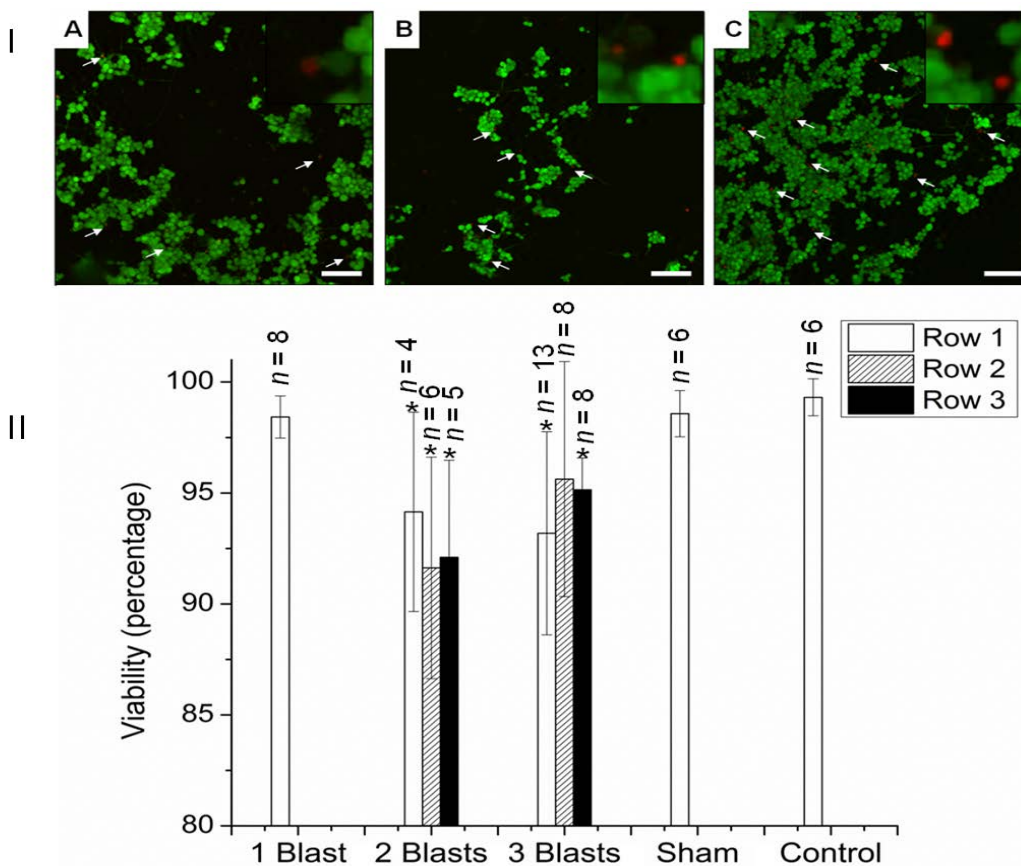


Fig. 15 Viability of PC12 neurons after exposure to single and multiple explosive blasts. Samples denoted 1 Blast were exposed to 19 psi. Samples denoted 2 Blasts and 3 Blasts were exposed to ca. 24, 14, and 9 psi (row 1, row 2, row 3). Multiple blasts were separated by 5–7 min intervals. Control cells remained in the incubator during the entire experiment, sham cells were transported to blast site but were not injured. **I)** Viability of PC12 cells 24 h after exposure to single and multiple explosive blasts as determined by a live/dead assay: **A)** injured cells exposed to single blast of ca. 9 psi, **B)** injured cells exposed to 2 blasts of ca. 9 psi separated by ca. 5 min, and **C)** injured cells exposed to 3 blasts of ca. 9 psi separated by ca. 5 min. Live cells appear green due to calcein AM dye trapped inside. The nuclei of dead cells appear red due to ethidium homodimer-1 staining. Arrows denote selected dead cells. Scale bars represent 100 μ m. Inset displays magnified image of dead cells. Inset scale bar represents 50 μ m. **II)** Viability of PC12 cells 24 h after blast injury calculated from live/dead assay. * $p < 0.05$ compared to control, sham and 1 Blast.

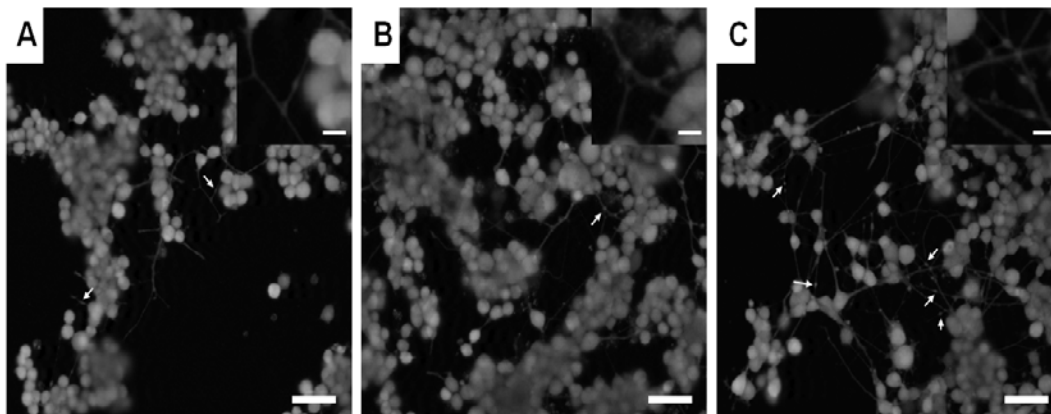


Fig. 16 Morphology of PC12 cells 24 h after exposure to a single explosive blast of ca. 10 psi. A) Control cells that remained in the incubator during the experiment, B) sham cells that were transported to blast site but were not injured, and C) injured cells subjected to a single blast. Arrows denote locations of selected axonal beads. Scale bars represent 50 μm . Inset displays magnified image of beads. Inset scale bars represent 10 μm .

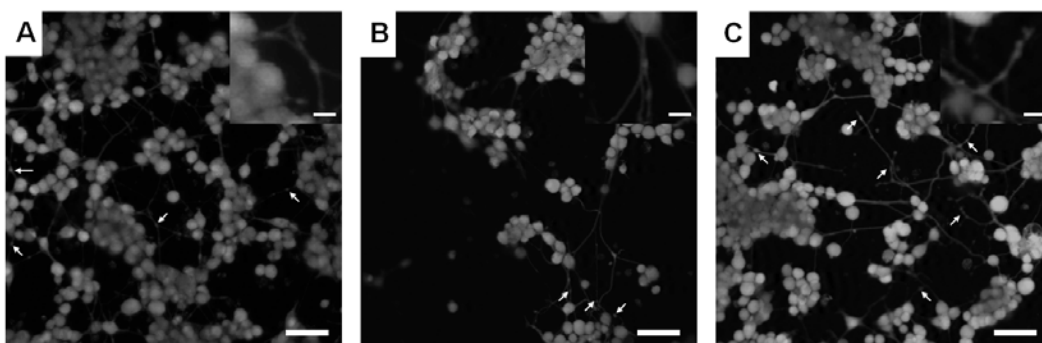


Fig. 17 Morphology of PC12 cells 24 h after exposure to a single and multiple explosive blasts of ca. 10 psi. A) Injured cells subjected to a single blast, B) injured cells subjected to 2 blasts separated by ca. 5 min, C) injured cells subjected to 3 blasts separated by ca. 5 min. Arrows denote locations of selected axonal beads. Scale bars represent 50 μm . Inset displays magnified image of beads. Inset scale bars represent 10 μm .

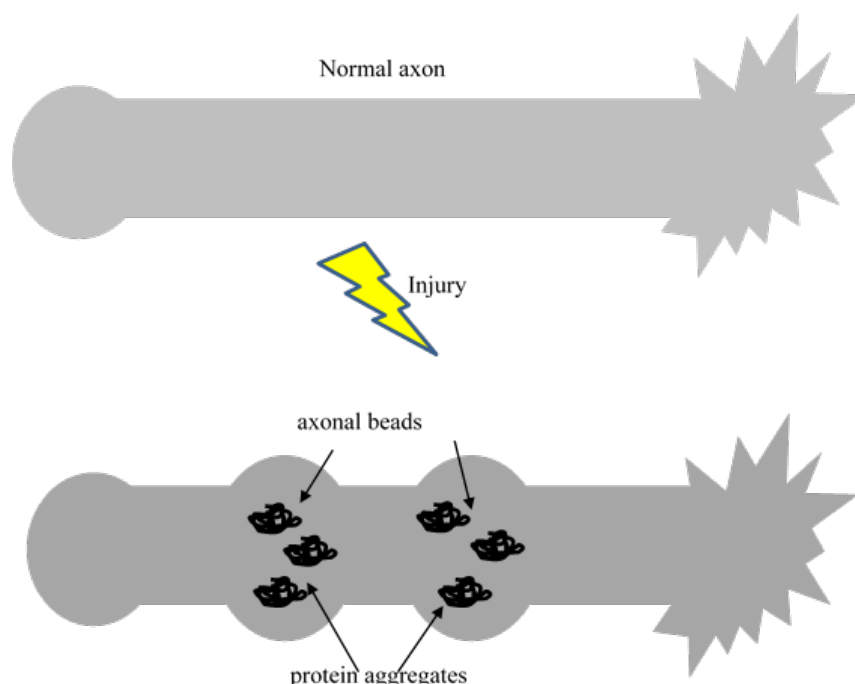


Fig. 18 Schematic showing axonal beading that can occur after blast injury

Results are displayed in Table 3. The bead diameter remained consistent for controls, shams, and injured cells, ranging from $3.55 \pm 0.70 \mu\text{m}$ to $5.04 \pm 0.99 \mu\text{m}$. In addition, there was no change in the number of beads per neurite length or beads per neurite between the control and sham samples, indicating that the mechanical stress of transport to the blast site did not increase axonal beading. Injured samples had a significant increase in beading compared to control and sham samples in both the number of beads per micrometer and beads per neurite, but there was no significant difference in beading between the cells exposed to single and multiple blasts.

Table 3 Quantification of axonal beading observed in PC12 neurons 24 h after exposure to explosive blast

Test parameter	<i>n</i>	Beads per micrometer	Beads per neurite	Bead diameter (μm)
Control	8	0.0050 ± 0.004	0.18 ± 0.2	4.17 ± 1.2
Sham	6	0.0039 ± 0.002	0.19 ± 0.1	4.13 ± 0.72
1 Blast	7	0.010 ± 0.006^a	0.48 ± 0.3^a	4.52 ± 1.2
2 Blasts	4	0.012 ± 0.004^a	0.52 ± 0.2^a	5.04 ± 0.99
3 Blasts	10	0.0095 ± 0.005^a	0.41 ± 0.2^a	3.55 ± 0.70

^a $p < 0.05$ compared to control and sham. *n* = number of separate CLSM images examined. 1 Blast = cells were exposed to a single blast of ca. 10 psi. 2 Blasts = cells were exposed to 2 blasts of ca. 15 psi (average) separated by ca. 5 min. 3 Blasts = cells were exposed to 3 blasts of ca. 15 psi (average) separated by ca. 5 min.

5.2.4 Discussion

In this work, we examined changes in membrane permeability to understand potential mechanisms of cellular injury. Transient pore openings or mechanoporation are thought to be a major contributing factor to injuries sustained from a TBI. The increase in permeability allows for increased ionic transport, particularly the influx of sodium, which in turn modulates a substantial rise in intracellular calcium.⁹ The former activates a variety of intracellular pathways including calpains, which can degrade cytoskeletal proteins like tubulin.³⁵ In addition, the increase in intracellular sodium can cause osmotic swelling and additional cytoskeletal damage including axonal beading and focal adhesion complex disruptions.³⁶ LDH release is one way to examine the extent of membrane damage, and extracellular LDH can be quantified by an enzyme coupled reaction and colorimetric assay. We tested LDH levels at 24 h following the blast events. Compared to control and sham samples, no significant change in LDH concentration was observed for the single blast sample. However, the sample blasted 3 times showed higher levels of LDH release. Additional evidence of membrane opening and increased ionic flux can be inferred from cell death, a more extreme case, or changes in axonal morphology. The viability data also showed increased cell death for the samples that experienced repeated blast compared to the sampled blasted one time. Calcein uptake was also evaluated to probe membrane damage. Increased dye uptake was observed for the injured samples, but there was not a statistical difference between the single and triple blasted samples. This result was unexpected based on the work by La Placa et al. in which they observed increased calcein uptake on primary cortical neurons for increased strain rates/higher loading immediately after the event.³³ In our experiment, we did not induce higher loading, but instead repeated loading. In addition, our measurements were taken 24 h after the event rather than immediately. Arun et al. actually saw a neuroprotective effect from repeated blast loading on SH-SY5Y cells, which may suggest the membrane damage was not increased with additional loading events or at least the damage was not sustained.¹¹

Cell viability was evaluated at 2 h (single blast only) and 24 h after the blast. No significant difference was observed between the single blast sample and the sham control, which was expected due to the low pressure of the blast wave used (ca. 10 psi). However, there was no significant difference in cell death between rows (ca. 9–24 psi). Effgen et al. found that for rat organotypic hippocampal slice cultures, cell death from primary blast was minimal up to pressures of 21–27 psi.³⁶ Repeated blast below the threshold pressure did not significantly increase cell death. Ravin et al. found little cell death in human brain cells at pressures as high

as 220 psi in the absence of shear.³⁷ Generally those models involve a secondary or higher-order injury mechanism such as acceleration, which may be the primary mechanism of injury at lower pressures. Although we expected some shear due to movement of the coverslip in the well plate, the pressures we examined were below those determined by Effgen et al. to cause significant cell death. In our experiments, we observed a significant increase in cell death between the cells exposed to single and multiple blasts, although cell death was still relatively minimal. This could be attributed due to the repeated mechanical damage to the membranes and increased ion transport. Intuitively, more blast should mean more injury, but in our research there was no significant difference in cell death between 2 and 3 blasts. Arun et al. saw an increase in viability after 24 h for multiple blasts that was attributed to increased neurobiological protective effects, so further investigation is warranted.¹¹ Possibly some type of neuroprotective effect is occurring after the second blast to prevent further injury. Particularly in the case of mild to moderate loadings, such as those used in our studies, there may be a need to use other assays to probe for more subtle changes in cellular function. Real-time calcium imaging and electrophysiology time course studies would be useful to better characterize the damage mechanisms for both single and repeated blast exposure.

Axonal beading (see Fig. 18), a hallmark of the axonal response to mechanical damage, was probed for cells exposed to blast. Due to the viscoelastic nature of the cell membrane, the axons can undergo sudden shape changes in response to applied mechanical force. Coupled with membrane damage, increased ionic flux and subsequent swelling can lead to bead formation along the axon length, focal swellings, or even disruption of the focal adhesion complex and detachment from the substrate.¹⁹ The injured cells had significantly higher axonal beading compared to controls, but there was no significant difference between the cells exposed to single and repeated blast. Monnerie et al. found that beading was maximized for a stretch injury immediately after the insult for rat cortical neurons.³⁵ After 5 h, only 5–10% of the processes displayed beading, and after 15 h, beading was nearly absent. Thus, time points earlier than 24 h are needed to fully understand the extent of neurite mechanical deformation. In addition, the bead diameter ranged from $3.55 \pm 0.70 \mu\text{m}$ to $5.04 \pm 0.99 \mu\text{m}$, whereas others have reported submicron beads. Limitations of our current microscope did not allow resolution of features of this size, thus it remains possible that neurites subjected to repeated blast could have additional smaller beads or axonal swelling that were not detected.

5.3 Quantum Dot (QD) Targeting to Specific Neural Cells

5.3.1 Introduction

The use of luminescent semiconductor nanocrystals (QDs) with targeting groups for analyte sensing was explored. By creating sensitive, fluorescent-sensing units that can be selectively targeted to specific cells, it should be possible to detect and quantitate the changes in levels of key analytes associated with brain injury (such as calcium ion and glutamate) in real time. This would help track the biochemical changes that happen to brain tissue in the time course of the injury.

QDs were chosen over traditional fluorescent dyes (such as fluorescein) and larger protein dyes (such as green fluorescent protein). They have a number of key advantages, including size and composition-tunable emission from visible to infrared wavelength; high levels of brightness and photostability for long-duration experiments; and surface-modified QDs for fluorescent tagging are now commercially available. Their chemical uniformity makes attachment of further functionality relatively easy compared to the protein dyes.

At ARL, a bioconjugation method for attaching the dimeric lectin protein succinyl-Concanavalin A (succinyl Con A) to PEGylated QDs via the Disuccinimidyl suberate (DSS linker) was developed. Succinyl Con A is known to tightly bind to certain cell surface carbohydrates, included those found on the surface of some neurons (the protein is also well studied and low in cost). The structures of succinyl Con A and DSS are outlined in Fig. 19.

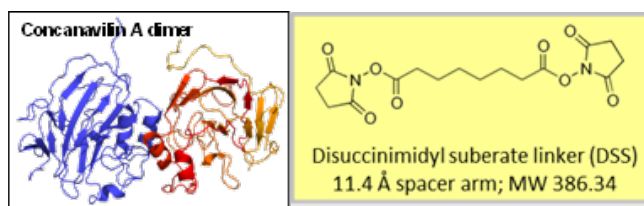


Fig. 19 Structures of Concanavalin A dimer and Disuccinimidyl suberate

The reaction scheme to synthesize the QD – lectin conjugate is shown in Fig. 20. The procedure was adapted from a suggested protocol for conjugation of PEGylated QDs with streptavidin.³⁸

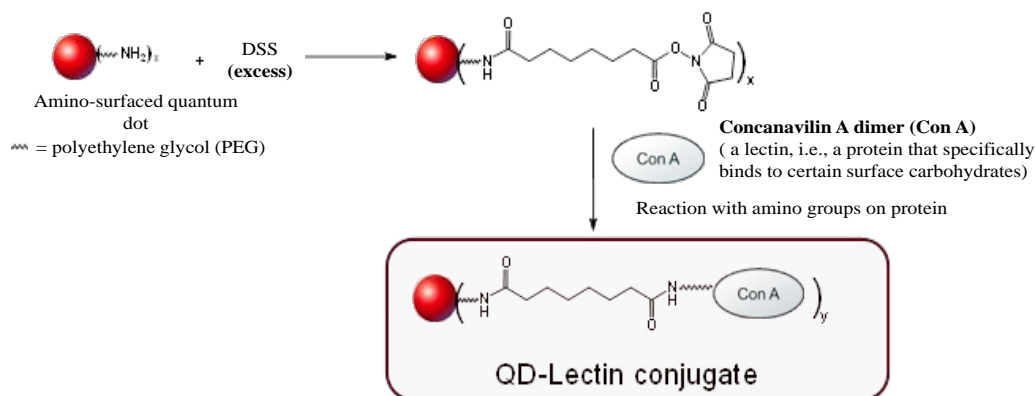


Fig. 20 Reaction scheme for producing the QD-lectin conjugate

5.3.2 Experimental

The QD starting material (Qdot 655 ITK Amino PEG Quantum Dot; emission at 655 nm) was obtained from Invitrogen as a suspension (2 nmol in QD) in borate buffer (50 mM borate, pH 8.3). The QD suspension (250 μ L) was loaded into a Centricon centrifugal ultrafiltration unit (YM-100; 100 kD MWCO; Millipore Corp). The suspension was diluted up to 2 mL with PBS buffer (pH 7.4), gently vortexed and sonicated, then centrifuged for 30 min (1,000 G, 15 $^{\circ}$ C). The clear, colorless filtrate was discarded and the unit was filled up to the 2 mL mark with PBS again, vortexed/sonicated, and centrifuged as before. The filtrate was again discarded and the QD rinsing procedure was repeated in the Centricon unit one more time. The suspension was then diluted up to 250 μ L with PBS, gently vortexed and sonicated, then transferred to a siliconized microfuge tube.

A 100 mM solution of DSS in dimethyl sulfoxide (DMSO) was prepared by adding 2 mg of DSS to 54 μ L of anhydrous DMSO in a siliconized microfuge tube. An aliquot (2.5 μ L) of the DSS solution was added to the QD suspension in PBS (this creates a final ratio of 8 μ M dots to 1 mM DSS in the solution), the mixture was gently vortexed, then allowed to react for 30 min at room temperature with gentle agitation with an orbital shaker.

A desalting column (Bio-Rad Econo-Pac 10DG, with 10 mL of Bio-Gel P-6DG; exclusion limit 6 kD) was prepared by equilibration with 5 column volumes of PBS (pH 7.4). Excess DSS was removed by passing the reaction mixture down the column, collecting the colored band (as visualized by a UV lamp at 366 nm) into a small glass vial containing 4.8 mg of succinyl Con A (Sigma-Aldrich L3885) in 480 μ L of DI water (an approximately 40-fold excess of protein). The vial was

gently vortexed and the succinyl Con A was allowed to react with the DSS-functionalized QDs for 2 h at room temperature with gentle agitation on an orbital shaker. The reaction was quenched by adding 1 M glycine solution to produce a reaction mixture with a final concentration of 50 mM glycine, then letting the quencher react for 15 min at room temperature with gentle agitation.

The reaction mixture was then loaded into a Centricon centrifugal ultrafiltration unit (YM-100; 100 kD MWCO; Millipore Corp). The solution was ultrafiltered to remove excess protein and small molecules, in a similar manner as the Centricon procedure previously, except borate buffer (50 mM, pH 8.3) was used instead of PBS and the mixture was kept at 4 °C. Six rinsings of the protein/QD conjugate were carried out with the Centricon. The conjugate solution (0.5 mL in borate buffer) was filtered through a 0.2 µm syringe filter (HT Tuffryn membrane) and stored in the dark at 4 °C. The conjugates were sent to Prof. DeCoster and his group (LA Tech) for biological testing.

5.3.3 Results

The conjugates were incubated with mixed neuronal cultures (neurons, astrocytes, and microglia). Preliminary experiments showed that the succinyl Con A functionalization led to a great improvement for QD uptake versus QDs in microglia, while little uptake in neurons and astrocytes was observed (Fig. 21). This demonstrated that the conjugates could selectively interact with specific primary cell types.

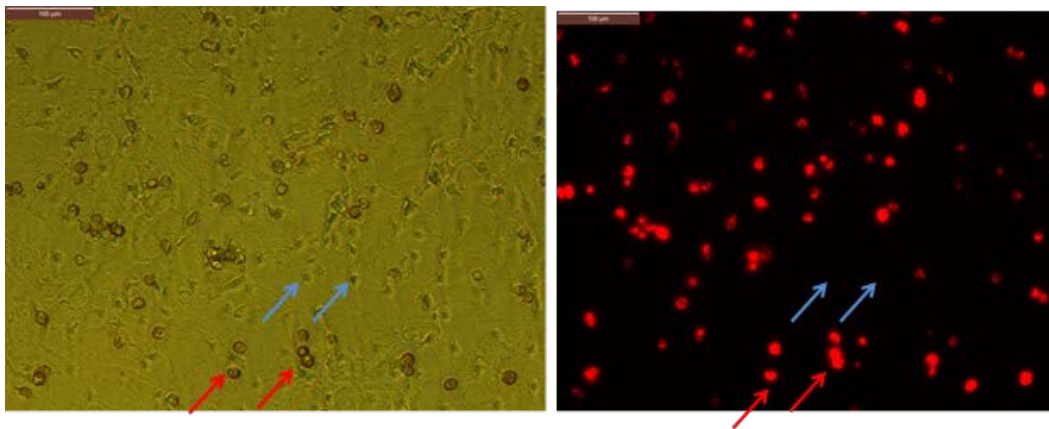


Fig. 21 QD-Con A conjugate uptake in mixed neuronal cultures. Red arrows: microglia with QDs; blue arrows: neurons (no QD uptake observed).

Images of microglia alone showed that the conjugates are actively taken up internally, but excluded by the nucleus (Fig. 22). Nuclear exclusion is always seen, in this case even after fixation.

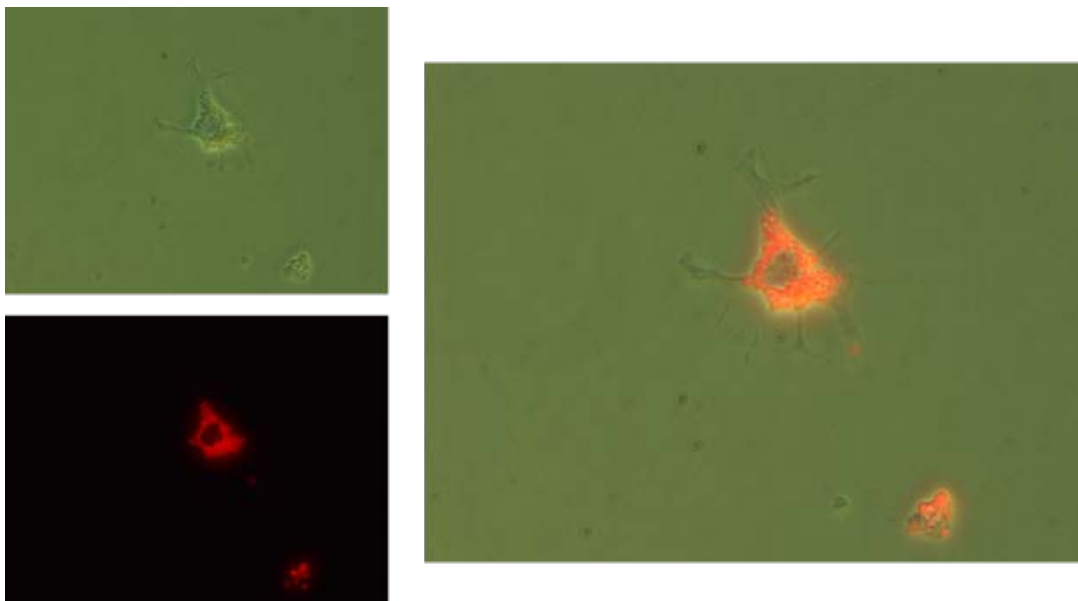


Fig. 22 Microscopy of microglia QD accumulation at higher magnification (630×)

5.3.4 Preliminary Conclusions

Modern research suggests that microglia have an important role in brain injury, including TBI. Therefore, studying the interactions of microglia in mixed cell cultures may yield valuable information. This work indicates that QD-based sensors may be preferentially taken up by microglia (and can be observed even after fixation). There is no indication yet that neurons or astrocytes take them up to any large degree, but it will likely be necessary to test them with a panel of a variety of neural cell types, as the Con A conjugate binding can be highly cell-type dependent.

Generally, functionalization of QDs with lectins (Con A) led to excellent uptake and could allow better targeting of QDs. As a possible future study, calcium imaging can be combined with QDs and fluorescent beads to develop in-vitro models, which allow microglia to be tracked under various conditions (excitatory, excitotoxic, and/or inflammatory responses) while also tracking the activity of neurons. This type of model can provide feedback about systems of cells, in particular how the different cells of the brain interact in normal brain and after TBI.

(Prof DeCoster's work on this project will extend to the end of FY16 due to a funding delay, so more results from his testing will be forthcoming.)

5.4 Computational Investigation of Blast-Wave Impact on Dissociated Neurons Placed in an Aquarium

5.4.1 Introduction

The present work attempts to improve the understanding of the major phenomena and processes associated with the interaction of a realistic blast wave generated from RDX with dissociated PC12 neurons. This research is a bottom-up approach aimed at unraveling the response behavior of neurons to blast waves through computational modeling and simulation. In recent years, most researchers have adopted a top-down approach to examining neuron response to blast starting from shock waves propagating through the human skull with subsequent generation of shock waves through intracranial soft tissue. These approaches while valid pose additional complexities as the intracranial shock waves gets reflected multiple times within various regions of the brain without determining any definitive isolating effects on neurons. In this work, computational modeling and simulations are coupled with in-vitro experiments to isolate pressure-loading impact on dissociated PC12 neurons placed in 24-well plates embedded in an aquarium. The complexities involved in this work are inherent in the explosive detonation as well as the direct interaction of blast waves with the neuron cells. The explosive detonation is a very complex phenomenon where the shape of the explosive, its chemistry, and its mode of detonation strongly influence the explosive waveform, the intensity of the resulting blast wave and its associated pressure, density, velocity, and temperature. Additionally, the direct interaction of the pressure waves with the neurons cells in the 24-well plates leads to their reflection. The results of the impact pressure waves on the neuron cells are presented and analyzed in the following subsections with the implication for damaged cells correlated through the pressure loading versus cell membrane porosity.

5.4.2 Computational Methods and Procedures

The interactions between blast waves propagating from an RDX explosive and dissociated PC12 neurons in a 24-well plate embedded in an aquarium was analyzed in the following way. An Eulerian domain containing both the RDX explosive and PC12 neurons assembly was initially set to atmospheric pressure levels. A point detonation in the center of the 1.7 g of RDX charge was applied to set off the initiation followed by detonation and propagation of blast wave toward the PC12 neuron assembly. Standoff distances ranging from 225 to 350 mm were investigated. Additionally, calculations were carried out with the Eulerian shock physics code CTH to determine pressure histories in areas not accessible with experimental diagnostics. For example, tracer particles were strategically placed in

sample wells to determine pressure histories resulting from the RDX blast waves. Because of the symmetry of the shock wave, only 3 tracer particles were used for each row of 6 wells. To solve the complete nonlinear dynamic problem requires the knowledge of equation of state (EOS), strength model, and failure model. The Jones-Wilkens-Lee (JWL) EOS was used to represent the RDX explosive with tabular SESAME EOS used for the surrounding air, the water medium in the aquarium, and the 24-well plate. The material properties of the aquarium and the 24-well-plate holder were represented as PMMA where a Mie-Grüneisen EOS was used for the hydrodynamic response and viscoelastic plastic strength model for the constitutive behavior. Finally, in CTH, the adaptive mesh refinement (AMR) capabilities were used to refine the expanding propagating shock front as it moved through the spatial domain. Figure 23 shows the AMR problem geometry setup with the RDX explosive standoff at 300 mm from the sample. As the explosive detonated in air, the AMR refinement techniques were used to resolve the shock front as it moved from air through the aquarium material (PMMA) and into the fluid (water) medium from the explosive in air through the PMMA and eventually to water-filled 24-well plate.

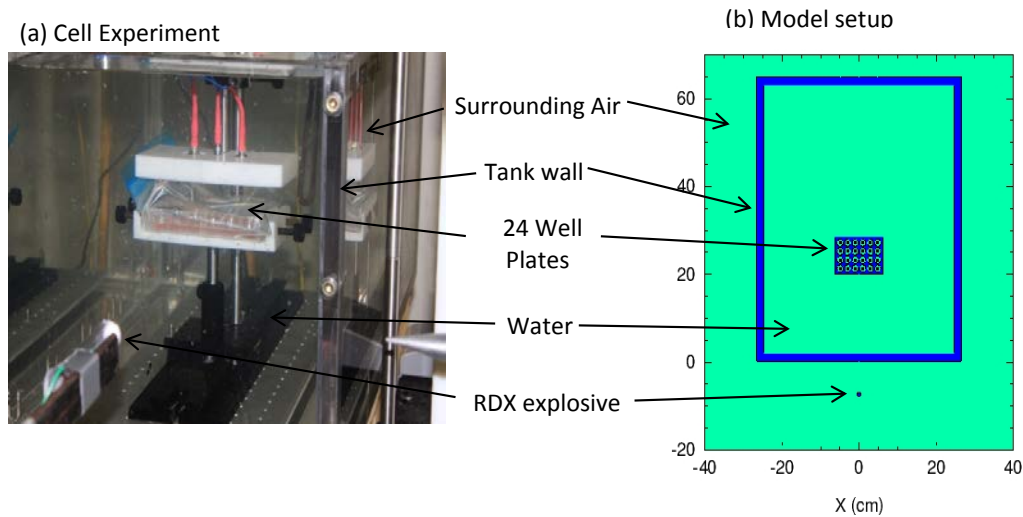


Fig. 23 a) Dissociated neurons in 24-well plate embedded in water-filled aquarium and b) 2-D numerical setup of experiment showing bird's-eye view of 24-well plate immersed in water-medium contained by aquarium walls and surrounded by air with RDX explosive at specified standoff distance

5.4.3 Results

In this section, the main results obtained in the present work are presented and discussed. Figure 24 shows the validation of the calculated results against experiments for the case of temporal evolution of pressure (Fig. 24a) in air as well as (Fig. 24b) in the aquarium. Specifically, Fig. 24a shows the case in which the

pressure histories at 325-mm standoff distance from the initiated RDX explosive were recorded. From experiments, a peak pressure on the order of 100 psi was recorded, followed by a delayed reflected pressure wave slightly above 50 psi. The calculated pressure histories also compared well with the recorded initial peak pressure, with the exception of the reflected pressure.¹ The reflected pressure wave was a result of reflecting pressure wave propagating back to the pressure sensor from the aquarium tank wall. This was not accounted for in the computational model. The propagated pressure waves from the RDX air blast traveled through the PMMA aquarium container and into the fluid water medium. Figure 24b shows the calculated and experimental pressure histories in water at a specified standoff distance of 300 mm. Both the calculated and recorded results show good agreement to within 4% with the initial peak pressure exceeding 125 psi.

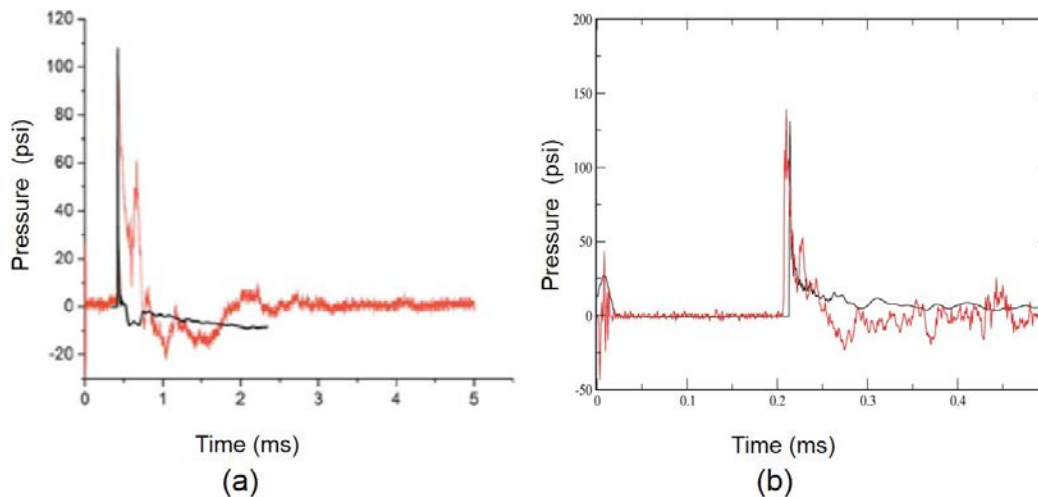


Fig. 24 Model calculations validated with blast experiments showing RDX explosive pressure histories: a) in air at 325-mm explosive standoff and b) in water-filled aquarium at 300-mm standoff

With the validated model completed, the initial impact pressure at the aquarium front was determined for the standoff distance at 125 mm from aquarium front or 325 mm from the immersed neuron sample in the 24-well plate. As an example, Fig. 25 shows the temporal evolution of the pressure just inside the aquarium front. The pressure wave is seen to shock-up³⁹ (i.e., the pressure wave assumes a vertical front where the PMMA material “jumps” in pressure from the nonshocked to the shocked state). The corresponding spatial distribution is also shown in Fig. 26. Here, the blast wave propagates from the RDX explosive through air, through the aquarium front, and into the water medium contained by the aquarium walls. The pressure wave further propagates into the fluid medium reaching the first 2 rows of the 24-well plates. Consequently, by the time the pressure wave reaches the first 2 rows, it has undergone multiple reflections from the water/well plate interfaces.

Figure 27 shows the multiple reflections exhibited in the first 3 cells of the first row. These results range from 25.6 to 35.5 psi. Table 4 shows the complete list of the pressure distribution in all the wells.

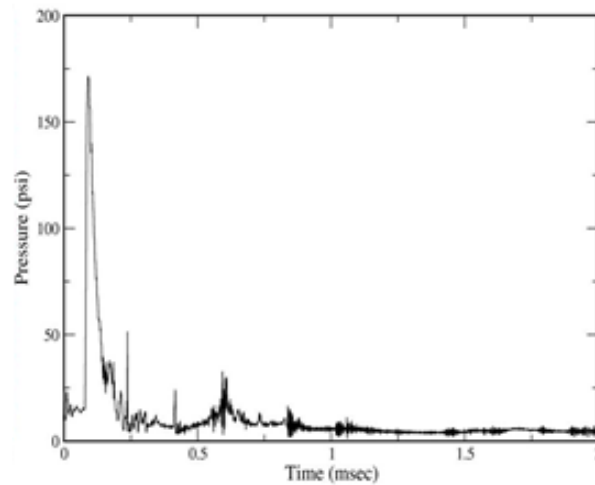


Fig. 25 Shock pressure histories in aquarium (PMMA) material at the front entrance exhibited peak pressure of 173 psi resulting from detonation of RDX explosive positioned at 125-mm standoff distance. The pressure wave transition from air produced increase pressure or a jump condition in the PMMA material from the nonshocked to shocked state. Peak pressure is only maintained for a very short period of time (a few milliseconds) before relaxing approximately to preshock conditions after 0.25 ms.

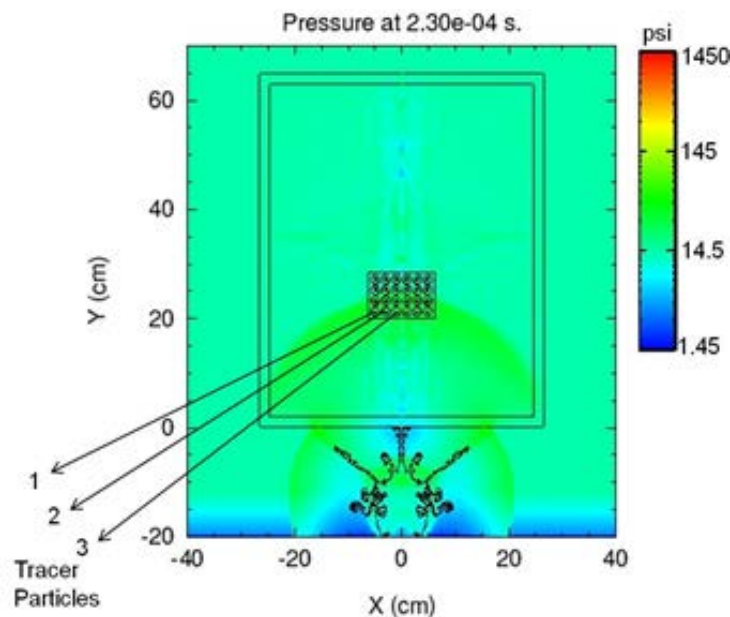


Fig. 26 Evolution of pressure waves from detonated RDX explosive positioned 125 mm in front of aquarium. The pressure waves propagate through the aquarium walls, into the water medium and impact the neurons in the 24-well plates. Tracer particles (such as those shown 1, 2, and 3) are used to captured the strength of the pressures waves in the 24-well pack.

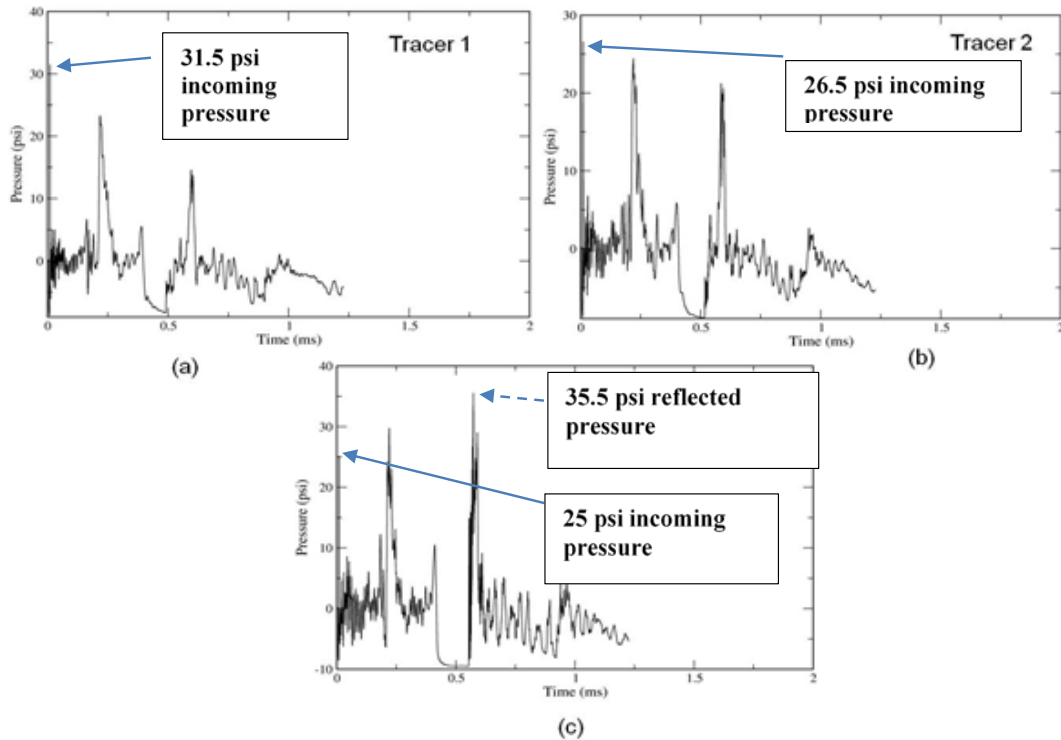


Fig. 27 Calculated pressure histories in the first row of 24-well pack for tracers 1–3 from Fig. 26 for a 325-mm standoff distance from RDX explosive. a) Pressure histories in the well ID at the tracer 1 position experienced a peak pressure of 31.5 psi loading, followed by lower-strength secondary reflected pressure waves. b) Pressure histories in the well ID at tracer 2 position produced peak loading of 26.5 psi, followed by strong secondary reflected pressure waves. c) Pressure histories in well ID at tracer 3 experienced strengthened reflected secondary pressure waves (peak 35.5 psi). Arrows indicate peak pressures entering 24-well plates.

Table 4 Calculated peak pressure distribution in 24-well plate columns (psi)

Rows	Well columns					
	A	B	C	D	E	F
1	31.4559	26.5452	35.4832	35.4832	26.5452	31.4559
2	28.73	26.6134	42.8992	42.8992	26.6134	28.73
3	28.047	26.0672	41.1134	41.1134	26.0672	28.047
4	33	26.0672	25.5462	25.5462	26.0672	33

Since the present work involves blast-loading impact on PC-12 neurons, it was deemed necessary to investigate the influence of varying standoff effect on pressure loading. To match the data collection format from the experiment (no comparison shown), Fig. 28 shows the effect of standoff distance (measured in millimeters) on the pressure loading strength (in psi) across all rows of the 24-well plate. The standoff distances investigated range from 225 to 325 mm. The results reveal that

for increasing standoff, the pressure loading experiences an exponential decay across all rows. The results shown in Fig. 27 indicate that the likelihood of damage to the dissociated neurons will manifest itself in the first row under conditions of reduced standoff distance. Case in point, Fig. 28 shows the peak pressure in the middle cells of each row was recorded across all standoff distance with the highest pressure exhibited in row 1. At a standoff distance of 225 mm, a peak pressure of 450 psi in row 1 has the more likelihood of cell damage compared with 300 psi in row 4 for the same standoff distance.

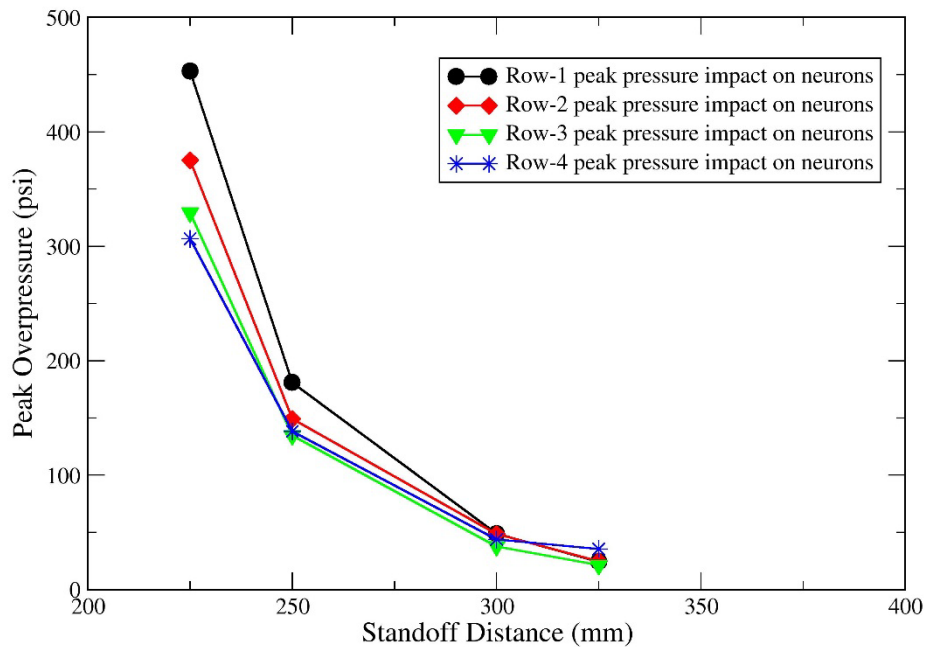


Fig. 28 The effect of standoff distance on calculated peak overpressure in the 24-well pack due to RDX blast impact

To further assess damage to the dissociated neurons, Fig. 29 shows a direct correlation between peak overpressure obtained from calculation and membrane fluorescent intensity obtained from the in-vitro experiment. The membrane fluorescence intensities were measured by selecting individual cells with the region of interest feature and calculating the mean intensity with the histogram feature of the software. Figure 29 shows that fluorescent intensity increases for increasing peak pressure from 50 to 100 psi then stabilizes from 100 to 200 psi. This increase in fluorescent intensity signifies an increase in membrane porosity with the potential for damage.

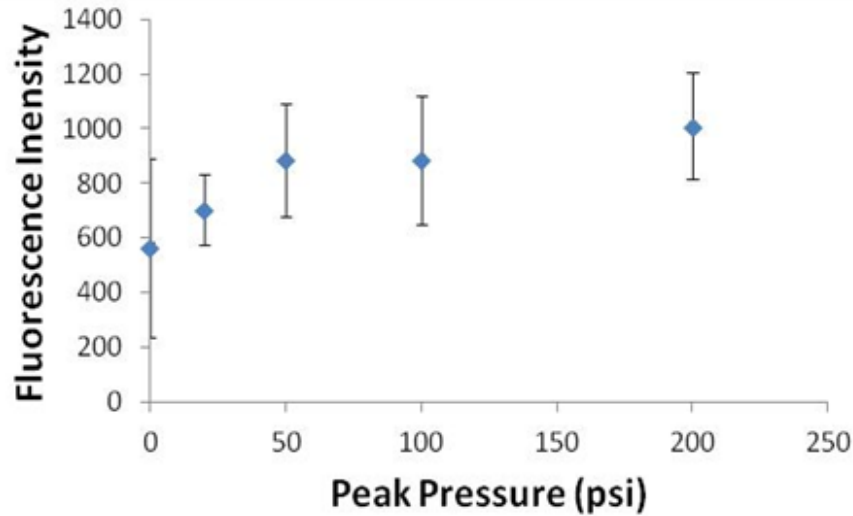


Fig. 29 Fluorescence intensity vs peak pressure in the 24-well pack

Additionally, the damage to PC-12 neurons is also assessed through a complex finite element model of individual neurons (Fig. 30). Figure 30c shows the model developed for single neuron using Mie-Grüneisen EOS with hyperelastic constitutive response. Figure 30c shows the distributed pressure contours loading with concentrated loading highlighted in red and lower pressure loading highlighted in blue. The corresponding pressure loading and von Mises shear stresses are shown respectively in Fig. 31a and 31b. Here, deep undulating pressure is exhibited with tensile and compressive loading (Fig. 31a). Consequently, Fig. 31b also shows increasing shear stress between cytoplasm and nucleus interface with smaller pockets of undulating stress levels compared to the pressure loading.

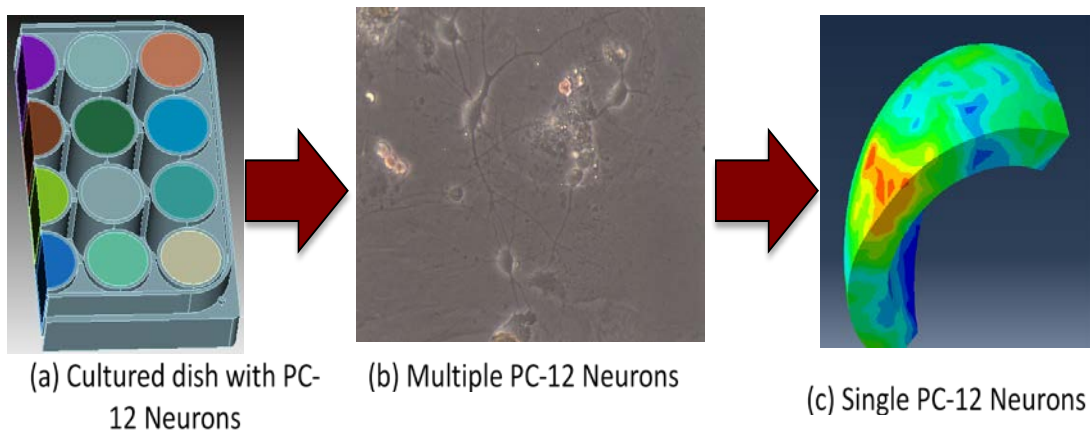


Fig. 30 Impact of pressure loading on a) cultured dish containing PC-12 neurons, b) photograph of multiple PC-12 neurons (40X magnification), and c) finite element model of exhibit mechanical response of single PC-12 neuron

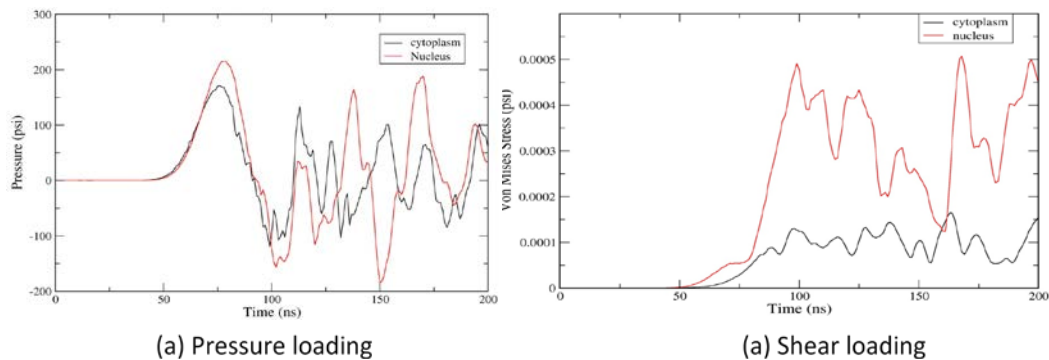


Fig. 31 Mechanical response of PC-12 neurons: a) pressure loading and b) von Mises stress

5.4.4 Discussion

A comprehensive computational investigation of the collision between a blast wave and a 24-well plate filled with PC-12 neuron was carried out. This entailed the construction of fairly detailed geometrical models for the aquarium, the 24-well plates, and individual neuron cell. In addition, detailed material constitutive models had to be identified and parameterized for the 24-well plate and the individual neuron representation. Finally, the work involved accurate modeling of the RDX explosive for blast wave propagation and interactions with the 24-well plate. The results obtained revealed explosive-generated pressure waves within the 24-well plate cavity consisting of compressive stress-dominated waves whose propagation and multiple reflections gave rise to very complex spatial distributions and temporal evolutions of stresses within the 24-well plate.

In the case of identifying damage to the PC-12 neurons (specifically the membrane porosity/damage) an attempt was made to correlate the calculated peak pressures with the associated deformation/damage/leakage identified through fluorescent intensity from in-vitro experiments. Additionally, a single neuron was also modeled to determine the response behavior to pressure and shear loading. The undulating compressive and tensile loading, combined with shear loading, shows the potential for tearing and rupture of the PC-12 cell membrane.

5.5 Damage in Spherical Cellular Membrane Generated by the Shock Waves: Coarse-Grain Molecular Dynamics Simulation of Lipid Vesicle

5.5.1 Introduction

Maintenance of membrane integrity is critical to neuronal/brain function and can be studied at all levels of description (subcellular, cellular, tissue, and network).

While it is well known that exposure of biological cells to shock waves causes damage to the cell membrane, it is still unclear by which mechanisms damage is caused and how it depends on physical parameters such as shock wave velocity, shock-pulse duration, or shock-pulse shape. It has been suggested that shear stress generated at the shock front propagating in a heterogeneous medium can cause damage to nitrocellulose membranes.^{37,40} In general, shock waves propagate without significant energy dissipation in a homogeneous medium or media with similar acoustic impedance (i.e., water and soft tissue).⁴¹ However, the shock strength in nearly incompressible brain tissue varies on a much smaller scale due to cellular acoustic heterogeneity, where the consequent shear—nanoshearing—can be much larger.⁴² Ravin et al.³⁷ found that even when the applied pressure reached 15 atm, there was no damage or excitation in human brain cells unless shear forces, peaking between 0.3 to 0.7 Pa, were present at the cell surface. Additionally, tensile stress may cause membrane damage during the shock wave propagation, since living tissue and brittle materials fail more easily under tension than under compression.³⁷

Experimentally, it is very difficult to observe the dynamics of membrane rupture due to the short time and length scales associated with the event. For instance, although the pressure front of a shock wave travels at supersonic speeds (the speed of sound in water is 1,497 m/s), the shock wave generally interacts with a cell membrane, which is only several nanometers thick, during a time scale on the order of picoseconds. As a consequence, it may prove particularly helpful to elucidate the microscopic structural details and dynamics with computer simulations. Recently, there have been several computational studies on structural changes of lipid bilayers induced by shock waves,^{43,44–47} high-speed stretching,⁴⁸ and ultrasound radiation.⁴⁹ Santo and Berkowitz⁴⁸ observed that a shock wave passing through a lipid bilayer in water-induced nanobubble collapse, where they discerned transient damage to the bilayer and pore creation. After the shock wave passed the bilayer, these pores resealed and the original bilayer was recovered. Even if this poration is transient, a large amount of water was transported across the pore. Koshiyama and Wada⁴⁹ found that a bilayer deforms anisotropically during high-speed stretching, where they observed the formation of a water-filled pore structure penetrating the bilayer develop into a large pore above a critical areal strain, resulting in rupture. In addition for high-stretching speed, they observed that small pores (multipore) could temporarily form.

In this project, shock simulations were performed on a simplified generic model of a cellular membrane using dissipative particle dynamics (DPD), where we determined the damage threshold in the compressive and tensile pressure for a cellular membrane. Structural changes as a result of the shock wave, such as

poration in the lipid layer of the liposome, were also monitored. Although, the accuracy of our results is subject to the limitations of coarse-grained modeling, our results are in qualitative agreement with experiments, which also detected the existence of transient cavitation of lipid membranes.^{50,51}

5.5.2 Models and Methods

Real brain cell membranes are inhomogeneous structures that include multiple lipids, cholesterol, and numerous proteins. The objective of this project is not to simulate cell membranes in full detail, but to use a simplified liposome model to study the mechanism of shock wave-induced damage. Vesicles or liposomes are composed of phospholipids that encapsulate a core region of water inside a hydrophobic membrane. An advantage of modeling vesicles over planar membranes is the absence of a periodicity effect in the former, where curvature can be used as an additional parameter. Using a coarse-grained representation also makes it feasible to simulate larger, spherical membrane systems for longer time than those accessible through an atomistic depiction. This spherical representation is necessary to reproduce qualitatively real damage processes, including membrane defects and curvature, where a less-than-ideal flat surface likely contributes to membrane rupture. The longer simulation time obtainable by these models also makes it possible to study the time evolution of the shocked membranes, where the shock front can travel for a longer period of time.⁴⁶

The DPD approach, which is a mesoscale technique for complex fluids, correctly captures hydrodynamic behavior. A DPD system is composed of coarse-grained soft particles, each representing a cluster of molecules rather than individual atoms, moving continuously in space and discretely in time according to Newton's equations of motion. A detailed description of the DPD thermostat can be found elsewhere.^{52–55} Standard values of $m = k_B T = 1$ and overall particle density $\rho_{DPD} = 3r_c^3$ were chosen, where the following DPD-reduced units are used: length in r_c , energy in $k_B T/r_c$, mass in particle mass m , and time in $\tau = r_c \sqrt{m/k_B T}$. The time step was set to $\Delta t_{DPD} = 0.01 \tau$ in DPD units, where the soft interaction forces used in our simulations allow for a much longer time step than when hard repulsion forces such as Lennard–Jones forces are used. Although results from DPD are sensitive to the time step,⁵⁶ the time step used in this study is lower than the conventional values of 0.04 – 0.06τ .^{55,57} Since DPD is used to model isothermal simulations, this method may not be appropriate for capturing adiabatic processes characterized with high-temperature gradients that can occur during shock wave propagation.⁴⁶ Because of this we will restrict our study to shock waves with low impulses (less than $10 \text{ Pa}\cdot\text{s}$) that cause negligible heating of the simulation system.

The coarse-grained model that we used is based off the work of Grafmüller et al.^{58,59} The systems considered here are constructed from 3 bead species: lipid head (H), lipid tail (T), and water beads (W). The model lipids have a headgroup consisting of 3 H beads and 2 hydrophobic tails, each consisting of 4 T beads (Fig. 32a), which corresponds to a coarse-grained model of dimyristoyl-phosphatidylcholine (DMPC) with an $H_3(C_4)_2$ architecture. Each coarse-grained chain-bead T represents 3.5 CH_2 groups, where the level of coarse-graining, $N_m = 3.5$.

The pair interaction between topologically nonconnected particles is described by a weakly repulsive potential:

$$U_{DPD}(r) = \frac{a_{DPD}}{2} \left(1 - \frac{r}{r_c} \right)^2, \quad (1)$$

where a_{DPD} is the maximum repulsion and $r_c = 1$ is the cutoff radius. The a_{DPD} values differ for different bead species and their values are taken from Grafmüller.⁵⁹ The interaction parameters are given in Table 5 and in general, the simulation parameters are chosen to match the mesoscopic behavior of the system.

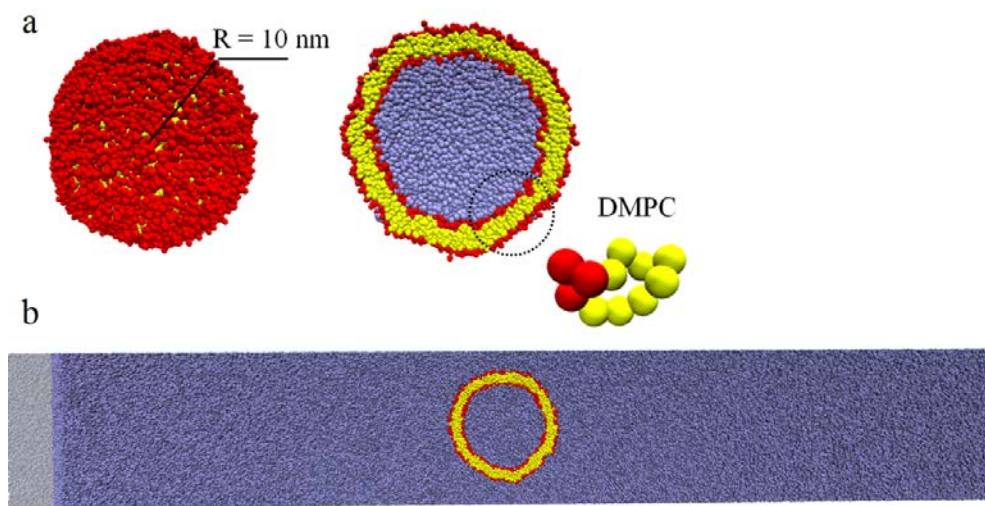


Fig. 32 a) A representative snapshot of the liposome surface (left) and cross-sectional area of the lipid vesicle (right): the liposome is composed of 5,551 lipids. H, T, and W particles are colored red, yellow, and blue, respectively. The liposome has a radius of 10 nm (14.5 r_c in DPD units). b) A representative cross-sectional area of the simulation box after initial compression.

Table 5 The interaction parameters a_{ijDPD} between pairs of beads where i and j belong to head (H), tail (T), or water (W) beads, respectively

Bead Type	Interaction parameter a_{ijDPD}		
	H	T	W
H	30	35	30
T	35	10	75
W	30	75	25

Topologically connected beads in lipids interact according to the harmonic potential, U_{harm} :

$$U_{harm}(r) = \frac{k}{2}(r - r_0)^2, \quad (2)$$

where k is the harmonic constant and r_0 is the equilibrium bond distance; the values of $k = 225 k_B T / r_c^2$ and $r_0 = 0.85 r_c$ are used. In addition, the hydrocarbon chains (tails) are stiffened by a bending potential that is enforced between 2 consecutive bonds:

$$U_{bend}(r) = k_\theta (1 - \cos \theta), \quad (3)$$

where the potential parameters are $k_\theta = 2 k_B T$ and $\theta = 180^\circ$.

To obtain the pre-shock structure, the vesicle structure was preassembled from 5,551 lipids, where the head groups were placed randomly in the inner and outer parts of the spherical membrane. Water particles were then placed randomly into the remainder of the simulation box. The hydrophobic tails of the vesicles and water particles were then equilibrated while the head beads were frozen (immobile) prior to subsequent short equilibration of the fully mobile system. The simulation box contains approximately 2,500,000 particles. This procedure produces a liposome with a radius of 10 nm ($14.5 r_c$ in DPD units), while cells of complex organisms are on the order of micrometers. This discrepancy in size is due to restrictions in the DPD method that are constrained to length scales of $O(100 \text{ nm})$, which must account for both the water and liposome in our simulation. Even so, using a coarse-grained model such as DPD allows for a more physical description of a liposome than all atom molecular dynamics simulations that can only simulate tiny membrane patches composed of hundreds of lipid molecules.⁵⁹ A smaller representation of the liposome may lead to higher curvature and lower stability, though it is expected that trends obtained from our system will be consistent with those that would be obtained using a larger liposome.

Shock waves were initiated with a momentum-reflecting mirror, which is a standard method for generating shock waves in computer simulation studies of lipid

bilayers.^{43,46,58} The fast shock waves generated from this method are numerically stable and have a well-defined shock wave front. In this method, the shock wave is created through an infinite-mass piston that moves in the positive z direction. All particles coming into contact with the piston surface are reflected, and the velocity relative to the moving wall is flipped in.⁴⁶ This procedure is comparable to standard shock wave experiments where a stationary target is hit by a fast-moving impactor. Upon impact with the piston, the target material is compressed and the resulting steep density gradient initiates a shock wave. After a short initial time, the piston was stopped while the initiated shock wave continues along the z direction (Fig. 32b).

The speed of the piston, v_p , and the final piston position were varied to produce different shock wave profiles, where the pressure was measured as function of time and z distance. The location of the liposome in the simulation box was sufficient to avoid direct impact with the piston during the shock simulation. In the first part of our study the piston was stopped after $t = 15\tau$, and the velocities of the piston were varied to 5, 10, and $15 r_c/\tau$ to produce shock waves with different pressure profiles. The resulting shock waves have Mach number of 1.49, 1.66, and 1.76, respectively. In the second part of our study, the piston was allowed to move longer, $t = 50\tau$, with v_p equal to 5 and $10 r_c/\tau$ to produce higher pressure impulses. The Mach numbers of these waves are equal to 1.87 and 2.45. To calculate the Mach number, which is the ratio of the speed of the shock wave in a fluid and the local speed of sound, we took into account the speed of sound of the DPD fluid (c_{DPD} 3.818–4.298 in DPD units).⁶⁰

To capture the time evolution of the shocked vesicle, the length of the simulation box in the direction of the shock impulse, L_z , must be sufficiently large to allow the shock front to travel for a long period of time. This study considers a relatively large simulation box: $50.72 \times 50.72 \times 326 r_c^3$ (corresponds to $35 \times 35 \times 225 \text{ nm}^3$), where the liposome is $29.0 r_c$ (corresponds to 20 nm) in diameter. Nonperiodic boundary conditions are used in all 3 directions in the simulation. Shrink-wrapped boundary conditions were used for the face that has the piston. The opposing face and the boundaries in the x and y dimensions are fixed. The simulation system was also bound with reflective walls that prevent particles from moving through the boundaries. If an atom moves outside of the wall by a distance Δx then it is put back inside the boundary by the same distance, and the sign of the corresponding constituent of its velocity is flipped. All simulations were executed using LAMMPS software from Sandia National Laboratories.⁶¹

To compare our simulation results with experimental data, it is necessary to relate DPD units of energy, length, and time scale to physical units. The basic length scale

(i.e., a physical size of interaction radius, $r_c = 0.69$ nm) is computed to match experimental values of the area per lipid molecule. The area per molecule in the simulations is $A_{DPD} = 1.25 r_c^2$, whereas the experimentally measured value is $A_{phys} = 0.596 \text{ nm}^2$.^{58,61} Therefore the length scale for our simulation is $r_c = \sqrt{A_{phys} / A_{DPD}} = 0.69$ nm.

Although the link between physical and simulation length scales is straightforward, the relationship between the experimental and computational time scales cannot be obtained directly. This is partially due to the faster dynamics observed by the coarse-grained system. The dynamics are accelerated due to the coarse-grained interaction potentials that are much smoother, therefore lowering energy barriers.⁶² Thus there is a need to compensate for this difference in dynamics by adjusting the time scale. There are several concepts that try to map the dynamics of a coarse-grained system with an experiment; however, open questions remain.⁶² One way to estimate the time scale in physical units, is to match the self-diffusion constant of a DPD particle with those obtained from a physical system⁵⁵:

$$\tau = \frac{N_m D_{sim} r_c^2}{D_{phys}}. \quad (4)$$

Here we used DMPC lipid ($D_{phys} = 5 \mu\text{m}^2/\text{s}$) as the physical system, where the in-plane diffusion coefficients for a DPD particle is $D_{sim} = 0.016 r_c^2 / \tau$.⁴⁰ From Eq. 4, we found that the time scale $\tau = 5.3$ ns.

We map differences in pressure, $\Delta P = P - P_0$ in $k_B T / r_c^3$, where P_0 is the pressure at equilibrium. Values of pressure obtained from DPD are unrealistically high even under standard conditions, for reasons we will discuss in the next paragraph. Even so, ΔP could be used to discern trends in our system, where we can use the standard conversion factor⁴⁷ $k_B T / r_c^3$, which is equal to 13 MPa for our simulation.

5.5.3 Results

5.5.3.1 Pressure Profile and Liposome Structure and Movement during Shock Waves with Low Overpressure Peaks

To determine the speed of the shock wave, the location of the shock wave front in z direction was identified as a function of simulation time. The position of the liposome was monitored during the simulation and pressure profiles were computed. This is achieved by dividing the simulation box into 11 bins, where each bin contains approximately 250,000 particles. Smaller bins produce qualitatively

similar results, but are more prone to statistical errors due to inadequate sampling. The initial speed of the shock wave propagation was calculated from the slope of the peak pressure versus time curve, which exhibits a near-linear relationship (data not shown).

The second overpressure peak (Fig. 33a) corresponds to the reflection and back propagation of the shock wave off the edge of the simulation cell. The pressure curves shown in Fig. 33a correspond to shock waves with a Mach number, $M = 1.49$, where the Mach number is a dimensionless quantity representing the ratio of the speed of the shock wave in a fluid and the local speed of sound. The curve labeled 107.8–127.3 nm represents the change in pressure at the location of the liposome, which was placed at 117.4 nm from the center of the wave initiation, and did not move significantly. The second peak in the pressure profile represents the second positive phase due to reflection from the simulation box wall. Figure 33b shows pressure (P) profiles obtained during the simulation at various distances, d , from the initiation of the shock wave. As expected, the peak overpressure decreases with distance from the wave initiation and causes almost instantaneous overpressure, followed by a longer interval of negative pressure.

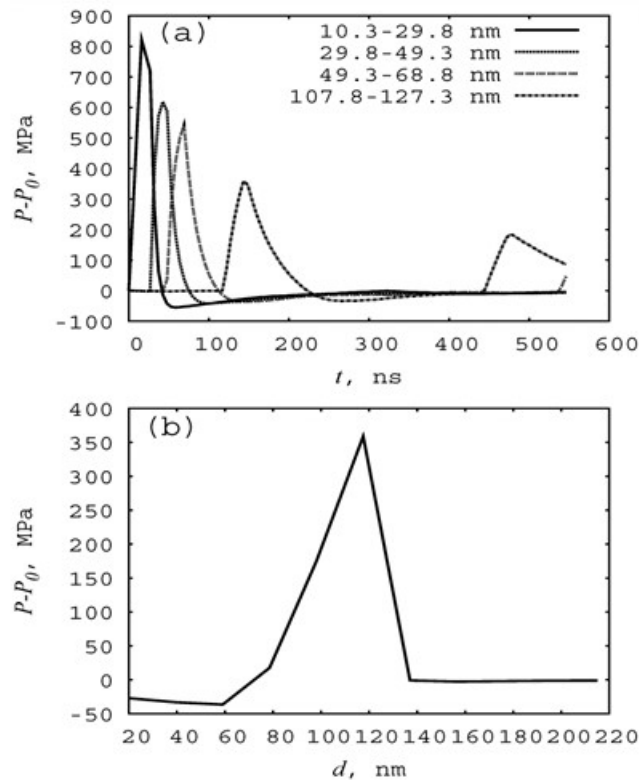


Fig. 33 The supersonic shock wave at the various distances from its launch. The liposome is located at 117.4 nm. The Mach number is 1.49. b) The pressure profile at $t = 150$ ns after the wave initiation at the liposome location.

To produce different pressure profiles for mild shock, the piston speed v_p was varied while keeping the compression of the box constant. We considered values of v_p equal to 5, 10, and 15 r_c / τ , which produced blast waves with Mach numbers of 1.49, 1.66, and 1.76, respectively. This produced shock profiles with overpressure peaks equal to 359, 495, and 633 MPa, respectively (Fig. 34a), which were measured at the location of the liposome (approximately 117.6 nm). The piston was stopped at a distance of 107.25 nm from the liposome.

The curves shown in Fig. 34 exhibit characteristics of extracorporeal shock waves, which are characterized by a rapid increase to a relatively high pressure (>100 MPa) in the span of a few nanoseconds, followed by an exponential descent. For these shock waves the duration of the positive phase is on the order of 100 ns, and is followed by a comparatively small tensile wave component below ambient pressure. This negative phase can experience compressive pressures up to 15 MPa, where the duration is long compared to the positive phase (around 2,000 ns)^{50,51}. In our simulation, the duration of the negative phase is shorter because of limitations in the simulation box size, which leads to a reflective wave earlier than the shock wave duration. The shock wave characteristics obtained in our simulations are different from blast shock waves, which are described by a lower (O(kPa)) value of the peak pressure, where positive overpressures ΔP higher than 400 kPa are considered potentially lethal.⁵² Blast shock waves also exhibit a much longer positive phase duration (O(ms)). Although, different shock waves (e.g., blast and extracorporeal) produce different pressure profiles, its impulse is defined as the pressure integrated over time and is a dominant factor in changing the permeability of living cells rather than the peak pressure.¹³ The impulse is computed from

$$I = \int_0^{t_+} [P(t) - P_0] dt, \quad (5)$$

where $P(t) - P_0$ is the shock wave positive overpressure and t_+ is the positive phase duration. Our simulation produced shock waves with I equal to 1.31, 1.93 and 2.49 Pa•s, respectively. The overall pressure impulse including the reflective positive phase, $I_{tot} = I_1 + I_2$ is found to be 1.87, 2.79, and 3.59 Pa•s.

When the shock wave impacts the liposome, its location slightly changes in the simulation box, where it initially moves in the positive z direction. Then, the liposome flows in the negative z direction as the reflective wave makes contact (the second positive phase). The overall movement of liposome in the lateral direction to the shock wave is found to negligible (less than 1%). With increasing v_p , the reflective wave hits the liposome before the pressure reaches ambient value. These results show that the primary shock wave is followed by the translational motion of lipid vesicle due to inertial forces. This translational motion of the lipid vesicle is

similar to a behavior of cells under shock in vitro, where the cells move with the surrounding liquid in the direction of the shock wave. Cells subjected to shock in vivo would require higher pressures or more shocks than cells in vitro to sustain damage and death. In vivo, the neighboring cells, the extracellular matrix, and basement membranes fix cells, such that when they are subjected to shock they demonstrate nonlinear, anisotropic, inhomogeneous behavior on the macroscale. In the context of TBI this linear acceleration could lead to diffuse axonal injury.⁵³

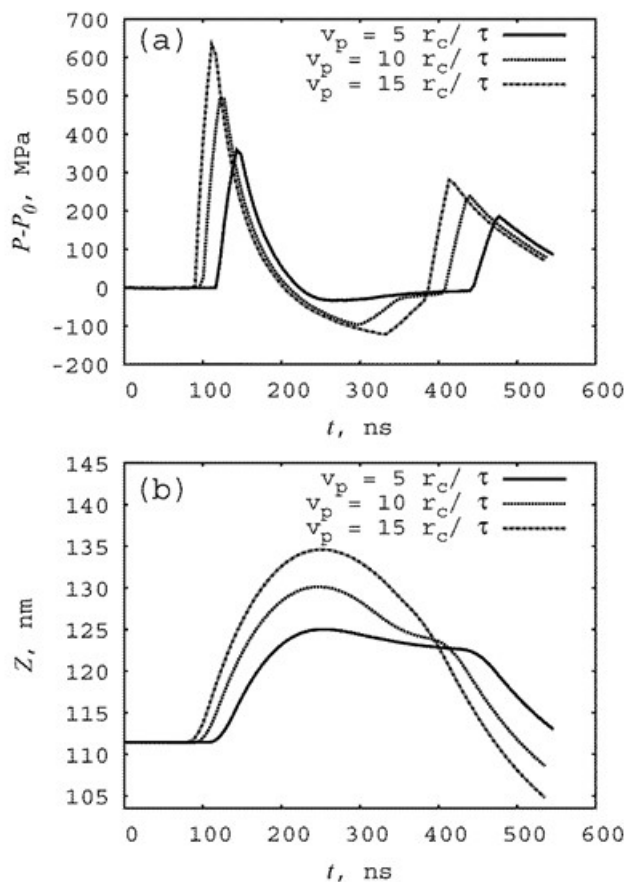


Fig. 34 The shock wave at the location of the liposome for the various piston speeds v_p and b) movement of the center of mass of the liposome in z direction

To characterize a change of the liposome size and the deviation from an equilibrium vesicle shape, the diagonal principal moments of the gyration tensor λ_{xx}^2 , λ_{yy}^2 , and λ_{zz}^2 were computed using

$$\lambda_{dd}^2 = \frac{1}{N} \sum_{i=0}^N (r_{id} - r_{com})(r_{id} - r_{com}), \quad (6)$$

where r_{com} is the coordinate of the liposome center of mass, r_{id} is the d coordinate of bead i of the liposome, and N is number of beads in the liposome. The radius of

gyration, R_g , which defines the size of the lipid vesicle, is given by the sum of the principal moments:

$$R_g = \sqrt{\lambda_{xx}^2 + \lambda_{yy}^2 + \lambda_{zz}^2} \quad (7)$$

and deviation from a spherical shape for the liposome is given by the asphericity, b :

$$b = \lambda_{zz}^2 - 0.5(\lambda_{xx}^2 + \lambda_{yy}^2). \quad (8)$$

Figure 35 shows the change in R_g and b with time, where we observed that changes in size of liposome are accompanied by changes in its shape. Initially the liposome is compressed during the positive pressure phase, where R_g is changed by 10.3%, 11.6%, and 12.7%, respectively. After compression the liposome undergoes extension during the negative pressure phase, where R_g is increased by 2.0%, 9.0% and 14.7% compared with its initial size (Fig. 35a). During the reflective wave, the process repeats with lower values for both compression and extension. Notably, the extent of liposome compression does not strongly depend on the pressure pulse compared with an extent of liposome extension (Fig. 35b). This finding suggests that liposome extension is very sensitive to the change in the negative pressure phase, which can consequently lead to more structural damage of the cell membranes. This is consistent with the general properties of living tissues, which fail more easily under tension than under compression.³⁷

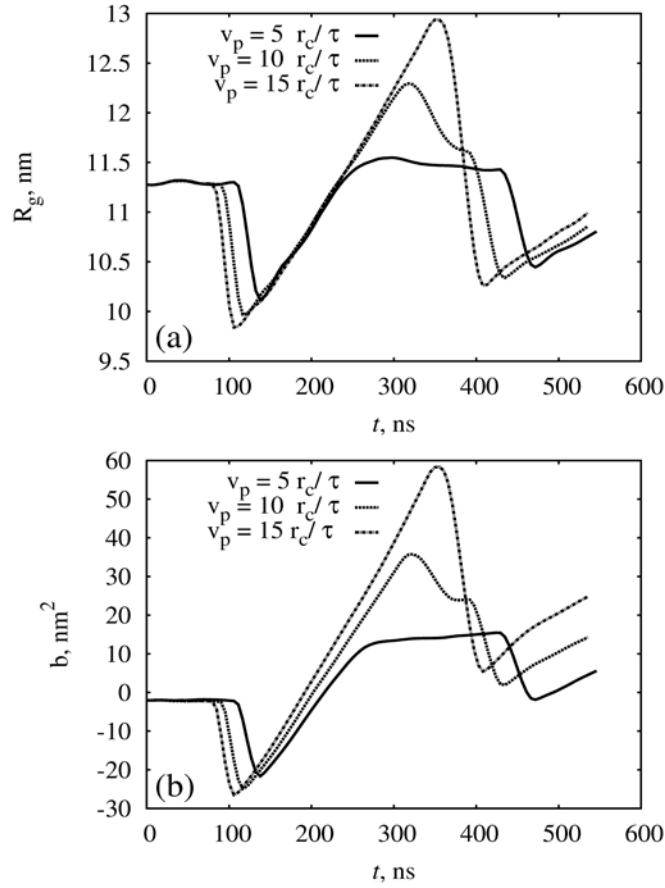


Fig. 35 Change of liposome size and shape vs. time: a) radius of gyration of the liposome, R_g and b) asphericity

5.5.3.2 Pressure Profile and Liposome Structure and Movement during Shock Waves with High Overpressure Peaks

To produce higher overpressure, 2 simulations were performed with piston speeds v_p equal to 5 and $10 r_c / \tau$, respectively. In these simulations, the piston was allowed to move longer and the piston was stopped at the distance of 83.1 nm from the liposome. Therefore the positive pressure phase values are greater than those values reported early though the negative pressure values are not significantly smaller (see also Figs. 34a and 36a). The Mach numbers of these waves are equal to 1.87 and 2.45 for v_p values 5 and $10 r_c / \tau$, respectively. Since the shock waves move faster in these simulations, the reflection wave reaches the liposome earlier than in the previous simulations, though the durations of the positive and negative phases are similar (see also Figs. 34a and 36a). In the case of the fastest shock wave with Mach number of 2.45, one can see the emergence of a third pressure peak that corresponds to the second reflective wave. In addition, the liposome travels a greater distance in the positive z direction than the shock waves discussed early which have a lower

overpressure peak (see also Figs. 34b and 36b). The positive impulse of these shock waves is found to be 3.33 and 5.57 Pa•s for v_p values 5 and 10 r_c/τ , respectively, for the first overpressure peak. I_{tot} for these wave are 4.91 and 7.09 Pa•s for v_p values 5 and 10 r_c/τ , respectively.

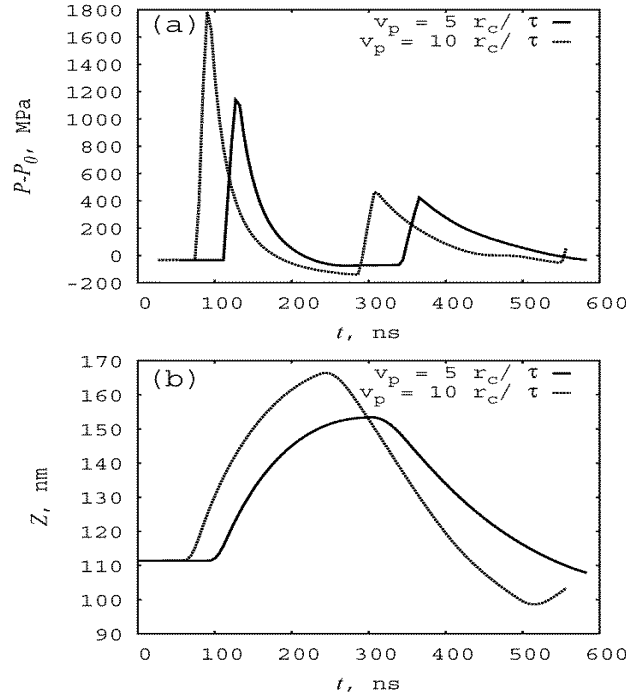


Fig. 36 The shock wave at the location of the liposome for the various piston speeds v_p .
b) Movement of the center of mass of the liposome in z direction.

The size and shape of the liposome changes similarly to those associated with the slower moving waves during initial impact of the shock wave, but the reflective portion of the shock waves has a stronger impact on the liposome size (see also Figs. 35 and 37). Interestingly, the liposome undergoes less movement in the z direction for $v_p = 10 r_c/\tau$ than $v_p = 5 r_c/\tau$ (Fig. 37b). This is caused by the reflective wave that reaches the liposome before the vesicle was fully stretched.

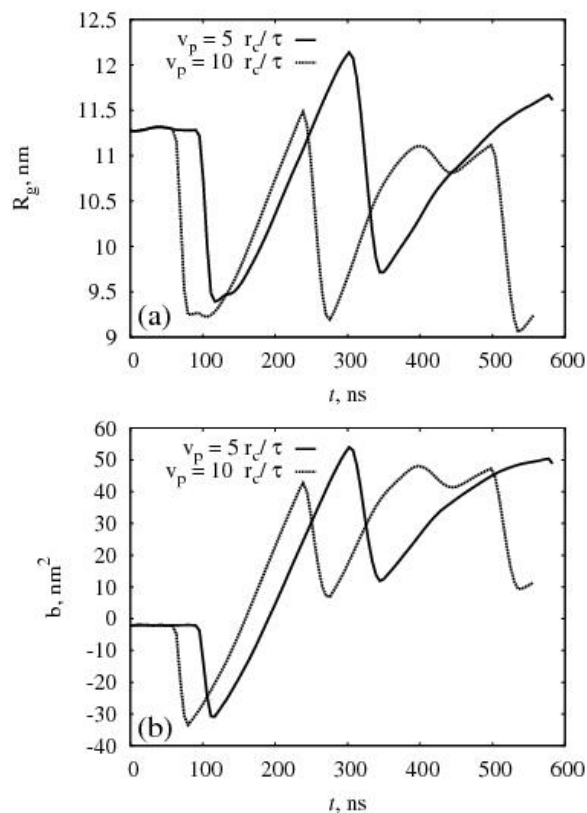


Fig. 37 Change of liposome size and shape vs. time: a) radius of gyration of the liposome, R_g , and b) asphericity, b

5.5.3.3 Structural Changes of Hydrophobic Layer of the Liposome

We observe damage in the lipid layer of the vesicle as a result of impact with the shock wave (Fig. 38a). Since the hydrophobic layer of the liposome is more fluidic than the polar layer, the hydrophobic layer should be damaged at a lower pressure, which we observe in our simulation. This damage will alter the membrane permeability, which we characterize by assessing the hydrophobic layer structure.

To do this, we use the concept of a “negative” or inverted image. Namely, we consider any space that is not populated by hydrophobic beads as being “occupied” by a dummy particle, where the size of this particle is equal to the size of the empty space. This is achieved by dividing the spherical hydrophobic layer into bins, with a grid spacing of $0.69 \times 0.69 \times 0.69$ nm, which is the minimal space resolution. Space adjacent to the outer and inner part of the hydrophobic layer is also divided in the same manner, though the thickness was chosen to be twice the bin size to reduce computational burden.

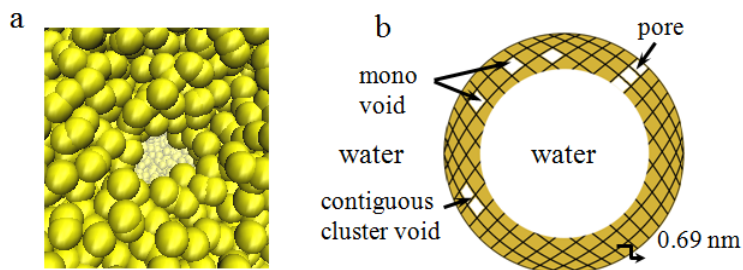


Fig. 38 The snapshot of a pore in the hydrophobic layer of the lipid vesicle, W and H beads removed for clarity. b) Schematic of possible damage of the hydrophobic layer.

This calculation was achieved through software developed in-house⁶³ that identified the size and number of all connected voids during the simulation. For each snapshot of the trajectory, “empty” bins that were not populated by any hydrophobic beads were calculated. If the empty bins are solitary (i.e., they do not neighbor any other empty bins), we identify them as mono voids. Second, we identified clusters made of the empty bins, where contiguous cluster voids arise from several connected voids.

At the start of the simulation (before any impact of the shock wave), 2 big clusters of dummy particles are present, which correspond to inner and outer adjacent layers to the hydrophobic part of the liposome (Fig. 39). Even before impact, some number of mono voids may be present. Upon impact, the number of mono voids could change and small contiguous cluster voids can form. The small cluster voids are composed of 2 empty bins, where the large clusters can vary in size, but are always larger than 3,000 bins. There are no clusters composed of empty bins between 2 and 3,000. When a pore forms, a contiguous void traverses the hydrophobic layer, and the outer and inner adjacent layers become connected such that one very big cluster of dummy particles is formed (see Fig. 39b). Thus a pore in the vesicle links water inside of liposome with water from the outside through a series of connected empty bins (Fig. 38b).

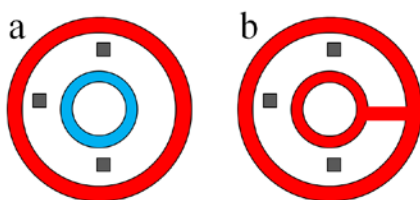


Fig. 39 Schematic representation of our method. a) Two large clusters are present; they are composed from adjacent outer and inner layers and colored in red and blue, respectively. Small cluster voids are in grey. b) The liposome has a pore, and one large cluster in red is present along with some number of small clusters.

For the lowest overpressure peak in Fig. 40a, $P_{max} = 358$ MPa, there are no significant changes in the structure where only the formation of mono voids was observed. While N_v at compression is slightly reduced compared with N_v prior the shock, N_v at extension P_{min} approximately -34 MPa is slightly higher and could suggest the onset of membrane disruption due to cavitation. This agrees with Lin et al.,⁶⁴ who determined that for very short pulse shock waves that the intrinsic cavitation threshold is 26–35 MPa. When the pressure profile has a higher peak, $P_{max} = 495$ MPa, the number of mono voids is significantly increased under extension, which corresponds to the negative portion of the pressure profile where a few contiguous cluster voids also appear. The maximum number of mono voids occurs at the pressure minimum, where the liposome is the most extended. At both of the positive pressure peaks $N_v = 0$, which corresponds to significant compression of the vesicle (Fig. 40b). For the pressure profile with $P_{max} = 633$ MPa, we observed a similar outcome, but we detected the formation of a pore under the extension, where $P_{min} = -121$ MPa. This pore was transient and closed as the reflective compressive pressure reached the liposome. Thus, our results suggest that the lipid membranes are more sensitive to tensile than to compressive deformation, where our results indicate that the pressure threshold for mechanical poration of a lipid membrane is P_{ext} approximately 121 MPa under tensile deformation.

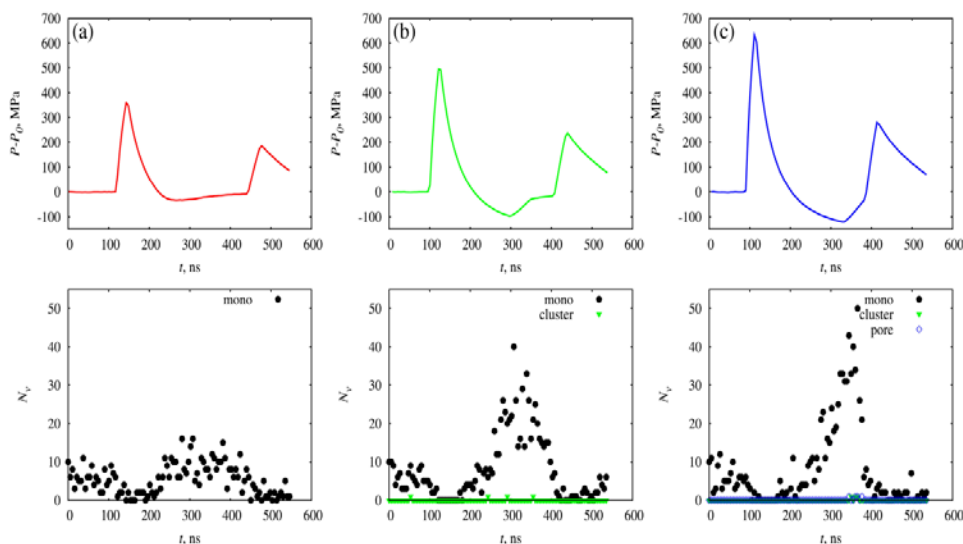


Fig. 40 Number of voids in the hydrophobic layer as function of pressure profile shows the change in the number of voids in the hydrophobic layer, N_v , with time, t , during propagation of the shock wave for our systems with low overpressure peaks

Interestingly, a higher overpressure peak, $P_{max} = 1,140$ MPa (Fig. 36a), that corresponds to $I = 3.33$ Pa•s does not produce significant damage to the lipid membrane, but impact with the second reflective positive peak of pressure, $P_{ref} = 423.7$ MPa results in pore formation, which lingers even after the reflective wave passes through the liposome and the pressure values are significantly reduced (Fig. 41a). In this case the overall pressure impulse is 4.91 Pa•s. The negative pressure values were smaller than P_{ext} , thus no pores were formed at the extension phase of the shock wave. Our results also show that damage to the cellular membrane occurs for lower pressures under repetitive exposure, which is in agreement with experimental observation.⁵⁰ We observed creation of the pore in the lipid vesicle during the positive pressure phase for the largest peak pressure of $P_{max} = 1,786$ MPa, which corresponds to pressure impulse of $I = 5.57$ Pa•s ($I_{tot} = 7.09$ Pa•s). Also, these pores did not re-seal during the simulation. Thus our results indicate that direct poration for lipid bilayer occurs for pressure impulse values higher than 5 Pa•s. Our results are in good agreement with other experiments⁶⁴ that have shown that fluorescence uptake, which is related to cell permeability, starts to change around 5 Pa•s.

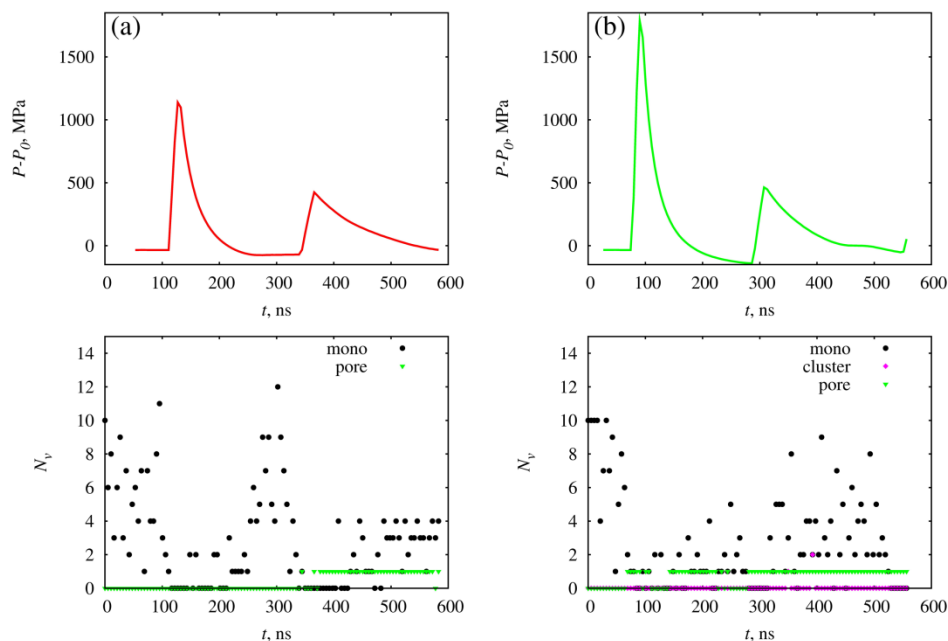


Fig. 41 Number of voids in the hydrophobic layer as function of pressure profile

5.5.4 Discussion

In this computational study, we used a coarse-grained model of a lipid vesicle as a generic model of a cell membrane to elucidate the general principles of the cellular

damage induced by the shock wave direct passage through the cranium. Results indicate that the extent of liposome compression does not strongly depend on the pressure pulse and that liposome extension is very sensitive to changes in the negative pressure phase. In addition, the structural integrity of the vesicle is altered as pores form in the lipid membrane at pressures generated by supersonic shock waves, when the pressure impulse of the shock wave is greater than 5 Pa•s. Even so, damage to the lipid membrane may arise at lower compressive pressure under repetitive exposure, if the overall pressure impulse is greater than 5 Pa•s. Consequently, these changes in permeability may lead to an influx of sodium, potassium, and calcium ions, which can lead to cell death. Direct poration also can occur during the tensile portion of the blast wave but only for very high negative pressure values P_{ext} approximately -120 MPa. Although, the accuracy of our results is subject to the limitations of coarse-grained modeling, our results are in qualitative agreement with experiments, such as those that consider the existence of transient cavitation in lipid membranes.⁵¹

5.6 Impact of Blast-Dependent Cellular Damage on the Local Field Potential (LFP) in a Large-Scale Simulation of Cerebral Cortex Modeling Simulation

5.6.1 Introduction

Interactions between brain structure and function occur across multiple scales, including diverse events such as ion channel deformation impacting neurotransmitter release,⁶⁴ coordinated firing activity underpinning oscillations in the LFP,⁶⁵ and large-scale oscillations that synchronize activity across spatially disparate brain regions.⁶⁶ This complex coordination of events across scales is thought to enable cognition^{60–69}; however, observing cross-scale interactions directly is not possible given the current state of in vivo human neuroimaging methods.^{67,70–71} Large-scale modeling simulations are able to work around many of these technological limitations since interactions between microlevel changes and contemporaneous macrolevel brain states can be observed directly.

Research on the neural underpinnings of TBI has primarily focused on large-scale morphological changes such as axonal degeneration and/or neuronal morbidity⁷²; however, we are interested in understanding how these structural changes manifest in a change in the overall functional activity that can capture fluctuations in human performance. In this project, we focus on how cellular damage following a blast exposure manifests changes to the LFP of simulated patches of the brain. The LFP activity serves as a proxy for the brain activity recorded by electroencephalography (EEG) from the scalp in cognitive neuroscience experiments that link dynamics

changes in EEG with fluctuations in task performance. As such, this model provides a way to investigate how cellular changes may link to differences in performance. We specifically investigate how cellular damage following a blast exposure manifests in changes to the LFP of simulated patches of the brain.

We use a compartment-level model of cerebral cortex that simulates a brain region, and we use the overall network electrical activity to compute the LFP in a simulated brain region. Recently, molecule-level simulations have predicted the appearance of blast-induced sodium and potassium permeable pores on the surface of the neuronal membrane.⁷³ This prediction was supported by recent experiments on cell cultures. These results imply that cellular damage due to blast exposure could induce electrophysiological changes that negatively impact brain function in the absence of either cell death or large-scale structural impacts such as degeneration of white matter tracts. Our use of a biophysically detailed compartment model of cerebral cortex has 2 advantages. First, we expect our network to produce cognitively relevant low-frequency electrical activity in a natural way.⁷⁴ Second, because our simulated neurons have explicitly defined cellular morphologies and membrane properties, we can explore the impact of damage on different regions of the neuron.

5.6.2 Materials and Methods

5.6.2.1 Individual Neuron Model

We adapted neurons from the thalamocortical network model described by Traub et al.⁷⁵ to run within the GENESIS neuronal simulation environment. Individual neurons were simulated using between 50 and 137 cylindrical compartments representing somata, axons, and apical and basal dendrites. Each compartment is represented by a differential equation describing its electrical activity (Eq. 9). Differential equations were solved using the exponential Euler method at a 50- μ s time step. Passive current properties within and between compartments were modeled via cable equations.⁷⁶ Electrical activity within each neuronal compartment was simulated using up to 15 distinct Hodgkin-Huxley type voltage-activated calcium, potassium, and sodium ion channels. Excitatory neurons (pyramidal and spiny stellate in cortex; thalamocortical relay cells) were associated with α -amino-3-hydroxy-5-methyl-4-isoxazolepropionic acid (AMPA) and NMDA synapses, while inhibitory neurons (basket, chandelier, small interneurons, and thalamic reticular nucleus cells) were associated with gamma-aminobutyric acid (γ -aminobutyric acid or GABA) synapses.

$$dV/dt = g_{Na+} \Delta V_{Na+} + g_{K+} \Delta V_{K+} + \dots + g_L \Delta V_L . \quad (9)$$

Nanoscale modeling of blast impact on the membrane of neurons predicts that pore sizes will be sufficiently large to allow the flow of both sodium and potassium ions,⁷⁴ but too small to allow through calcium ions. We theorize therefore that blast-induced pore formation is likely to alter the permeability of the neuronal membrane to sodium and potassium. Hodgkin-Huxley-like simulations of neuronal electrical activity include a term to represent the passive permeability of the neuronal membrane to sodium and potassium in the form of the membrane resistance, R_m . We operationalize increasing numbers of pores being formed on the membrane as a reduction in the resistance of the membrane. Since the relationship between pore formation and changes in electrical resistance of the membrane has not been experimentally elucidated, we performed a simple parameter sweep of how changes in membrane resistance impact model electrical activity.

Additionally, while there is a wealth of experimental evidence linking blast to changes in white matter tracts, there is very little discussing the impact of blast on other parts of neurons. Here we wanted to determine if the location of pore formation had any impact on degradation of network activity. Since our model represents each neuron using multiple compartments, we tested the differential impact of damage to the whole cell, axonal compartments only, and contemporaneous damage to both the soma and the dendrites.

5.6.2.2 Cortical Network Model

Our cortical network represents a $150\text{-} \times 150\text{-} \times 2,871\text{-}\mu\text{m}$ patch of cortex along with a corresponding thalamic relay and downstream thalamic target (Fig. 42a–b). Connections between axons and synaptic targets were weighted as an exponentially decaying function of the Cartesian distance. Connection probabilities between neuron types ranged from $p = 0.01$ to 0.667 . In our model, 335,067 connections were simulated between 549 neurons. Axonal conduction delays were proportional to the distance between the soma of the sending neuron to the synaptic compartment. Action potentials were transmitted between neurons as all-or-none messages from the soma of the firing cell directly to their synaptic targets on destination cells with a distance-weighted conduction delay (1 s/m). Ten percent of cells received 200-Hz Poisson spike trains representing background input from other cortical areas.

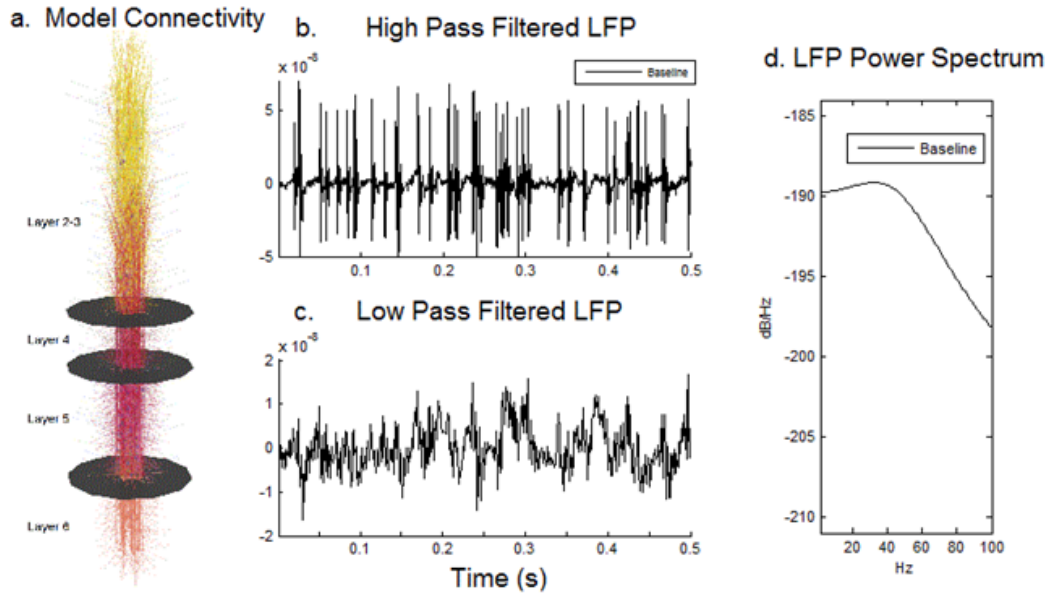


Fig. 42 Overview of cortical network model and output. a) Visual representation of the model, showing 549 cortical neurons with layer boundaries depicted as discs. b) High-pass filtered LFP for the baseline (undamaged) model shows distinct clusters of spikes. c) Low-pass filtered LFP shows slow oscillations similar to those seen in EEG. d) Parametric power spectrum shows relatively low power in higher frequencies, again similar to electrocorticography (ECoG) and EEG.

5.6.2.3 Model Network Activity

Simulated model network activity was recorded at a point 7 mm above the simulated cortex with the assumption of perfect conductance between the location generating the electric field and the recording site. Overall activity was summed as a distance-weighted membrane potential from each simulated compartment at each time step. The results from the first 1 s of data were excluded to allow the model to settle from initial conditions. Data were analyzed using Matlab. Action potentials were obtained by resampling to 5,000 Hz and then high-pass filtered using a ninth order Butterworth filter with a roll off of 50 Hz (Fig. 42c). Number of action potentials per simulation was determined using a threshold, with the mean action potential firing rate simply being that number divided by the length of the simulation. LFPs were first resampled to 1,000 Hz and then low-pass filtered using a 48th order Butterworth filter with a roll off of 300 Hz (Fig. 42d).

5.6.3 Results

Electrical activity within the cerebral cortex is thought to underlie human cognitive processes that are disrupted in patients diagnosed with mTBI. Here we explore how proposed blast-induced microscale alterations to neurons alter our simulated network's ability to generate experimentally relevant frequencies of electrical

activity. One proposed mTBI-related damage mechanism is the formation of blast-induced sodium and potassium permeable pores across the neuronal membrane. We operationalized the impact of predicted sodium and potassium permeable pores as changes in the electrical resistance of our simulated neuronal membrane and measured changes in macrolevel model electrical activity.

Network-level electrical activity was obtained from the distance-biased summed electrical activity of all 585 simulated neurons. To generate data similar to that observed in vivo, we processed model output in 2 ways. First, we used a high-pass filtered model output to produce a signal commensurate with extracellular recordings that allows us to measure neuronal activity in terms of number of action potentials (Fig. 43a–e). Second, model output in a low-pass filtered form was used to obtain a LFP, which is thought to be the neuronal basis for both EEG and magnetoencephalography (MEG) (Fig. 43f–j).

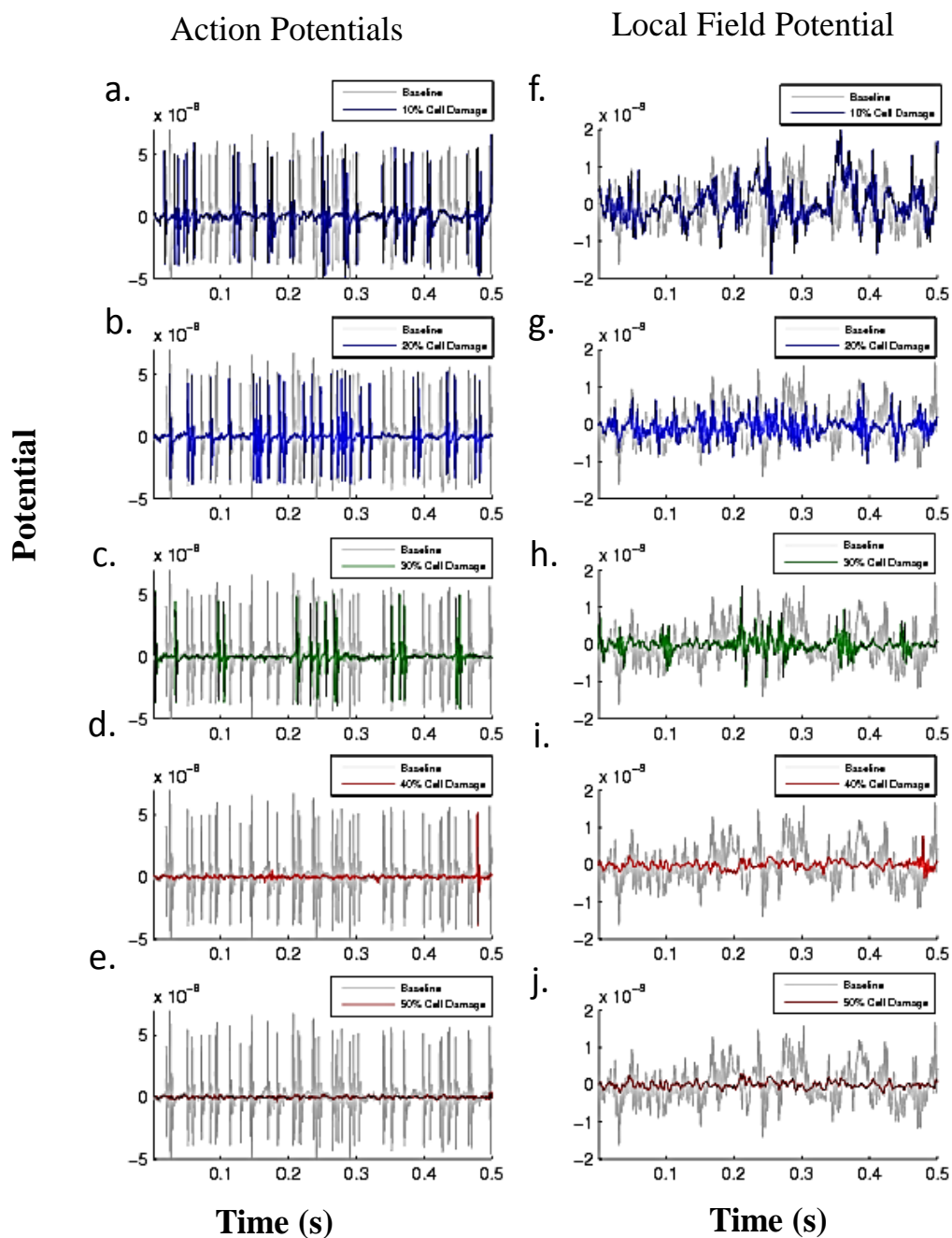


Fig. 43 Comparison between baseline model output (gray) and damaged model output (color). Each row shows how the model activity changes as a function of increasing the percentage of damage to the cell membranes, ranging from 10%–50% in increments of 10%. Potential is shown in arbitrary units for the 0.5 s of model data (total simulation time 19 s). a–e) High-pass filtered model outputs designed to mimic extracellular recording techniques to measure action potential frequency. f–j) Low-pass filtered model output designed to mimic the LFP. Note reduction in amplitude and duration of low frequency activity.

Additionally, since the functional implications of damage to specific neuronal regions are currently unknown, we measured changes in macrolevel model electrical activity response to damage to either dendrites and soma, or axons.

5.6.3.1 Blast-Induced Pore Formation on the Neuronal Membrane Reduces Both Network Activity and Neuronal Firing Rates

We first tested the impact of blast-induced pore formation on the whole cell's membrane on our simulated network activity. As expected, we found that increasing levels of damage (10%–50%) reduced overall neuronal activity (Fig. 43a–e). Additionally we found that as damage to the membrane increased, there was a reduction in the overall power of the simulated LFP and that this reduction was stronger in the low-frequency component. Figure 43f–j shows damage-induced changes to the shape and structure of the simulated LFP. There is a reduction in both the prevalence and amplitude of voltage fluctuations occurring on the time scale of hundreds of milliseconds as damage increases from 10%–50%. For instance at the 0.3-s point of the baseline simulation (light gray line in all traces), there is a large amplitude double-peaked voltage fluctuation; however, similar voltage fluctuations disappear as damage levels are increased (green and red traces).

The reduction in prevalence of large amplitude voltage fluctuations occurring on the time scale of hundreds of milliseconds is measureable as a change in the power spectrum (Fig. 44a). We observe that for a given damage level, there is a stronger reduction in the low-frequency component of the LFP (less than 50 Hz) than in its high-frequency component (more than 50 Hz) (Fig. 44b). The low-frequency component of the LFP reached its floor (where greater damage levels no longer reduce the power of the signal) at the 40% level of damage as indicated by very little difference in power between 40% and 50% power below 50 Hz. The high-frequency component of the LFP is reduced in power more gradually.

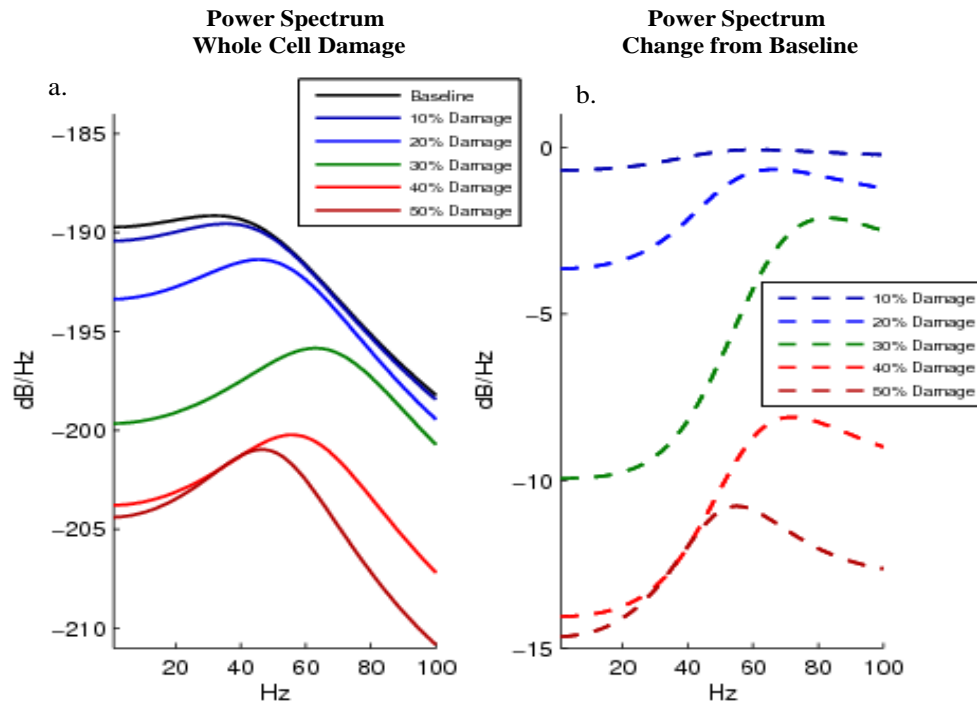


Fig. 44 Effects of cell membrane damage on spectral power of model. Across both subplots, colored lines represent change in the power spectrum with increasing levels of damage to the cell membrane (black is baseline, damage increases from blue to red in increments listed in legend). a) Effect of damage to the whole cell. b) Difference in spectral power of model between baseline (undamaged) and damage to the whole cell. Each line plots the overall reduction in power/decibels between the baseline (undamaged) model and models with increasing percentage of damage to the cell membrane. As expected, increased damage led to increased reduction in power as indicated by the negative values. Model shows larger decrease in low-frequency power due to membrane damage.

5.6.3.2 Damage to Axons Reduces Network Activity and Neuronal Firing Rates More Severely Than Damage to the Cell Body and Dendrites

Additionally, we tested to see if damage to specific neuronal regions had a significant impact on the shape and structure of the LFP. First, we selectively damaged simulated axons while leaving the soma and dendrites undamaged. Second, in a separate set of simulations, we only damaged the soma and dendrites while leaving the axons intact.

We found that overall damage to axons was more impactful than damage to the soma/dendrites (Fig. 45). At minimal damage levels (10%), damage to the soma/dendrites actually increased power in the low-frequency range (1–50 Hz), while damage to the axons decreased power over the same frequency range (1–50 Hz). Across all damage levels, damage to the axons is worse than damage to the soma and dendrites except when damage is between 10% and 20% and when the frequencies are above 40 Hz (Fig. 45).

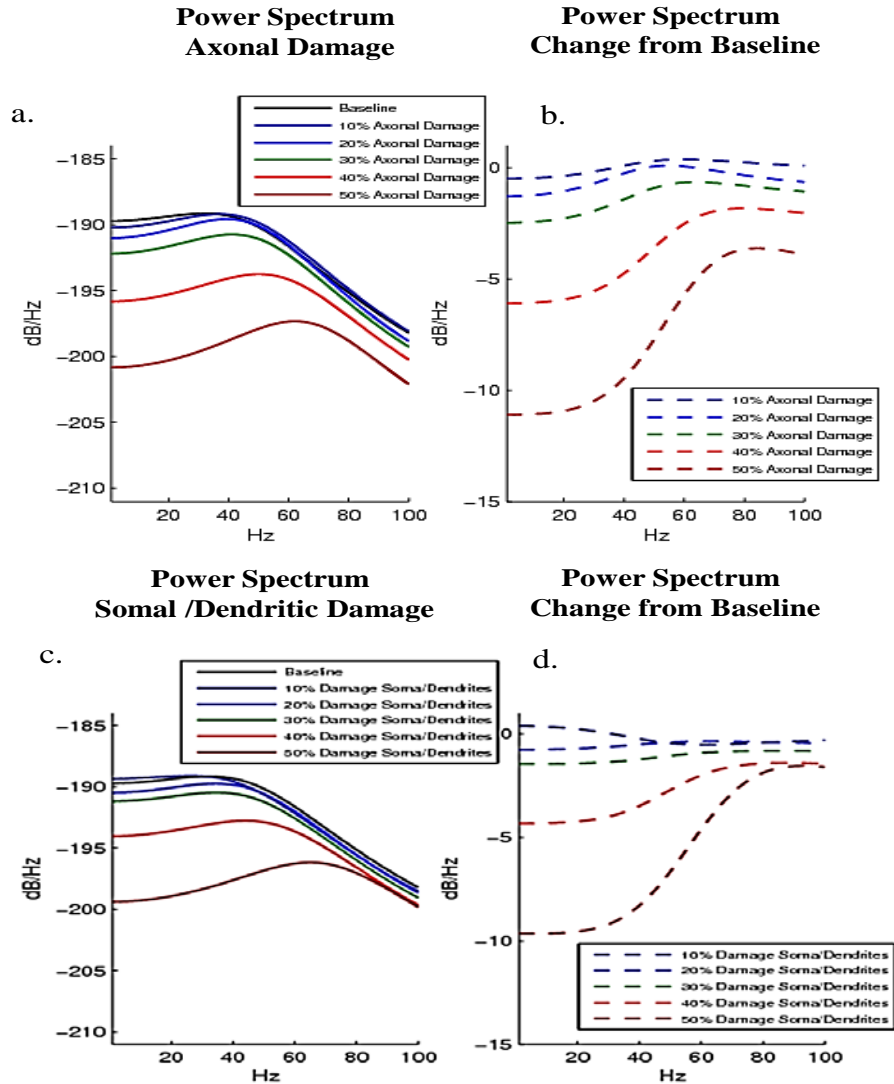


Fig. 45 Difference in spectral power of model due to damage to axons and soma/dendrites. Damage is modeled as changes to specific compartments of the model that comprise either simulated axons or simulated somas and dendrites. a) Effect of selective damage to only the axonal compartments of the cell. b) Reduction in power from baseline for axonal damage. Low-frequency power is reduced to a greater extent than high-frequency power. c) Effect of selective damage to the soma and dendrite compartments of the cell. d) Reduction in power from baseline for damage to somal and dendritic compartments of the model. Minor damage (10%) is associated with a small increase in low-frequency power. More damage (40%–50%) causes a drop in low-frequency power. b) and d) Comparing these plots reveals that damage to the soma and dendrites results in greater power reductions in high frequencies at smaller percentages of damage (10%–30%) while damage to the axon reduces power in the low frequencies at all damage levels (10%–50%) and also at high frequencies for larger values of percent damage (40%–50%).

Damage restricted to either axonal or somal/dendritic regions act qualitatively like damage to the whole cell with low-frequency power dropping in power faster than higher frequencies (Figs. 44a–c). In all tested conditions (whole cell, axons, soma/dendrites), damage at the 10% level results in only a small changes from baseline. When damage is at the 20%–30% level (light blue and green), damage to the entire cell is much greater than damage to either region on their own. At the 40%–50% level damage level for the whole cell, frequencies below 50 Hz LFP power hit the lowest levels possible, while simulations with only damage to a single region are unsaturated.

5.6.3.3 Changes in Neuronal Firing Rate

We also analyzed high-pass filtered model output to determine the mean rate of neuronal firing within our simulations. Changes in mean action potential firing rates confirm and support our results from the previous section that damage to the axons reduces model neuronal activity more vigorously than damage to the soma and dendrites.

As expected from changes to the power spectrum of the LFP, as damage to the whole cell increases (shown in Table 6), we observe an overall decrease in mean action potential firing from a baseline level of 69 to 0 measured AP/s.

Additionally damage to the axons always reduces neuronal firing rates more than damage to the soma/dendrites (Table 6). For instance, damage to the axons reduced firing rates by 2 Aps/s more than damage to the soma and dendrites at the 10% level of damage and by 12 Aps/sec at the 50% damage level (Table 6).

Table 6 Neuronal firing rate

Cell Area	Neuronal firing rate ^a (APs/s)				
	Damage level				
	10%	20%	30%	40%	50%
Whole cell	69	55	34	7	0
Axons	75	65	55	42	24
Soma and dendrites	77	71	66	56	36

^a Baseline = 69 AP/s

5.6.4 Discussion

In this project, we used a compartment-level model of cerebral cortex to simulate the electrical activity for a brain region, and we use the simulation to examine how damage at the cellular level manifested as changes in functional activity at the regional level. This simulated LFP serves as a proxy for scalp EEG data that are

Approved for public release; distribution is unlimited.

used in cognitive neuroscience experiments to understand links between brain and behavior.

The mTBI-related damage mechanism used in our model is based on experimental results from cell cultures⁷⁷ that found transient damage to the neuronal cell membranes that are critical for the modulation of the brain signals that generate and carry information between brain regions. Our approach is also informed by modeling results using molecule-level simulations that have predicted the appearance of blast-induced sodium and potassium permeable pores on the surface of the neuronal membrane.⁷⁴

We used the model to examine the effect of damage to the cellular membrane on the coordinated functional activity of our neuronal network. The study revealed that neuronal injury disrupted overall levels of neuronal activity and the coordinated low-frequency activity of brain signals hypothesized to underlie behavioral performance. This result could be used to enhance the ability to use changes in EEG signals as indicators of TBI.

We also found that damage to the axons of simulated neurons within a single cortical region had a larger impact on overall network activity than did damage to the soma and the dendrites. We hypothesize that similar damage to axons in larger networks that use long distance axonal connections to share information between spatially disparate brain regions will be impaired to an even greater extent than was observed in our single region simulation.

6. Conclusions and Future Studies

mTBI is a major health issue that is hard to diagnose since it often occurs without signs of external injuries. While it is well known that exposure of biological cells to shock waves causes damage to the cell membrane, it is currently unknown by which mechanisms damage is caused and how it depends on physical parameters such as shock wave velocity, shock pulse duration, or shock pulse shape. Threshold shock-impulse levels required to induce cellular injury and cumulative effects upon single and/or multiple exposures are not well characterized. Currently there is no in-vitro experimental model with blast pressure waves generated by using real explosives in the laboratory for investigating the effects of primary blast-induced TBI. Hence, it is critical to develop a reliable experimental research tool in the laboratory to study functional and structural alteration or damage at the cellular and tissue levels following real explosive blast impacts for future improvement of detection and subsequent treatment.

ARL developed the unique in-vitro indoor experimental platform that uses real military explosive charges to accurately represent battlefield blast exposure and to probe the effects of primary explosive blast on dissociated neurons and tissue slices. Our results indicate that membrane damage is occurring, evidenced by LDH release, calcein uptake, and axonal beading, but it is not permanent and the time course is unclear. Injury from blast in the conditions we examined (ca. 10–25 psi) do not appear to cause immediate or sustained damage to the cells. This indicates that delayed cell responses may be responsible for the effects of TBI, or at least mTBI. Three consecutive primary blasts failed to disrupt the overall cellular integrity in the hippocampal slice cultures and produced a unique type of pathology comprised with distinct reduction in synaptic proteins before cellular deterioration set in. These observed changes might add to the challenges in regard to enhancing our understanding of the complex biochemical and molecular mechanisms caused by primary blast-induced injury.

The extent of the cellular compression does not strongly depend on the pressure pulse, but that extension is very sensitive to the change in the negative pressure phase. The structural integrity of the vesicle is altered as pores form in the lipid membrane at overall pressure impulses generated by supersonic shock waves, which are greater than 5 Pa•s at single or repetitive exposure. This is important because they can result in permeability changes in the cell. These changes may lead to an influx of sodium, potassium, and/or calcium ions that in turn can lead to a cascade of events that may ultimately cause cell damage and eventual cell death, resulting in TBI.

All-atom molecular dynamics simulations were used to study potassium, sodium, and chloride ions transport through transmembrane pores between the extra- and intracellular compartments. Initial compositions of the 3 ions in both compartments were set to values found in neurological cells. The concentration gradient between the 2 regions is the driving force for ion transport between the 2 compartments via the transmembrane pore. To find a damage threshold that leads to change of ion homeostasis after brain trauma, membrane transport and concentration are monitored as a function of time for 3 pore radii: $r_i = 1.0, 1.5,$ and 2 nm . Our results show that pores with a radius less than 2 nm exhibited resealing over the course of our 100 ns simulations, where ionic disturbance is minimal at $r_i = 1.5 \text{ nm}$ and nonexistent at $r_i = 1.0 \text{ nm}$. Ion flux through the larger pore ($r_i = 2.0 \text{ nm}$) leads to a substantial change in the intra- and extracellular ionic concentrations, where the cell reaches a new resting state after approximately 80 ns . The simulation results show that the influx of sodium and chloride ions is greater than efflux of potassium ions, which consequently causes an osmotic influx of water. This could result in

the rupture of the cell membrane due to the generated osmotic force that drives an influx of water into the cell.

Based on the recorded tracer data and the simulated pressure wave propagation, the most effective peak pressures were determined along the centerline location of the tank. As the pressure wave diverged outward from the air blast, the pressure wave weakened. The wave propagation from air to PMMA produced a short rise in pressure, followed by a drop in peak pressure in the transition from PMMA to water. However, with controlled standoff distances and knowledge of the explosive strength, the desired input pressures in the samples can be determined and controlled. The internal interactions in the sample wells still need further investigation. More advanced 3-D simulations are desirable as well. Current efforts are underway to pursue this line of investigation and to extend our knowledge in investigating the influence of pressure wave impact on neuronal cells.

More real-time or near real-time points are needed to better elucidate the mechanical injury mechanisms, particularly in the case of repeated blast injury. In addition, real-time analysis of chemical changes such as neurotransmitter or calcium flux would be of great interest to understand changes in cellular function. Electrophysiological measurements would aid in understanding if any functional/connectivity loss is occurring after blast injury. Finally, the development of threshold parameters for cell injury and death are needed. Together, this information can help aid in the treatment and diagnosis of brain injuries, as well as in the design of better head protective equipment.

7. References

1. Nelson NW, Davenport ND, Sponheim SR, Anderson CR. Blast-related mild traumatic brain injury: neuropsychological evaluation and findings. In: Kobeissy FH, editor. Brain neurotrauma: molecular, neuropsychological, and rehabilitation aspects. Boca Raton (FL): CRC Press/Taylor and Francis; 2015. Chapter 32. <http://www.ncbi.nlm.nih.gov/books/NBK299235>.
2. Duckworth JL. Uniformed Services University of the Health Sciences, Bethesda, MD. Personal communication, 2016 Jan.
3. Barthel J, Konkar S, Sankin G, Zhong P, Zauscher S, Darling E, Guilak F, Yen C, Cheeseman B, LaMattina B. Biomechanical and biochemical cellular response due to shock wave. Proceedings of the 26th Army Science Conference 2008; 2008 December 1–4; Orlando, FL.
4. Weinberger S. 2011. Bomb's hidden impact: the brain war. *Nature*. 477:390–393.
5. Svetlov SI, Lerner SF, Kirk DR, Atkinson J, Hayes RL, Wang KW. Biomarkers of blast-induced neurotrauma: profiling molecular and cellular mechanisms of blast brain injury. *J Neurotrauma*. 2009;26:913–921.
6. Morrison B, Elkin BS, Dollé J, Yarmush ML. In vitro models of traumatic brain injury. *Annu Rev Biomed Eng*. 2011;13:91–126.
7. Murphy EJ, Horrocks LA. A model for compression trauma: pressure-induced injury in cell cultures. *J Neurotrauma*. 1993;10:431–44.
8. Shepard SR, Ghajar JBG, Giannuzzi R, Kupferman S, Hariri RJ. Fluid percussion barotraumas chamber: a new in vitro model for traumatic brain injury. *J Surg Res*. 1991;51:417–24.
9. Chen YC, Smith DH, Meaney DF. In-vitro approaches for studying blast-induced traumatic brain injury. *J Neurotrauma*. 2009;26:861–876.
10. Howard D, Sturtevant B. In vitro study of the mechanical effects of shockwave lithotripsy. *Ultrasound Med Biol*. 1997;23:1107–1122.
11. Arun P, Spadaro J, John J, Gharavi RB, Bentley TB, Nambiar MP. Studies on blast traumatic brain injury using in-vitro model with shock tube. *Neuroreport*. 2011;22:379–384.
12. Effgen GB, Hue CD, Vogel E, Panzer MB, Meaney DF. A multiscale approach to blast neurotrauma modeling: part II: methodology for inducing blast injury to in vitro models. *Front Neurol*. 2012;3:1–10.

13. Chen Y, Constantini S. Caveats for using shock tube in blast-induced traumatic brain injury research. *Front Neurol*. 2013;4:1–4.
14. Smith DH, Meaney DF. Axonal damage in traumatic brain injury. *Neuroscientist*. 2000;6:483–495.
15. Elder GA, Mitsis EM, Ahlers ST, Cristian A. Blast-induced mild traumatic brain injury. *Psychiatr Clin N Am*. 2010;33:757–781.
16. Hue CD, Cao S, Haider SF, Vo KV, Effgen GB, Vogel E, Panzer MB, Bass CR, Meaney DF, Morrison B. Blood-brain barrier dysfunction after primary blast injury in vitro. *J Neurotrauma*. 2013;30:1652–1663.
17. Hue CD, Cao S, Bass CR, Meaney DF, Morrison B. Repeated primary blast injury causes delayed recovery, but not additive disruption, in an in vitro blood–brain barrier model. *J Neurotrauma*. 2014;31:951–960.
18. Tischler AS, Greene LA. Nerve growth factor-induced process formation by cultured rat pheochromocytoma cells. *Nature*. 1975;258:341–342.
19. Bernal R, Pullarkat PA, Melo F. Mechanical properties of axons. *Phys Rev Lett*. 2007;99:018301.
20. Pera M, Camps P, Muñoz-Torrero D, Perez B, Badia A, Clos Guillen MV. Undifferentiated and differentiated PC12 cells protected by huprines against injury induced by hydrogen peroxide. *PLoS ONE*. 2013;8(9):e74344.
21. Hinshaw DB, Miller MT, Omann GM, Beals TF, Hyslop PA. A cellular model of oxidant mediated neuronal injury. *Brain Res*. 1993;615:13–26.
22. Fernández P, Pullarkat PA. The role of the cytoskeleton in volume regulation and beading transitions in PC12 neurites. *Biophys J*. 2010;99:3571–3579.
23. Serbest G, Horwitz J, Barbee K. The effect of poloxamer-188 on neuronal cell recovery from mechanical injury. *J Neurotrauma*. 2005;22:119–132.
24. Liu Y, Song X, Liu W, Zhang, T, Zuo, J. Glucose deprivation induces mitochondrial dysfunction and oxidative stress in PC12 cell line. *J Cell Mol Med*. 2003;7:49–56.
25. Edwards MA, Loxley RA, Williams AJ, Connor M, Phillips JK. Lack of functional expression of NMDA receptors in PC12 cells. *Neurotoxicity*. 2007;28:876–885.
26. Cheng J, Gu J, Ma Y, Yang T, Kuang Y, Li B, Kang J. Development of a rat model for studying blast-induced traumatic brain injury. *J Neurolo Sci*. 2010;294:23–28.

Approved for public release; distribution is unlimited.

27. Moomchala SM, Md S, Lu J, Teng CH, Greengrass C. Neuroprotective role of aminoguanidine in behavioral changes after blast injury. *J Trauma*. 2004;56:393–403.
28. Kato K, Fujimura M, Nakagawa A, Saito A, Ohki T, Takayama K, Tominaga T. Pressure-dependent effect of shock waves on rat brain: induction of neuronal apoptosis mediated by a caspase-dependent pathway. *J Neurosurg*. 2007;106:667–676.
29. Cernak I, Wang Z, Jiang J, Bian X, Savic J. Ultrastructural and functional characteristics of blast injury-induced neurotrauma. *J Trauma*. 2001;50:695–706.
30. Koh HS, Yong T, Chan CK, Ramakrishna S. Enhancement of neurite outgrowth using nano-structured scaffolds coupled with laminin. *Biomaterials*. 2008;29:3574–3582.
31. Chew SY, Wen J, Yim EKF, Leong KW. Sustained release of proteins from electrospun biodegradable fibers. *Biomacromolecules*. 2005; 6:2017–2024.
32. Lee JY, Bashur CA, Goldstein AS, Schmidt CE. Polypyrrole-coated electrospun PLGA nanofibers for neural tissue applications. *Biomaterials* 2009;3:4325–4335.
33. LaPlaca MC, Prado GR, Cullen D, Simon CM. Plasma membrane damage as a marker of neuronal injury. Proceedings of the 31st Annual International Conference of the IEEE Engineering in Medicine and Biology Society. 2009 Sep 3–6; Minneapolis, MN. New York (NY): IEEE; c2009; p. 1113–1116.
34. Kilinc D, Gallo G, Barbee KA. Mechanically-induced membrane poration causes axonal beading and localized cytoskeletal damage. *Exp Neurol*. 2008;212:422–430.
35. Monnerie H, Tang-Schomer MD, Iwata A, Smith DH, Kim HA, Le Roux, PD. Dendritic alterations after dynamic axonal stretch injury in vitro. *Exp Neurol*. 2010;224:415–423.
36. Effgen GB, Vogel EW, Lynch KA, Lobel A, Hue CD, Meaney DF, Bass CR, Morrison B. Isolated primary blast alters neuronal function with minimal cell death in organotypic hippocampal slice cultures. *J Neurotrauma*. 2014;31:1202–1210.
37. Ravin R, Blank PS, Steinkamp A, Rappaport SM, Ravin N, Bezrukov L, Guerrero-Cazares H, Quinones-Hinojosa A, Bezrukov SM, Zimmerberg J.

- Shear force during blast, not abrupt changes in pressure alone, generate calcium activity in human brain cells. *PLoS One*. 2012;7(6):e39421.
38. Invitrogen. Conjugation of Qdot ITK Amino (PEG) Quantum Dots to Streptavidin. Carlsbad (CA): Life Technologies; 2005 Dec 12. PN 90-0117, Rev 1.1, mp19021 [accessed 2016 June 27] <https://tools.thermofisher.com/content/sfs/manuals/mp19021.pdf>.
 39. Cooper PW. Explosives Engineering. New York (NY): Wiley-VCH; 1996. Chap 14, p.170–172.
 40. Hesselink L, Sturtevant B. *J Fluid Mech*. 1988;196:513.
 41. Howard D, Sturtevant B. *Ultrasound Med Biol*. 1997;23:1107.
 42. Nakagawa A, Manley GT, Gean AD, Ohtani K, Armonda R, Tsukamoto A, Yamamoto H, Takayama K, Tominaga T. *J Neurotrauma*. 2011;28:1101.
 43. Xi X, Zhong P. *J Acoust Soc Am*. 2001;109:1226.
 44. Koshiyama K, Kodama T, Yano T, Fujikawa S. *Biophys. J*. 2006;91:2198.
 45. Koshiyama K, Kodama T, Yano T, Fujikawa S. *Biochim Biophys*. 2008;1778:1423.
 46. Choubey A, Vedadi M, Nomura K, Kalia RK, Nakano A, Vashishta P. *Appl Phys Lett*. 2011;98:023701.
 47. Ganzenmüller GC, Hiermaier S, Steinhauser MO. *Soft Matter*. 2011;7:4307.
 48. Santo KP, Berkowitz ML. *J Chem Phys*. 2014;140:054906.
 49. Koshiyama K, Wada S. *J Biomech*. 2011;44:2053.
 50. Koshiyama K, Yano T, Kodama T. *Phys Rev Lett*. 2010;105:018105.
 51. Arun P, Abu-Taleb R, Valiyaveetil M, Wang Y, Long JB, Nambiar MP. *Neuroreport*. 2012;2:342.
 52. Farkas O, Lifshitz J, Povlishock JT, *J Neurosci*. 2006;26:3130.
 53. Hoogerbrugge PJ, Koelman JMVA. *Europhys Lett*. 1992;19:155.
 54. Koelman JMVA, Hoogerbrugge PJ. *Europhys Lett*. 1993;21:363.
 55. Español P, Warren PB. *Europhys Lett*. 1995;30:191.
 56. Groot RD, Rabone KL. *Biophys J*. 2001;81:725.
 57. Peters JF. *Europhys Lett*. 2004;66:311.

58. Groot RD, Warren PB. *J Chem Phys.* 1997;107:4423.
59. Grafmüller A, Shillcock J, Lipowsky R. *Biophys J.* 2009;96:2658.
60. Ortiz V, Nielsen SO, Discher DE, Klewin ML, Lipowsky R, Shillcock J. *J Phys Chem B.* 2005;109:17708.
61. Sandia Laboratories home page. LAMMPS molecular dynamics simulator. Albuquerque (NM): Sandia National Laboratories. [accessed on 2013 October 30]. <http://lammps.sandia.gov>.
62. Nagle JF, Tristram-Nagle S. *Biochim Biophys Acta.* 2000; 1469:159.
63. Sliozberg YR, Strawhecker KE, Andzelm JW, Lenhart JL. *Soft Matter.* 2011;7:7539.
64. Lin KW, Kim T, Maxwell AD, Wang TY, Hall TL, Xu Z, Fowlkes JB, Cain CA. *IEEE Trans Ultrason Ferroelectr Freq Control.* 2014;61:251.
65. Kodama T, Hamblin MR, Doukas AG. *Biophys J.* 2000;79:1821.
66. Başar E, Güntekin B. A review of brain oscillations in cognitive disorders and the role of neurotransmitters. *Brain Research.* 2008;1235:172–193. doi:10.1016/j.brainres.2008.06.103.
67. Orban GA. *Neuronal operations in the visual cortex.* New York (NY): Springer Science and Business Media; 2012.
68. Klimesch W, Sauseng P, Hanslmayr S, Gruber W, Freunberger, R. Event-related phase reorganization may explain evoked neural dynamics. *Neuroscience and Biobehavioral Reviews.* 2007;31:1003–1016. doi:10.1016/j.neubiorev.2007.03.005.
69. Alivisatos AP, Chun M, Church GM, Greenspan RJ, Roukes ML, Yuste R. The brain activity map project and the challenge of functional connectomics. *Neuron.* 2012;74:970–4. doi:10.1016/j.neuron.2012.06.006.
70. Bressler SL, Kelso JS. Cortical coordination dynamics and cognition. *Trends in Cognitive Sciences.* 2001;5:26–36.
71. Bressler SL, Menon V. Large-scale brain networks in cognition: emerging methods and principles. *Trends in Cognitive Sciences.* 2010;14:277–290. doi:10.1016/j.tics.2010.04.004.
72. Insel TR, Landis SC, Collins FS. The NIH brain initiative. *Science.* 2013;340:687–688. doi:10.1126/science.1239276.

73. Meaney DF, Smith DH. Cellular biomechanics of central nervous system injury. *Handbook of Clinical Neurology*. 2015;127:105–114.
74. Slonberg Y, Chantawansri T. Damage to spherical cellular membrane generated by the shock waves: coarse-grained molecular dynamics simulation of a lipid vesicle. *J of Chem Phys*. 2014;141(18):184904.
75. Traub RD, Contreras D, Cunningham MO, Murray H, LaBeau FEN, Roopun A, Bibbig A, Wilent WB, Higley MJ, Whittington MA. Single-column thalamocortical network model exhibiting gamma oscillations, sleep spindles, and epileptogenic bursts. *J Neurophysiology*. 2005;93(4):2194–2232. Epub 2004 Nov 3.
76. Rall W. Electrophysiology of a dendritic neuron model. *Journal of Biophysics*. 1962 Mar 2;(2 Pt 2):145–167.
77. Zander N, Piehler T, Boggs M, Banton R, Benjamin R. In vitro studies of primary explosive blast loading on neurons. *J Neuro Res*. 2015;93:1353–1353.

Appendix A. Unpublished Work

This appendix appears in its original form, without editorial change.

Approved for public release; distribution is unlimited.

1. Pressure threshold studies with NG108-15 neuroblastoma/glioma rat cell line. Standoff distances from 225 mm to 325 mm (pressures ca. 400 – 40 psi) evaluated to determine effect on cell viability, membrane permeability, reactive oxygen species, and intracellular calcium. Repeated blast also evaluated. Reactive oxygen species was elevated with blast and in general increased with pressure or repeated insult. Membrane permeability and intracellular calcium increased with blast, but did not show strong correlations with pressure or repeated blast. Cell death was minimal except at very high pressures.
2. Mixed rat cortical primary cultures exposed to single and repeated blast (6–10 psi). Glutamate, lactate dehydrogenase, membrane permeability, sodium, reactive oxygen and species increased with blast. Membrane permeability, intracellular sodium, and reactive oxygen species are significantly higher for triple shot compared to single shot.
3. Human primary neurons and glia from stem cells exposed to 250 and 300 mm standoff distances. Intracellular sodium, reactive oxygen species and cell death increased with blast.
4. Not reported here are the initial studies on blast-induced neurodegeneration in brain slice samples were conducted by using a novel in vitro indoor explosively generated blast impact experimental system to probe the effects of explosive blast (ranging from about 20 to 100 psi) on cultured tissue slice samples. This work was a collaboration effort between ARL DSI WMRD team and Prof. Ben Bahr from University of North Carolina – Pembroke. The initial results showed that a single blast had no effect on the GluR1 immunoreactivity level, whereas the triple blast insult caused a significant reduction in the GluR1 synaptic marker compared to the submerged control slices. This might be an indication of a dose-dependent effect. These results warrant further analysis of hippocampal slice samples to better understand dose-dependent effects of blast-induced brain damage. Slices harvested earlier and later during the recovery period will provide more information concerning the onset of neurodegeneration and injury thresholds and thus determining whether distinct stages of blast-induced injury occur, as well as blast threshold profiles for induction of transient changes versus induction of persistent cellular damage. Subsequent analyses will assess whether cytoskeletal deterioration and/or loss of presynaptic integrity contribute to the damage, providing additional indicators of blast-induced neuronal compromise.

Appendix B. Journal Publications

- Piehlert T, Banton R, Piehlert L, Benjamin R, Sparks R, Smith Marquitta, Bahr B. Preliminary study of realistic blast impacts on cultured brain slices. Aberdeen Proving Ground (MD): Army Research Laboratory (US); 2015 April. Report No.: ARL-TR-7197.
- Piehlert T, Zander N, Benjamin R. Primary explosive blast-induced traumatic brain injury model in PC12 cell culture. Bioprotocol.org. Forthcoming 2016.
- Sliozberg YR, Chantawansri TL. Damage in spherical cellular membrane generated by the shock waves: coarse-grained molecular dynamics simulation of lipid vesicle. *Journal of Chemical Physics*. 2014;141:184904.
- Sliozberg YR, Chantawansri TL. Structural changes in lipid vesicles generated by the shock waves: dissipative particle dynamics simulation, dynamic behavior of materials. In: Song B, Casem D, Kimberley J, editors. *Proceedings of the 2014 Annual Conference on Experimental and Applied Mechanics. Dynamic Behavior of Materials, Vol. 1*. New York (NY): Springer International Publishing; 2015. p. 121–126.
- Sliozberg YR, Chantawansri TL. Mechanism resulting in chemical imbalance due to cellular damage associated with mechanoporation: a molecular dynamics Chem Phys Lett. Forthcoming 2016.
- Zander N, Piehlert T, Boggs M, Benjamin R, Banton R. In vitro studies of primary explosive blast loading on neurons. Aberdeen Proving Ground (MD): Army Research Laboratory (US); 2014 Oct. Report No.: ARL-TN-7104.
- Zander N, Piehlert T, Boggs M, Banton R, Benjamin R. In vitro studies of primary explosive blast loading on neurons. *J Neuroscience Res*. 2015;9:1353–1363.
- Zander N, Piehlert T, Banton R, Boggs M. Single and repeated blast loading on human neuroblastoma cells. *Cellular and Molecular Neurobiology*. Forthcoming 2016.

List of Symbols, Abbreviations, and Acronyms

3-D	3-dimensional
AMPA	α -amino-3-hydroxy-5-methyl-4-isoxazolepropionic acid
AMR	adaptive mesh refinement
AP	action potential
ARL	US Army Research Laboratory
CLSM	confocal laser scanning microscopy
DI	deionized
DMEM	Dulbecco modified medium
DMPC	dimyristoyl-phosphatidylcholine
DMSO	dimethyl sulfoxide
DPD	dissipative particle dynamics
DSI	Director's Strategic Initiative
DSS linker	disuccinimidyl suberate
EEG	electroencephalography
EOS	equation of state
GABA	γ -aminobutyric acid
HBSS	Hank's balanced salt solution
ID	identification
JWL	Jones-Wilkens-Lee
LDH	lactate dehydrogenase
LFP	local field potential
MEG	magnetoencephalography
mTBI	mild traumatic brain injury
NGF 7S	nerve growth factor
NMDA	N-methyl-D-aspartate

PBS	phosphate buffered saline
PMMA	poly (methyl methacrylate)
QD	quantum dot
succinyl Con A	succinyl-Concanavilin A
USU	Uniformed Services University of the Health Sciences

1 DEFENSE TECHNICAL
(PDF) INFORMATION CTR
DTIC OCA

2 DIRECTOR
(PDF) US ARMY RESEARCH LAB
RDRL CIO L
IMAL HRA MAIL & RECORDS MGMT

1 GOVT PRINTG OFC
(PDF) A MALHOTRA

12 DIR USARL
(PDF) RDRL DE
T CHANTAWANSRI
RDRL HR
P FRANASZCZUK
RDRL HRF B
A YU
J VETTEL
RDRL SLB W
D BOOTHE
RDRL WML C
T PIEHLER
R BENJAMIN
R SPARKS
RDRL WMM G
N ZANDER
L PIEHLER
Y SLIOZBERG
RDRL WMP G
R BANTON

INTENTIONALLY LEFT BLANK.